Technische Universität München
TUM School of Engineering and Design

Laser-Based Powder Bed Fusion Process Simulation with Smoothed Particle Hydrodynamics

Christopher Zöller

Vollständiger Abdruck der von der TUM School of Engineering and Design der Technischen Universität München zur Erlangung eines

Doktors der Ingenieurwissenschaften (Dr.-Ing.)

genehmigten Dissertation.

Vorsitz: Prof. Dr.-Ing. Florian Holzapfel

Prüfende der Dissertation:

1. Prof. Dr.-Ing. Nikolaus A. Adams
2. Prof. Dr. Peter Mayr

Die Dissertation wurde am 12. März 2025 bei der Technischen Universität München eingereicht und durch die TUM School of Engineering and Design am 18. August 2025 angenommen.

Abstract

This work aims to enhance the understanding of laser powder bed fusion process behavior on the micro-scale through numerical simulation. The additive manufacturing technique allows for exceptional design flexibility and high material efficiency. Current research indicates that powder bed fusion even has the potential to control microstructure and allow for the combination of different materials. This makes locally tailored material properties possible without altering the part geometry. However, controlling the process remains a challenge. Improper settings can lead to defects such as porosity, residual stresses, cracks, or rough surface topology. Therefore, a detailed understanding of the process mechanisms is essential to prevent defects and realize the full potential of locally optimized material properties. High spatial and temporal resolution simulations provide valuable insights into the process and enable a detailed analysis of the underlying mechanisms. However, the complex geometries, multiple phase transitions, and violent interface dynamics pose a significant challenge for numerical methods. The particle method, Smoothed Particle Hydrodynamics, is particularly well-suited for modeling such phenomena. Hence, the first objective of this work is to develop a Smoothed Particle Hydrodynamics model for simulating the powder bed fusion process. Here, the focus lies on developing a robust surface tension model. The model is subsequently used to study the powder bed fusion process. The first study aims to analyze the mechanisms behind the balling defect. A second study focuses on laser beam-shaping, a promising technique with the potential to generate locally tailored material properties. Here, the influence of laser beam size, shape, and exposure time on melt pool evolution is investigated.

The dissertation is structured as a cumulative work comprising three peer-reviewed journal articles. Chapter 1 introduces the laser powder bed fusion process, and motivates the use of Smoothed Particle Hydrodynamics for process simulation. Chapter 2 introduces the fundamental physical processes of powder bed fusion, focusing on the balling defect and laser beam-shaping. After a summery of the current state-of-the-art in Smoothed Particle Hydrodynamics modeling, the governing equations and their numerical implementation are presented. Chapter 3 summarizes the results of the individual publications and places them in the context of the current state of research. The dissertation concludes with a discussion of the findings and an outlook on future investigations in Chapter 4. The corresponding research articles are included in the appendix.

Zusammenfassung

Das Ziel dieser Arbeit ist es, das Prozessverhalten von Laser-Pulverbett-Schmelzverfahren durch numerische Simulation auf der Mikroskalenebene besser zu verstehen. Das additive Fertigungsverfahren ermöglicht eine außergewöhnliche Designfreiheit und hohe Materialeffizienz. Aktuelle Forschungen zeigen, dass sich beim Pulverbett-Schmelzen sowohl die Mikrostruktur gezielt steuern als auch unterschiedliche Materialien kombinieren lassen. Dies ermöglicht es, Materialeigenschaften lokal anzupassen, ohne die Geometrie des Bauteils verändern zu müssen. Die Kontrolle des Prozesses stellt jedoch weiterhin eine Herausforderung dar. Ungünstige Einstellungen können Defekte wie Porositäten, Eigenspannungen, Risse oder eine raue Oberflächentopologie verursachen. Ein tiefgreifendes Verständnis der Prozessmechanismen ist daher entscheidend, um Fehler zu vermeiden und das Potenzial lokal-optimierter Materialeigenschaften umzusetzen. Simulationen mit hoher räumlicher und zeitlicher Auflösung ermöglichen wertvolle Einblicke in den Prozess und erlauben eine detaillierte Analyse der Wirkmechanismen. Allerdings ist die Simulation aufgrund der komplexen Geometrien, mehrfachen Phasenwechsel und hochdynamischen Mehrphasenströmungen eine große Herausforderung für numerische Verfahren. Die Partikelmethode, Smoothed Particle Hydrodynamics, eignet sich besonders gut zur Modellierung solcher Phänomene. Das erste Ziel dieser Arbeit besteht daher in der Entwicklung eines Smoothed Particle Hydrodynamics Modells zur Simulation des Pulverbett-Schmelzprozesses. Hierbei liegt der Fokus auf der Eintwicklung eines robusten Oberflächenspannungsmodells. Das Modell wird im Anschluss zur Vertiefung des Prozessverständnisses eingesetzt. Die erste Untersuchung zielt darauf ab, die Mechanismen hinter dem Defekt der Schmelzbadseparation und der anschließenden Schmelzakkumulation zu analysieren. Eine zweite Untersuchung konzentriert sich auf die Laserstrahlformung, eine vielversprechende Technik mit dem Potenzial zur Erzeugung lokaler Materialeigenschaften. Hierbei wird insbesondere der Einfluss der Laserstrahlgröße, Laserstrahlform und Belichtungszeit auf die Schmelzbadentwicklung untersucht.

Die Dissertation ist als kumulative Arbeit strukturiert und besteht aus drei entstandenen Fachartikeln. In der Einleitung werden das Laserstrahl-Schmelzverfahren vorgestellt und der Einsatz der Smoothed Particle Hydrodynamics Methode für die Prozesssimulation motiviert. Kapitel 2 gibt eine Einführung in die grundlegenden physikalischen Prozesse des Pulverbett-Schmelzens, insbesondere den Balling-Defekt und die Laserstrahlformung. Zudem wird der Stand-der-Technik der Smoothed Particle Hydrodynamics Modellierung in der Prozesssimulation zusammengefasst und die relevanten Gleichungen und deren numerische Disketisierung werden erläutert. Es folgt eine Zusammenfassung der Ergebnisse der veröffentlichten Arbeiten und deren Einordnung in den Stand-der-Technik in Kaptiel 3. Die Dissertation schließt mit einer Diskussion der Ergebnisse und einem Ausblick auf zukünfige Untersuchungen in Kapitel 4. Im Anhang sind die zugehörigen Fachartikel aufgführt.

Danksagung

Die vorliegende Arbeit ist während meiner Zeit am Lehrstuhl für Aerodynamik und Strömungsmechanik von 2018 bis 2024 entstanden. An dieser Stelle möchte ich mich bei allen bedanken, die mich während dieser Zeit unterstützt haben.

Zuallererst möchte ich mich bei Herrn Prof. Dr.-Ing. Adams bedanken. Bereits im Grundstudium haben Sie mich für die Strömungsmechanik begeistert und ein Großteil meiner akademischen Ausbildung wurde maßgeblich durch Sie sowie die Doktoranden und Postdocs Ihres Lehrstuhls geprägt. Vielen Dank für das entgegengebrachte Vertrauen und den Freiraum bei der Gestaltung meiner Promotion. Die stets angenehme und offene Arbeitsatmosphäre am Lehrstuhl hat dazu beigetragen, dass ich dort gerne viel Zeit verbracht habe. Besonders bedanken möchte ich mich auch für die unkomplizierte Zusammenarbeit sowie Ihre wertvolle Unterstützung bei den Publikationen.

Des Weiteren möchte ich mich bei Herrn Prof. Dr. Peter Mayr bedanken. Sowohl für den interessanten Austausch bei tum.Additive und Advanced Manufacturing Institute Veranstaltungen als auch für die Zweitprüfung meiner Arbeit.

Ein besonderer Dank gilt auch Dir, Stefan. Deine Begeisterung für die SPH-Methode hat sich bereits während meiner Semesterarbeit auf mich übertragen und war ein wichtiger Anstoß für den Weg zur Promotion. Gemeinsam mit Jakob hast Du mir diese Möglichkeit erst eröffnet. Deine Betreuung hat sowohl meine fachliche als auch persönliche Weiterentwicklung geprägt und war maßgeblich für den erfolgreichen Abschluss meiner Promotion.

Darüber hinaus möchte ich mich bei den Lehrstuhlkollegen für die gute Zeit bedanken. Besonders die Zusammenarbeit mit den SPH-Kollegen Fabian, Fabian und Matthias hat mir hinsichtlich C++ Programmierung und SPH Modellierung viel geholfen. Es freut mich besonders, dass es trotz (oder vielleicht auch wegen) der 1861er Kollegen – Paula, Ruhland und Klukas – mit der Promotion geklappt hat.

Weiterer Dank gilt den Mitbewohnern der Dietersheimer WG. Die verrückten Momente mit Salah, Sarah, Diego, Raphael und Daniel waren genau der richtige Ausgleich in dieser herausfordernden Zeit.

Mein größter Dank gilt meiner Familie, deren Hilfe über all die Jahre diesen Weg überhaupt erst möglich gemacht hat. Besonders der stetige Austausch und die gemeinsamen Urlaube haben geholfen eine gewisse Work-Life-Balance zu bewahren. Ein ganz besonderer Dank geht an Dich, Adina, für deine liebevolle Unterstützung und eindringliche Motivation an den Wochenenden an der Dissertation zu arbeiten.

München, February 24, 2025 *Christopher Zöller*

Contents

List of Figures **ix**

Acronyms **xi**

1 Introduction **1**

2 Theoretical background **5**
2.1 Physics of Laser-Based Powder Bed Fusion . . . 5
2.2 Balling Defect . . . 7
2.3 Laser Beam-Shaping . . . 10
2.4 Governing Equations . . . 12
2.5 Smoothed Particle Hydrodynamics . . . 15
2.5.1 Basics . . . 16
2.5.2 Density Equation . . . 18
2.5.3 Equation of Motion . . . 18
2.5.4 Momentum Equation . . . 20
2.5.5 Energy Equation . . . 24
2.5.6 Boundary Conditions . . . 25
2.5.7 Time Stepping . . . 26

3 Contributions **29**
3.1 A partitioned continuous surface stress model for multiphase smoothed particle hydrodynamics . . . 29
3.2 Numerical investigation of balling defects in laser-based powder bed fusion of metals with Inconel 718 . . . 32
3.3 Beam-shaping in laser-based powder bed fusion of metals: A computational analysis of point-ring intensity profiles . . . 34

4 Discussion and Conclusion **37**

A A partitioned continuous surface stress model for multiphase smoothed particle hydrodynamics **39**

B Numerical investigation of balling defects in laser-based powder bed fusion of metals with Inconel 718 **59**

C Beam-shaping in laser-based powder bed fusion of metals: A computational analysis of point-ring intensity profiles **73**

Bibliography **87**

List of Figures

2.1 Top view and longitudinal cross section view of single melt track balling process at time instances a) $t = 1960\ \mu s$, b) $t = 2160\ \mu s$, c) $t = 2180\ \mu s$ and d) $t = 2380\ \mu s$ after the irradiation start. 8
2.2 Schematic illustration of intensity distribution I over the radial distance from the beam center r for common beam profiles. 10
2.3 Cross section view of melt pool after $t = 42.5\ \mu s$ irradiation with a) Gaussian profile of 107 μm spot diameter, b) VBPP4 profile of 107 μm spot diameter, and after $t = 250\ \mu s$ irradiation with c) Gaussian profile of 253 μm spot diameter, and d) VBPP4 profile of 253 μm spot diameter. 11
2.4 Initial (left) and steady-state (right) particle distribution of a square to droplet deformation due to the action of surface tension 15
2.5 Three dimensional droplet shape for a wetting and non wetting scenario with wetting angles of a) $\theta_w = 60°$ and b) $\theta_w = 120°$ 26

Acronyms

SPH Smoothed Particle Hydrodynamics

FVM Finite Volume Method

FEM Finite Element Method

DEM Discrete Element Method

CSS Continuous Surface Stress

CSF Continuous Surface Force

CFL Courant-Friedrichs-Lewy

CA Cellular Automata

DOE Diffractive Optical Element

Chapter 1

Introduction

This thesis provides an overview over my research into the powder-scale process behavior of laser powder bed fusion of metals with the Smoothed Particle Hydrodynamics (SPH) method. The work focuses on three key areas: the development of a SPH Continuous Surface Stress (CSS) surface tension model for multiphase flows with high density ratios, the investigation of melt pool breakups and balling in a regime of fully melted powder and substrate remelting, and the examination of the influence of point-ring laser beam shapes on melt pool dynamics and process behavior.

Laser-based powder bed fusion of metals introduces many new possibilities to the field of production technology. A fundamental understanding of the process behavior is necessary for its reliable application. The basic approach is the application of a high-energy laser beam to selectively melt powder particles within a powder bed. The emerging molten pool coalesces with the preceding layer of material, adding to the layer height. This process occurs in a continuous alternation with the application of new powder, resulting in an additive manufactured three-dimensional part. With laser dimensions and powder particles in the order of micro-meters, powder bed fusion allows for the fabrication of small-scale structures. The production process introduces minimal requirements, allowing for a high degree of design freedom. Further, powder bed fusion can enable the processing of local multi-material composites [24, 143] and even locally tailor the microstructure. This allows the generation of desired material properties without adjusting the component structure [110, 111, 144]. When process understanding and control reach a level where these benefits can be fully leveraged, laser-based powder bed fusion will greatly enhance conventional formative and subtractive manufacturing techniques.

However, ensuring consistent, high-quality part production is still a challenge due to process complexity. Its application in aerospace, automotive, and bio-medicine industries, where part failure is critical and minimal tolerance for defects is acceptable, necessitates a high level of process repeatability. Effectively controlling a process characterized by intricate laser-powder interactions, high temperature gradients, multiple rapid phase transitions, and a highly dynamic melt pool convection, all occurring simultaneously within microseconds, remains challenging. An appropriate selection of process parameters is inevitable. Laser power, spot size, spot shape, scan speed, scan path, powder material, and powder layer thickness are just a few of the relevant parameters that need to be configured. An improper setup can result in various undesirable consequences, including unstable melt pools [47], powder denudation [83], spatter [56], incomplete melting [108], lack of fusion [116], keyhole collapse [82], or balling [116]. These defects may lead to parts exhibiting high porosity, micro-cracks, poor surface finish, elevated thermal stresses, or unfavorable microstructure. A profound understanding of the manufacturing process is therefore required.

Extensive research is necessary to understand the relevant physics and to derive printer setups and print strategies that avoid manufacturing defects and enable targeted material properties or local alloying. Process complexity and micro-level temporal and spatial scales often render experimental in-situ measurements of physical phenomena impractical. Instead, numerical simulation has proven beneficial in enhancing the process understanding at the microscopic level. Nevertheless, achieving an accurate representation requires extensive numerical modeling. The multiphase characteristics, phase transitions, and complex interface topologies featuring strong deformations pose severe challenges to the numerical algorithms. Nevertheless, simulation studies made several significant contributions to an enhanced process understanding. The following paragraphs highlight selected advantages of simulation, supported by examples from the literature, illustrating how simulations contribute to a better process understanding.

Analysis of numerical results allows us to isolate and identify dominant physics. The study of single-track simulations suggests surface tension drives the melt pool dynamics while gravity and buoyancy play marginal roles [57]. They find that surface tension acts towards the coalescence of melted powder particles, necking, and melt pool breakup due to the Plateau-Rayleigh instability. Based on the simulation results, beam size variations for a target melt pool width-to-length ratio for stable tracks are suggested [57]. Hence, the knowledge gained from simulations is used to motivate process improvements.

Simulation campaigns often enhance experimental investigations to find an explanation for specific process behavior. For example, in a study of powder denudation, an outward metal vapor flux and an induced shear flow are identified as drivers for powder motion [83]. Here, simulation results explain the experimentally observed powder behavior by providing direction information of vapor flow.

Process simulation also enhances understanding of defect mechanisms. In [56], Khairallah et al. use an arbitrarian Lagrangian-Eulerian hybrid finite volume finite element model to closely study melt track anatomy. Three regions of distinct physics are identified across the melt pool. The importance of recoil pressure and Marangoni convection to the melt pool shape is demonstrated. The simulation results allow to draw explanations for defect mechanisms such as the melt-pool breakup, spatter formation, and vapor cavity dynamics. A study of pore formation uses process simulations to understand the rapid formation and collapse of deep keyholes [82]. The simulation results identify locations of strong vapor recoil effects and explain the keyhole collapse. The formulated mitigation strategy where a constant vapor cavity depth is achieved by a constant normalized enthalpy proofs to reduce the occurrence of pores.

In numerical studies, a precise initial setup can be defined, which allows the investigation of specific process scenarios. In [58], the complexity of process control at non-ideal conditions is highlighted by a study of spatter formation due to the presence of a powder cluster. The results give insight into spatter acceleration and dynamics, laser-spatter interaction, and the corresponding melt pool vapor depression. By initializing a specific set of process parameters, start-of-track back-spatter is generated. The results demonstrate the problem of a fast laser power increase and allow for formulating a power ramp-up criterion. Thus, simulation results are used to reduce spatter in powder bed fusion processes.

Numerical parameter studies show the trends of powder bed fusion processes. In [71], the local temperature field dependence on laser power and scan speed is investigated. The cooling rate is found to depend more on scan speed than laser power. In contrast, the temperature gradient in the depth direction is more dependent on the laser power.

Numerical investigations allow for a close spatial and temporal analysis of thermal behavior at different process conditions. This information is vital for microstructure prediction. The simulation campaign by Roberts et al. [109] reviles the temperature history of multi-layer builds. They find that scanning of a consecutive layer shows a similar heating cycle in the prior layer but at a reduced temperature level. As the heat conduction rate to the base plate is reduced, peak temperatures of consecutive layers increase. These thermal cycles of multi-layer builds need to be studied closely as they are associated with the thermal stress cycles. The provided information by process simulations on the temperature field can be used for microstructure analysis. In [66], the solidification of single melt tracks is investigated. Here, mesoscale process simulations provide the required information about temperature gradients at the solid-liquid interface and the solidification rate. Including this information in solidification, models allow for the prediction of grain morphology and the primary dendrite arm spacing.

In most numerical powder bed fusion investigations, conventional grid-based discretization schemes such as the Finite Volume Method (FVM) or Finite Element Method (FEM) are used. These methods require considerate modeling efforts to resolve the complex powder geometry and violent melt-pool surface motion and to account for the multitude of physical effects. However, there exists a discretization method particularly well suited for powder bed fusion process simulations, the Smoothed Particle Hydrodynamics method [34, 79]. In contrast to grid-based methods, SPH is highly adaptable for the simulation of complex geometries [75] such as powder bed structures and dynamic melt-solid boundaries. Different particles are used to represent different materials and phases, enabling multi-material and multiphase applications. It also naturally defines the location of interfaces between particles of different phases. As the SPH particles advect with the flow field interface tracking is handled implicitly without the need for computationally demanding interface tracking algorithms such as in volume-of-fluid or level-set approaches. Complex re-meshing and moving meshes due to distortions or folding are not required [75]. The SPH method remains numerically stable for strong interface deformations, making it ideal for simulating dynamic melt pools with complex topology. Many physical phenomena can be incorporated without modifying the underlying algorithms [89, 94]. Defining a fixed mass for each SPH particle ensures mass conservation effortlessly. Conservative formulations also exist for momentum and energy [52]. The SPH algorithms can be efficiently parallelized for high-performance computing architectures, enabling high-resolution numerical studies despite its high computational cost [29]. Therefore, the method was chosen for the numerical studies of this work.

This thesis summarizes my contribution to advancing the understanding of the laser powder bed fusion process. The developed Smoothed Particle Hydrodynamics model is used to study both a process defect and a potential process enhancement technique. This thesis includes the following three contributions, which are published in the peer-reviewed Journal of Computational Physics and the Journal of Additive Manufacturing:

1. A stable and efficient continuous surface stress formulation for Smoothed Particle Hydrodynamics, including a static wetting model.
2. A numerical study of the balling defect in a regime characterized by considerate substrate remelting highlighting the breakup process's driving forces and mechanisms.
3. A detailed investigation of point-ring laser beam-shape effects on single melt tracks, focusing on beam size and beam shape contributions.

The research was also presented at scientific conferences, namely the VII International Conference on Particle-based Methods - Particles, 2021, in Hamburg, the 9th GACM Colloquium on Computational Mechanics, 2022, in Essen, and the Fourth International Conference on Simulation for Additive Manufacturing, 2023, in Munich.
The remainder of this work is structured as follows: Chapter 2 summarizes the theoretical background for the three research articles. It consists of a brief review of laser powder bed fusion physics focusing on the balling defect and laser beam-shaping. Then, the main governing equations describing the physical process behavior are stated and the state-of-the-art in SPH modeling is summarized. Typical SPH multiphase formulations are presented, and a short summary of surface tension models is included. Chapter 3 summarizes the publications and highlights their novelty concerning the state-of-the-art. The thesis closes with conclusions drawn from the research in Chapter 4. The appendix provides the corresponding list of publications.

Chapter 2

Theoretical background

2.1 Physics of Laser-Based Powder Bed Fusion

In laser-based powder bed fusion of metals, many physical phenomena coincide. Below is a brief overview of selected physical behavior at the powder-scale.

In the initial state, a build chamber is considered, where a layer of powder covers a substrate. The packing density and powder distribution depend, among other factors, on the powder particle size distribution, adhesive forces, and powder morphology [86]. The material is either maintained at room temperature or preheated to a specific temperature [135]. To prevent oxidation, the build chamber is filled with an inert gas [60]. This protective gas is consistently passed over the powder bed throughout the process.

In order to fuse the powder with the substrate, a high-intensity laser beam is traversed across the build surface. Adjustments such as laser power, scan speed, hatch distance, and scan path will allow the laser to be tailored to the specific process conditions. The additional tuning parameters of laser spot size and intensity distribution are considered when aiming for optimized energy input through laser beam-shaping. The laser radiation is absorbed and reflected at the substrate and powder surfaces. The proportion of absorbed radiation depends on the incidence angle and the material's absorbtivity, which is often temperature and wavelength-dependent [46, 127]. Through multiple laser beam reflections, the proportion of absorbed energy increases within the powder bed [57]. A portion of the energy absorbed at the surface is released to the surroundings through thermal emission or by convective cooling of the protective gas flow [71]. The remaining energy dissipates into the bulk or induces a temperature rise, ultimately melting the material. The thermal conductivity of most metals is temperature-dependent, causing the rate of dissipation to increase with rising temperatures [97]. Due to localized contacts, the heat transfer between powder particles is minimal [7]. Transitioning from a solid to a liquid state requires additional energy, the latent heat of phase change. During the melting process, the material absorbs this latent heat, causing only a slight change in temperature in the case of non-isothermal melting or maintaining a constant temperature in the case of isothermal melting.

The molten material wets the powder and substrate. With sufficient energy input, the melt islands ultimately fuse to form a melt pool. The heating and melting process occurs so rapidly that the molten pool often forms still within the laser-irradiated zone. Thus, laser power continues to be absorbed within the melt as well. Here, too, absorption is determined by the thermal dependence of the material-specific absorption and by multi-reflections of the laser radiation [9]. As temperatures are high, thermal emission and heat transfer to the ambient gas also increase. The spatial distribution of thermal energy induces a dynamic within the molten pool, primarily determined by three phenomena. With higher energy content, the density of the material decreases. Under the action of gravity, buoyancy forces induce warmer melt to rise relative to colder melt [142]. Strong temperature gradients prevail at the melt pool surface, primarily due to the laser intensity distribution. With Gaussian lasers, a high temperature can be observed in the molten pool near the center of the laser-irradiated zone [98]. This temperature decreases towards the sides as well as upstream and downstream. The surface tension between molten metals and protective gases often decreases with increased energy [97]. Thus, the energy distribution creates a gradient in surface tension towards the cooler regions of the melt pool. The surface tension forces can be divided into a component normal to the interface, known as the capillary force, and a component tangential to the surface, referred to as the Marangoni force. The capillary force is proportional to the surface tension, thus exerting a more substantial influence in the colder regions of the melt pool. Furthermore, it is proportional to the local curvature of the interface, thus acting only on curved areas. The Marangoni force arises due to gradients in surface tension along the surface. It is directed towards higher surface tension and is particularly strong in regions of pronounced temperature gradients. Thus, the Marangoni forces induce convection upstream, sideways, and downstream of the high-temperature zone. Furthermore, surface tension strongly influences the molten pool's morphology and is associated with phenomena such as necking [103], fish scales [76], and balling [48]. Another effect of surface tension is the wetting ability of the molten material on the surrounding solid material. Among other factors, wetting depends on surface roughness and oxidation [41, 74]. The third dynamic-inducing phenomenon influenced by the energy distribution is evaporation. When the local energy content is sufficiently high, the melt undergoes evaporation. Once again, an additional latent heat of phase change is required before reaching the boiling point. The expelled vapor induces a recoil pressure on the molten pool surface [63]. Pressure gradients then lead to melt convection out of the region of evaporation. A vapor capillary develops. This melt pool regime allows for deep penetration into the substrate, facilitating mixing materials from multiple layers. However, the molten pool in keyhole mode is particularly dynamic. Instabilities and the collapse of vapor capillaries can lead to gas entrapments [82]. As a result, porosities may remain in the build. In addition to the recoil effect, evaporation also influences the build process through the vapor stream. The high velocities of the escaping vapor induce a flow of the protective gas, which can become strong enough to entrain powder particles. This effectively alters the powder distribution for the melt track [83]. The powder bed denudation also poses a significant challenge for localized alloying, as it results in mixing different powders [40]. Moreover, the vapor interacts with the laser, potentially causing fluctuations in the laser energy applied to the melt and powder bed. Accurately comprehending and controlling the different types of melt pool convection is essential to avoid defects in the manufactured parts.

The melt pool advection contributes to the distribution of energy in the melt. A portion of its kinetic energy is dissipated as heat through viscous heating [6]. In addition to convection, heat conduction also occurs both within the melt and across the melt-solid phase interface.

Downstream of the laser, the melt pool cools down rapidly. Once the temperatures have dropped sufficiently, the solidification process begins. During the liquid-solid phase transition, the latent heat of fusion is released. Between the melting and solidification points, a mushy zone forms where both solidified and liquid material coexist [127]. Solidification is influenced by the rapid cooling rate, local thermal gradients, and the melt pool geometry [118]. Unfavorable solidification conditions can lead to residual stresses or micro-cracks in the material [84, 120]. Size, crystal morphology, and texture influence mechanical properties such as strength, ductility, creep, fatigue, and crack propagation resistance of the manufactured part [118]. Targeted solidification through appropriate variation of process parameters promises the production of tailored mechanical properties [110]. Therefore, a precise understanding and prediction of solidification behavior is particularly desirable. Scan paths, including laser turns, hatch spacing, multi-tracks, and multi-layer heating cycles, further influence the solidified material, adding to the manufacturing complexity.

Once the powder and substrate are coalesced and solidified, a new layer of powder is applied, and the process starts again. In conclusion, laser-based powder bed fusion involves a complex interplay of physical phenomena, from powder distribution to melt pool dynamics and solidification. While my research mainly focuses on thermofluid dynamics, its connection to the entire build process should be kept in mind throughout the manuscript. The introduced physics provides a basis for the following sections on balling, beam-shaping, and the mathematical description for process simulations.

2.2 Balling Defect

Balling is the breakup of continuous melt pools into melt agglomerates. The entire necking, pinch-off, and ball formation process is shown in Fig. 2.1. The phenomenon is observed in melt tracks of various materials, including aluminum, titanium, nickel, and steel alloys [55, 68, 74, 136]. Balling and related processes, such as the aggregation of melt islands or humps [35, 65], are recognized as critical defect mechanisms alongside keyhole instabilities and under-melting [31]. It is found at high laser scan speeds at both high [99] and low [65] laser power and at low laser scan speeds and high laser power [142]. Extensive efforts have been devoted to finding process maps of stable production [45, 134, 136] avoiding balling and corresponding final part defects. The consequences of balling include non-uniform powder distribution in consecutive powder layers, poor wettability of the previous layer [92, 104], and pore formation [68]. It can even interrupt the build process due to collisions with the paving roller [68]. These issues contribute to final parts exhibiting rough surface morphology [68], increased porosity [99], or inadequate interlayer bonding [67] around balls.
Several factors influence the balling of single melt tracks. Generally, surface tension acts between the melt and ambient gas or vapor phases, and balling arises from minimizing surface free energy through capillary forces. The high temperature range in powder bed fusion influences the process as for many materials, surface tension, and, thus, capillary forces depend on temperature. In addition, high temperature gradients at the melt surface induce Marangoni flow, contributing to the fragmentation [43]. At poor wetting conditions between liquid metal and the surrounding powder and substrate balling is further facilitated [74]. For instance, the formation of oxide films on the substrate and within the melt pool amplifies dewetting behavior [63]. Oxidation can further influence the balling process by inversion of surface tension gradients. The resulting surface flow toward the melt pool center supports melt aggregation [24]. Also, melt pool dimensions are crucial to the balling defect. At low or even the absence of melt penetration into the substrate layer, melt pools are more prone to break up. Additionally, long and narrow melt pools are susceptible to the Plateau-Rayleigh instability [134]. The formation and shape of balls themselves are influenced by the solidification rate [59] and spreading rate [145]. Due to this multitude of influencing factors, and because balling can occur at different process conditions, there are distinct and even conflicting [136] explanations of balling behavior in literature.
One common explanation for the breakup of continuous melt tracks is the Plateau-Rayleigh capillary instability [43, 47, 55, 56, 65, 67, 92, 99, 103, 104, 142]. As shown experimentally by Plateau [105] and analytically by Rayleigh [107], a liquid cylinder can break up into droplets when the wavelength of a growing disturbance exceeds the circumference of the cylinder. With regard to melt tracks, the theory is initially applied to the humping phenomenon in metal-arc welding [16]. Gratzke et al. [35] later extend it to account for the partial bound of the liquid melt. According to their stability analysis, a liquid column on a flat plate is unstable for wavelengths greater than $2/\sqrt{3}$ of the column circumference. In addition, they show that a bounded cylinder can only break up for wetting angles higher than 90 degrees. This is confirmed by the stability criterion for segmental cylinders derived by Yadroitsev et al. [134]. Meanwhile, Kruth et al. [63] find a length-to-diameter threshold of 2.1 from a surface area comparison of cylinders and spheres. Stability criteria serve as breakup conditions for continuous single melt tracks in laser-based powder bed fusion studies [57, 59, 74, 137], but their effectiveness in predicting the initiation of balling remains uncertain [96]. Significant temperature differences and, thus, varying capillary and Marangoni forces are identified to influence [99] or even be the primary driver of capillary instability [43, 104]. Besides, a low powder packing density is found to reduce the breakup length predicted by the analytical models [65]. With an increase in laser scan velocity, the ratio of melt pool length to diameter grows, making the melt pool especially susceptible to Plateau-Rayleigh instability in the high scan speed and high laser power process window [47].
When operating at low power density settings, isolated melt islands can result in balling. These melt islands form due to insufficient heating of the powder bed and, consequently, partially melted particles. The resulting melt pool tends to aggregate rather than wet the surface [108]. Ge et al. [32] identify two

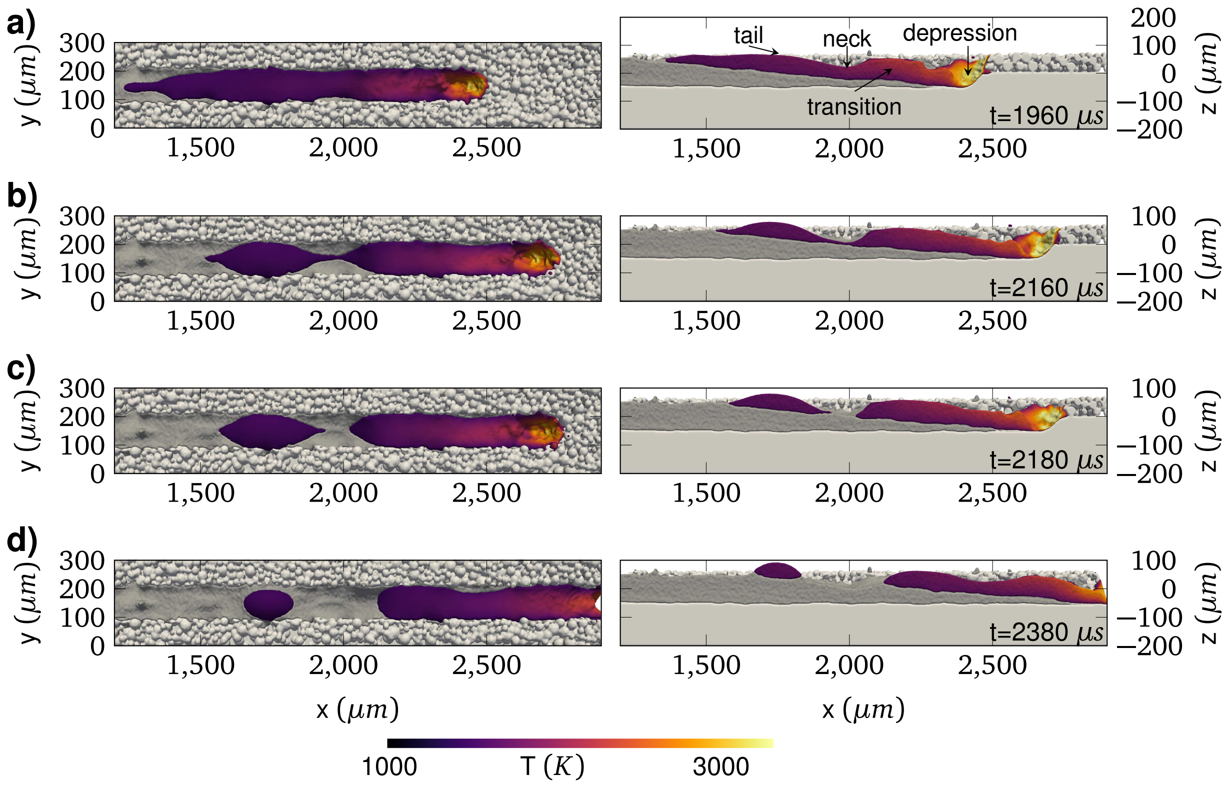

Figure 2.1: Top view and longitudinal cross section view of single melt track balling process at time instances a) $t = 1960\ \mu s$, b) $t = 2160\ \mu s$, c) $t = 2180\ \mu s$ and d) $t = 2380\ \mu s$ after the irradiation start.

types of partially melted powder particles. Semi-spherically melted particles attract the melt pool from its center toward the powder and thus facilitate breakup and melt accumulation. On the other hand, melt from almost fully melted particles tends to flow into the melt pool, causing no pool deformations. For low power input, Gu et al. [42] find substrate to melt only in regions where no powder is present. In such regions, surface tension pulls the melt toward the pool. However, insufficient remelting of the substrate beneath the powder leads to aggregation of the small pools of partially melted particles instead. In addition, at low melt temperatures, high viscosity and surface tension further facilitate the process [31, 68, 143]. Track distortions and melt agglomeration cause increased surface roughness and decreased dimensional accuracy [32]. To avoid balling under these conditions, an increase in energy input [31] or reduction of powder layer thickness [136] is suggested.

Balling at low scan speeds and high energy input, where large amounts of liquid metal are present, is called 'self balling' [72, 142]. The high energy content within the melt pool increases the solidification time and simultaneously the time scale at which surface tension affects pool breakup [59].

Balling is particularly affected by wetting and remelting of the substrate layer. The inability of melt to properly wet the underlying solid material amplifies its agglomeration [61, 67, 142]. The resulting rough surface morphology of the melt track, in turn, impacts the wettability of the consecutive melt track and enhances balling [74]. Liu and Guo [77] state that a low surface tension between the melt and gas phase facilitates an excellent ability to wet the substrate and thus improve melt spreading, which is found at higher energy densities. At high scan velocities, the melt pool width and thus the wetted substrate area decreases [47]. The pool instability and breakup are further driven by low melt pool penetration and melt spreading [68, 74, 134]. Remelting of the previous layer is especially important when oxide layers are present on the substrate as they decrease the wetting capability of the melt [41]. However, sufficient remelting can resolve oxide layers [63].

Oxidation, in general, is identified as a critical factor of single melt track balling [99]. With an increase of oxygen content in the ambient gas, the breakup tendency increases [99]. Oxide layer formation on melt and substrate depends on processed material and process temperature. At high energy density, the affinity of oxidation increases as temperatures are high. However, at the same time, increased remelting of the substrate leads to the destruction of already present oxide layers [63, 104]. While for many materials, temperature-dependent surface tension induces a Marangoni flow towards the cooler edges of the melt pool, oxidation can reverse this convection toward its hotter center [24, 99, 104]. Additionally, oxidation can decrease surface tension, e.g., for AlSi10Mg by 20 percent [24], and change its temperature dependence [99]. As a remedy, anti-oxidative alloying elements can be added to reduce the adverse effects on balling [41].

After melt pool breakup, a ball forms following a competitive non-equilibrium process between melt spreading and solidification [45, 77, 145]. Capillary forces, inertia, solidification, thermal properties, and heat content all contribute to the resulting droplet shape [145]. If melt can spread out before it solidifies, balling is avoided. However, strong cooling rates can terminate the spreading prematurely [45]. Schiaffino and Sonin [114] find a melted droplet to spread on a solid substrate only when its dynamic wetting angle is larger than the angle of the solidification front. From an isothermal analysis of spreading, Zhou et al. [145] show that the spreading time depends on the melt density, droplet radius, and surface tension. Further influencing factors such as thermal properties, solidification, process variables, surface roughness, or contaminants are discarded. The competing time scale of solidification follows from an estimate of cooling superheated liquid to its phase change temperature [30]. These time estimates agree with single melt track experiments by Guo and Zhou [45], where balling and contact angles above 90 degrees are found only for melt tracks where the spreading time exceeds the solidification time.

In a study on balling, I investigated the entire process, from powder melting to pool beak-up and ball solidification. A regime of considerate substrate remelting is explored to better understand the process window restriction due to balling at high power and scan speed settings. Unlike the commonly applied grid-based approaches, this study uses a Smoothed Particle Hydrodynamics multiphase model, offering a novel and natural treatment of the complex interface dynamics involved in balling. Through simulations with Inconel 718 powder, validated against experimental data, the study successfully predicts balling behavior. It identifies critical regions and driving forces within the melt pool, particularly highlighting the roles of capillary and Marangoni forces. The findings provide deeper insights into balling mechanisms, such as the onset of necking and its influence on final ball size. The SPH model proves robust for the simulation of powder bed fusion processes.

2.3 Laser Beam-Shaping

Beam shape refers to the spatial distribution of the laser intensity. The current industrial standard in powder bed fusion of metals are Gaussian laser beams with spot diameters between 40 and 140 μm [98]. Characterized by a prominent central intensity peak and a sharp radial gradient, Gaussian laser beams exhibit an intensity profile that may lead to overheating and substantial temperature gradients within the melt pool. As a result, the emerging evaporation and Marangoni flow form a highly dynamic melt pool [98]. Consequently, using the standard Gaussian laser profile is associated with melt pool fluctuations, spatter, balling, and powder denudation [98]. Additionally, the energy input influences temperature distribution and cooling behavior, thus solidification and the microstructure [124]. In beam-shaping, adjustments are made to the laser profiles to achieve enhanced process stability and targeted process behavior. One approach to adjust the energy input is defocusing the laser beam. This lowers the peak intensity while maintaining the same profile shape. However, the beam diameter is more sensitive to disturbances at a significantly defocused state, which is also associated with process instabilities [98]. Instead, different laser beam modulation techniques can be used to adjust beam shape. In static beam-shaping, the optical path is commonly adjusted by Diffractive Optical Element (DOE) or lenses [10, 39, 87, 98]. DOEs use specific microstructure surface reliefs to diffract light into the desired shape. For example, M-shapers can modulate a donut beam shape [132]. Lens systems can alter the beam intensity depending on their shape. For example, axicons are applied to form Bessel beams [124, 125], and cylindrical lenses are used to generate elliptical beam shapes [110]. Refractive optical systems such as pi-Shapers for flat-top or donut profiles [101, 144] or anamorphic prism pairs for elliptical profiles [111] are used. Besides static modulators, dynamic systems exist that change the spatial beam shape in time [87, 98]. Approaches include liquid crystal light modulators [10], acousto-optic deflectors [38], deformable mirrors with piezo-electric actuation [87], and in-source dynamic shapers, for example, with multiple-core fiber lasers [98].

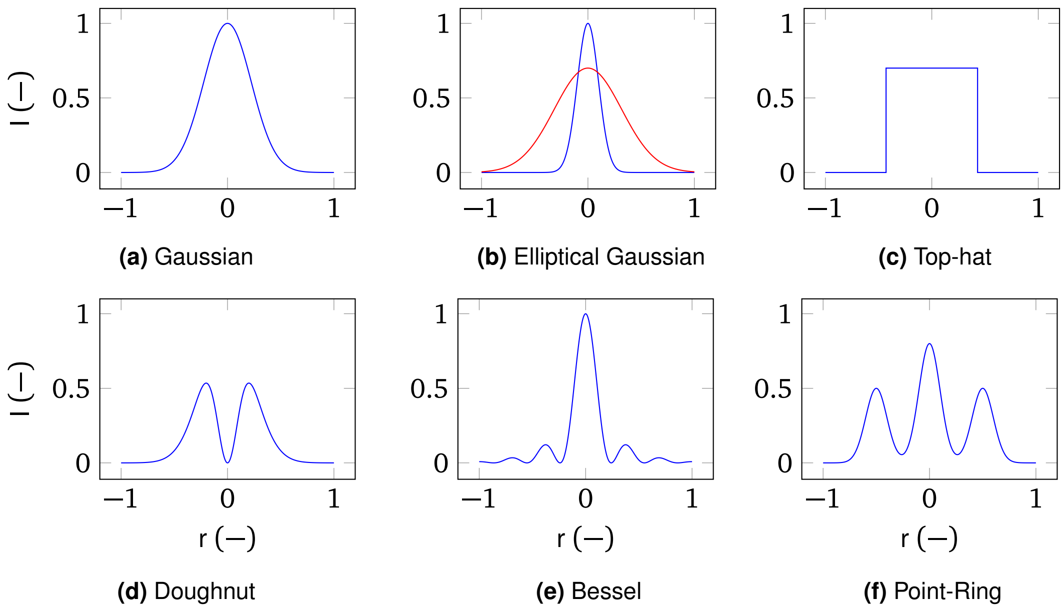

Figure 2.2: Schematic illustration of intensity distribution I over the radial distance from the beam center r for common beam profiles.

Fig. 2.2 shows an example of a Gaussian as well as common axisymmetric alternative beam shapes currently under investigation, namely, the elliptical Gaussian profile [1, 87, 110, 111, 118], top-hat profile [101, 119, 144], doughnut profile (inverse Gaussian) [37, 132], Bessel profile [124], and point-ring profile [39, 98, 112].

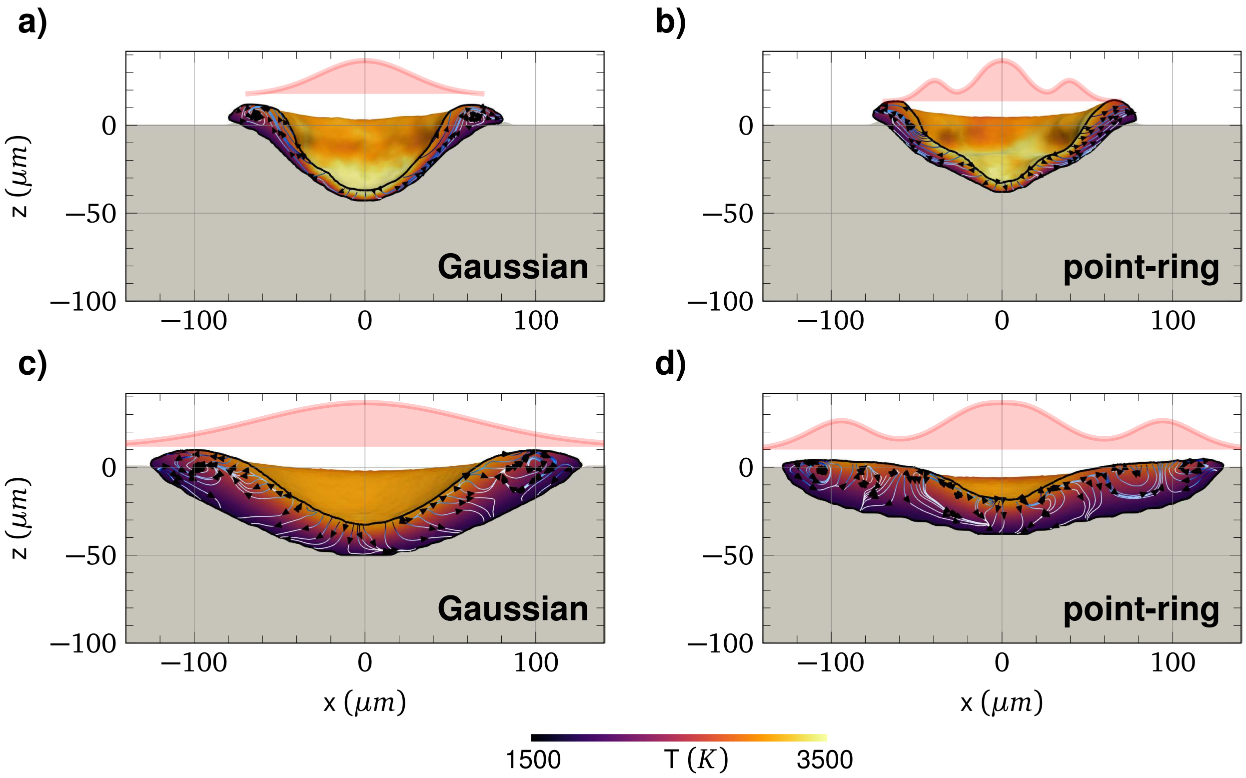

Figure 2.3: Cross section view of melt pool after $t = 42.5$ μs irradiation with a) Gaussian profile of 107 μm spot diameter, b) VBPP4 profile of 107 μm spot diameter, and after $t = 250$ μs irradiation with c) Gaussian profile of 253 μm spot diameter, and d) VBPP4 profile of 253 μm spot diameter.

Research shows that beam-shaping has a significant influence on the process behavior. Adjusted profiles lead to reduced temperature gradients on the melt pool surface [1, 125] and evaporation [37, 131]. Correspondingly, shape [118] and size [87, 118, 132] of melt tracks can be varied. Shaped laser beams reduce defects and increase the printable process window [111, 124, 132]. Appropriate selection of the beam shape reduces the amount of spatter [119, 124] and the zone of powder denudation [101], highlighting its potential for local alloying. Through thermal and spatial variation of the melt pool beam-shaping shows potential for targeted microstructure generation and thus tailored material properties [110, 111, 144]. In Fig. 2.3, exemplarily, two beam-shapes of identical width and energy input are compared. Clearly, the dimensions and temperature profile of the melt pool are strongly affected by the beam profiles.

Part of my research focuses on the beam-shaping impact of a point-ring intensity profile. Modern beam-shaping systems allow partial intensity distribution to a central Gaussian spot and an outer ring. The profile proved to expand the process window with less humping, key-holing, hot cracking, and spatter compared to the Gaussian beam [38, 39, 98, 112].

2.4 Governing Equations

The transient conservation laws of mass, momentum, and energy describe the laser-based powder bed fusion process behavior at the micro-scale. This work considers three phases: solid Ω_s, liquid Ω_l, and gas Ω_g. For Newtonian fluids, the set of equations in Lagrangian form reads

$$\frac{d\rho}{dt} = -\rho\ \nabla \cdot \mathbf{v} \quad \text{in} \quad \Omega_l \cup \Omega_g, \tag{2.1}$$

$$\rho \frac{d\mathbf{v}}{dt} = \mathbf{F}^p + \mathbf{F}^\nu + \mathbf{F}^\sigma + \mathbf{F}^\theta + \mathbf{F}^{ev} + \mathbf{F}^g \quad \text{in} \quad \Omega_l \cup \Omega_g, \tag{2.2}$$

$$\rho \frac{dh}{dt} = Q^\lambda + Q^{ev} + Q^l \quad \text{in} \quad \Omega_l \cup \Omega_g \cup \Omega_s, \tag{2.3}$$

where ρ, $\mathbf{v}$ and h are density, velocity, and enthalpy, respectively. Acceleration due to pressure ($\mathbf{F}^p$), viscous ($\mathbf{F}^\nu$), surface tension ($\mathbf{F}^\sigma$), wetting $\left(\mathbf{F}^\theta\right)$, recoil pressure ($\mathbf{F}^{ev}$) and gravity ($\mathbf{F}^g$) forces are considered. The changes in enthalpy are induced by thermal diffusion $\left(Q^\lambda\right)$, evaporative cooling (Q^{ev}) and laser energy deposition $\left(Q^l\right)$.
The pressure force follows from gradients within the pressure field p as

$$\mathbf{F}^p = -\nabla p. \tag{2.4}$$

Due to the extensive temperature range, viscosity differs significantly throughout the melt pool. The divergence of the strain rate tensor determines the viscous forces. When assuming a divergence-free velocity field, they follow to

$$\mathbf{F}^\nu = \nabla \cdot (\mu \nabla \mathbf{v}), \tag{2.5}$$

where μ is the temperature-dependent dynamic viscosity. At the melt gas surface both the interface normal capillary and interface tangential Marangoni forces are present in the form

$$\mathbf{F}^\sigma = [\sigma\kappa\mathbf{n} + \nabla_s \sigma]. \tag{2.6}$$

Here, σ, κ, $\mathbf{n}$, and ∇_s are the surface tension coefficient, interface curvature, interface normal vector, and surface tangential gradient operator, respectively. The wetting of the melt on the substrate and powder is modeled using the static Young's equation. A formulation with the current wetting angle θ and equilibrium wetting angle θ_{eq} reads [54]

$$\mathbf{F}^\theta = \sigma\left(\cos\theta_{eq} - \cos\theta\right)\mathbf{n}. \tag{2.7}$$

The evaporation-induced recoil pressure force is expressed by the Clausius-Clapeyron equation for ideal gases assuming a constant latent heat of phase change [8]

$$\mathbf{F}^{ev} = c_1\ p_\infty \exp\left(\frac{\Delta H_{mol}}{R}\left(\frac{1}{T} - \frac{1}{T_{ev}}\right)\right). \tag{2.8}$$

Its parameters are the coefficient $c_1 = 0.54$, ambient pressure p_∞, molar latent heat of evaporation ΔH_{mol}, universal gas constant R, temperature T and boiling temperature T_{ev}, respectively [8]. Gravity g acts as body force

$$\mathbf{F}^g = -\rho\mathbf{g}. \tag{2.9}$$

Energy diffusion within the different phases is considered by Fourier's law of thermal conduction

$$Q^{\lambda} = \nabla \cdot (\lambda \nabla T), \tag{2.10}$$

where λ is the respective thermal conductivity. Evaporation of material has a cooling effect on the melt surface. The mass flux of evaporation is approximated by

$$J_{ev} = c_2\, c_3\, p_r \sqrt{\frac{M}{2\pi R\, T}}, \tag{2.11}$$

where the coefficient $c_2 = 0.82$ and the sticking coefficient $c_3 = 1$ are chosen according to [8]. In Eq. (2.11), p_r is the recoil pressure, and M is the atomic mass of the evaporating material. Then, the vapor enthalpy flux follows as

$$Q^{ev} = -A\ (h + h_{ev}) J_{ev}. \tag{2.12}$$

Here, both the enthalpy h and the specific heat of evaporation h_{ev} are included. This heat sink is applied at the melt and ambient gas phase interface. Laser energy deposition on the solid and melt surface is considered by

$$Q^{l} = -\alpha\, \Omega A\, I. \tag{2.13}$$

The rate of energy absorbed by the material depends on the irradiated surface area A, absorptivity α, and Fresnel factor Ω. With Schlick's approximation $\Omega = 1 - (1 - \cos(\phi))^5$, no knowledge of the material's complex refractive indices is required. Instead, absorption depends on the incident angle ϕ between laser light and surface normal vector only [115]. Laser power is emitted following a specific intensity profile I. The current industrial standard are laser beams, where the laser power P is distributed following a Gaussian function

$$I = \frac{2\,P}{\pi r_s^2} \exp\left(-2\left(\frac{r - r_0}{r_s}\right)^2\right). \tag{2.14}$$

Here, r_s, r_0, and r are laser spot radius, laser axis location, and radial coordinate, respectively. Other intensity distributions are, however, studied as well.

The liquid-solid phase change is incorporated by assigning material to either the liquid or solid phase based on its enthalpy. Solid is melted once its enthalpy surpasses the liquidus enthalpy, including latent heat of phase change. Contrary melt solidifies once its enthalpy falls below the solidus enthalpy after the latent heat of phase change is released. During the phase transition, the temperature is updated either via a material model or the apparent heat capacity approach [27]. Material models can directly link the enthalpy to a corresponding temperature via an enthalpy-dependent specific heat capacity

$$T(h) = h / c_p(h). \tag{2.15}$$

The apparent heat capacity approach for non-isothermal phase change is applied if no material model is available. Here, the temperature is changed linearly between solidus and liquidus temperature. Latent heat of phase change is accounted for by an increased heat capacity during the phase transition, according to

$$c_p = \begin{cases} c_s & h < h_s \\ \frac{h_l - h_s}{T_l - T_s} & h_s \leq h \leq h_l \\ c_l & h > h_l. \end{cases} \tag{2.16}$$

The temperature follows from

$$T = \begin{cases} h / c_p & h < h_s \\ T_s + (h - h_s)/c_p & h_s \leq h \leq h_l \\ T_l + (h - h_l)/c_p & h > h_l. \end{cases} \tag{2.17}$$

During phase transition, a change in enthalpy will only adjust the temperature marginally due to the high heat capacity. To account for the flow behavior within the mushy zone, the viscosity is increased following [113]. Temperature dependence of solid and liquid material properties such as viscosity, thermal conductivity, laser absorptivity, and surface tension are incorporated by material-specific models from the literature.

In addition to the physical phenomena described, further effects occur during the laser beam melting process. However, these effects are considered to have minimal impact on melt pool behavior in the studies conducted and are therefore neglected. The gas is treated as a passive medium concerning the laser, meaning that the gas does not influence laser radiation, nor does the gas absorb laser energy. The shielding gas flow is disregarded; instead, the gas is modeled as an isothermal medium. For proper evaluation of the surface tension coefficient, it is calculated with the extrapolated temperature of the melt phase. Evaporation of the melt and the corresponding effects of vapor on the laser, shielding gas, and powder bed are not considered. Simplifications in the solid phase include treating powder particles as fixed, not accounting for the reduced contact thermal conductivity in the powder, and discarding solidification dynamics. Within the melt pool, viscous heating, thermal emissions, and buoyancy effects are neglected.

2.5 Smoothed Particle Hydrodynamics

The Smoothed Particle Hydrodynamics method was simultaneously introduced by both Gringold and Monaghan [34] and Lucy [79] in 1977. While initially developed for astrophysics simulations, it has since been applied to the problem of multiphase flow, microfluidics, bio-fluid mechanics, and many more [140]. In SPH, the domain is represented by a set of particles. Besides functioning as discretization points, the particles can be understood as volume elements of the material. Their mass is usually kept constant [94], which makes mass conservation throughout the simulation trivial. In contrast to mesh-based methods, no fixed neighbor connections are defined between the particles. This allows particles to move freely with the local flow field. Their movement follows the Newtonian equations of motion. By labeling particles to specific phases, the interface is implicitly known, avoiding additional capturing or tracking algorithms. In Fig. 2.4, this is demonstrated by the deformation of a square into a droplet under the action of surface tension. Particles represented by empty and full circles correspond to different phases, respectively. In SPH, governing equations are expressed through inter-particle forces and fluxes [94] determined by weighted integration over neighbor particles. The method can be formulated to be fully Lagrangian. Its fundamental features make SPH particularly well suited for deforming boundaries and interfaces [75, 89]. In addition, complex geometries are easily discretized [75] and new physics quickly adapted [89, 94].

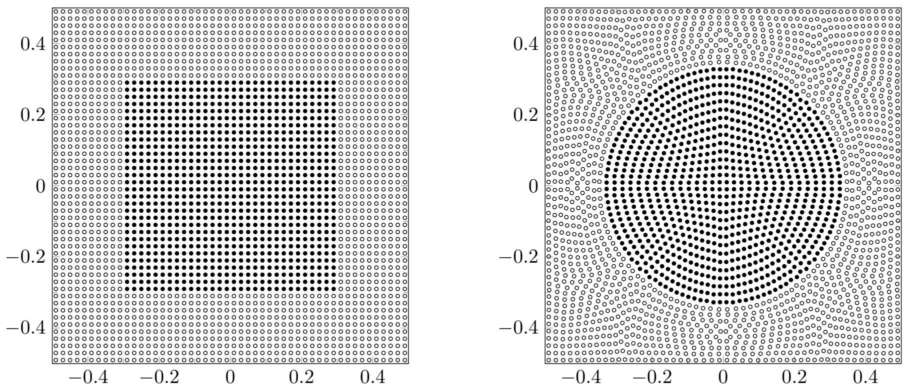

Figure 2.4: Initial (left) and steady-state (right) particle distribution of a square to droplet deformation due to the action of surface tension

Due to these inherent advantages, SPH is employed in numerous studies on the process behavior of powder bed fusion. To date, SPH schemes were applied in 2D [6, 76, 78, 113] and 3D [25, 29, 127] simulations of single track [6, 25, 70, 78, 113, 133], multi-track [11, 22, 80, 139] and multi-layer [5, 139] processes. The model accuracy is validated by comparison to experimental data. The impact of process parameters on single tracks is studied in virtual process map simulations [29, 70, 127, 133]. Surface tension and recoil pressure forces are identified as the main drivers of melt pool convection, and thus, their impact is studied closely [4, 11, 29, 76, 80]. In [29], it is shown that the melt pool is influenced more by Marangoni rather than the temperature-dependent capillary force component. Luthi et al. [80] find the Marangoni force to drive melt from the high-temperature zone towards the cooler trailing edge. Recoil pressure, in turn, is shown to produce wider and deeper melt pools [4]. The implicit interface capturing and tracking of the SPH method enables a close study of melt pool morphologies [11, 73, 76, 78, 133]. For instance, the influence of surface tension on the longitudinal wave-like surface morphology present at certain process parameter combinations was captured in [76]. Besides different defects such as porosities [85], lack-of-fusion [6], necking [6] and balling [139] are shown in SPH simulations. In [129], the thermal information from SPH single melt track simulations is coupled to analytical cracking models to identify regions and alloys of particular hot-cracking susceptibility. Some initial simulations of multi-material composites demonstrate the potential of SPH to enhance the understanding of in-situ-alloying in powder bed fusion [70, 113, 130]. With accurate information on local melt pool positions and the thermodynamics within the mushy zone, SPH can provide the required information for consecutive micro-structure predictions [13, 22, 69, 81]. For example, a study of process parameters on the grain morphology shows high scan speeds lead to smaller grain sizes and a higher content of columnar grains [81].

The initial research into laser welding by Hu et al. [49, 50] had already demonstrated the suitability of SPH models to predict melting processes at the micro-scale. Following this research, models were developed to simulate the extensive physical phenomena of laser beam melting. Thermal expansion and buoyancy-driven convective flow are incorporated by equation of state models and the Boussinesq approximation [6, 25, 76, 113, 139]. Surface tension effects are modeled by the continuous surface approach. Both capillary and Marangoni forces are considered either through the Continuous Surface Force (CSF) [6, 11, 25, 29, 69, 70, 76, 78, 81, 113] or the continuous surface stress [117, 127] formulation. Wetting behavior at the melt substrate gas triple line is commonly accounted for by solving Young's equation [70, 73, 80, 81, 85, 133]. Evaporation occurring at high energy densities is modeled by a recoil pressure force applied at the melt surface [4, 22, 70, 80, 85, 117, 127, 133]. Several models of varying complexity exist to account for the energy deposition of laser beams. Common models include simple volume and surface heat sources [5, 6, 11, 29, 69, 70, 78, 80, 81, 127], models incorporating shading [25, 113] and more advanced ray tracing schemes [13, 22, 73, 117]. To ensure stability and accuracy of numerical results, the algorithms often include additional terms incorporating artificial viscosity [80, 81, 113, 117, 133], mass-diffusion [6, 73, 78, 80, 113, 139], artificial-stress [81, 133], shifting-schemes [78, 133] as well as kernel and kernel gradient corrections [29, 78, 80]. To reduce the computational demand, researchers have introduced multi-resolution schemes where the resolution is increased within a fixed frame around the laser beam [6], within the powder layer [78], or changes dynamically [80]. Further, SPH algorithms are coupled with other discretization schemes to enhance their capabilities. The generation of accurate particle distributions within the powder bed is often modeled by the Discrete Element Method (DEM) while for the consecutive melting and solidification, SPH is applied [5, 11, 22, 81, 139]. In microstructure predictions made by Cellular Automata (CA) [13, 81] or FEM [69] simulations, SPH results provide the required position and thermal information.

This comprehensive body of work highlights the significant advancements in modeling powder bed fusion processes through the SPH method. It follows a introduction to the main concepts of SPH and to the relevant models for process simulation.

2.5.1 Basics

SPH is based on the mathematical identity

$$\psi(\boldsymbol{r}) = \int_\Omega \psi(\boldsymbol{r}')\delta(\boldsymbol{r}-\boldsymbol{r}')d\boldsymbol{r} \tag{2.18}$$

for a given continuous field function ψ within the domain Ω. With the Dirac delta function,

$$\delta(\boldsymbol{r}-\boldsymbol{r}') = \begin{cases} 1, & \boldsymbol{r}=\boldsymbol{r}' \\ 0, & \boldsymbol{r}\neq\boldsymbol{r}' \end{cases} \tag{2.19}$$

an integral formulation exists that gives the exact evaluation of the field function at the position vector $\boldsymbol{r}$. As stated in Eq. (2.18), the identity is not applicable to numerical methods. The fundamental approach of SPH is to replace the Dirac delta function with a smoothing kernel. The field function is then approximated by

$$\psi(\boldsymbol{r}) \approxeq \int_\Omega \psi(\boldsymbol{r}')W(\boldsymbol{r}-\boldsymbol{r}',h)d\boldsymbol{r}, \tag{2.20}$$

with a kernel function W and smoothing length h. Thus, a field value at a certain position is determined by a convolution of the field and kernel. Appropriate smoothing functions usually share the following properties. First, the normalization condition

$$\int_{\Omega} W(\boldsymbol{r}-\boldsymbol{r}',h)d\boldsymbol{r} = 1, \tag{2.21}$$

ensures integration over the domain results in unity. Second, the Dirac limit

$$\lim_{h\to 0} W(\boldsymbol{r}-\boldsymbol{r}',h) = \delta(\boldsymbol{r}-\boldsymbol{r}'), \tag{2.22}$$

where in the limit of the smoothing length approaching zero, the kernel approaches the Dirac delta function. The third and final property is the compact support

$$W(\boldsymbol{r}-\boldsymbol{r}',h) = 0 \quad \text{for} \quad \left|\boldsymbol{r}-\boldsymbol{r}'\right| > \kappa h, \tag{2.23}$$

reducing computational demand by limiting integration to the support domain of the kernel. Here, κ is a constant, and κh defines the support radius of the kernel. The smoothing length can be understood as a parameter defining the rate of decay of the smoothing function [106]. Increasing the smoothing length will increase the weight of more distant locations; conversely, decreasing the smoothing length will increase the weight in proximity. A typical kernel function choice is Gaussian-like differentiable, symmetric functions with monotonic decay in the radial direction. Among the most prominent kernels are the cubic, quartic, and quintic B-splines functions [88, 89, 106]. With increasing order, their approximation of the Gaussian function improves as their support domain increases.
When applying numerical methods to differential equations, such as the conservation equations of fluid mechanics, spatial derivatives need to be provided. In SPH, the differential operation is shifted from the field function to the kernel [75], giving

$$\nabla\psi(\boldsymbol{r}) \approxeq \int_{\Omega} \psi(\boldsymbol{r}')\nabla W(\boldsymbol{r}-\boldsymbol{r}',h)d\boldsymbol{r}. \tag{2.24}$$

Gradients can thus be found by convolution of the field and kernel gradient. As standard kernel functions are differentiable, exact analytical solutions for their derivatives can be found.
Moving from the continuous to the discrete space, the integral interpolants become summation interpolants. A function and its gradient are then evaluated by

$$\psi(\boldsymbol{r}) \approxeq \sum_j \frac{m_j}{\rho_j}\psi(\boldsymbol{r}_j)W(\boldsymbol{r}-\boldsymbol{r}_j',h), \tag{2.25}$$

and

$$\nabla\psi(\boldsymbol{r}) \approxeq \sum_j \frac{m_j}{\rho_j}\psi(\boldsymbol{r}_j)\nabla W(\boldsymbol{r}-\boldsymbol{r}_j',h), \tag{2.26}$$

the weighted summations over a set of disordered points. Differential volume element $d\boldsymbol{r}$ is replaced by the finite volume of particle j, expressed here as the fraction of particle mass m_j and density ρ_j. Note that this formulation of the spatial derivative is not zero-order consistent, i.e., the gradient of a constant field is not zero. As a remedy, identity

$$\nabla\psi(\boldsymbol{r}) = \frac{1}{\xi}\left(\nabla\left(\xi\psi(\boldsymbol{r})\right) - \psi(\boldsymbol{r})\nabla\xi\right) \tag{2.27}$$

with the free field function ξ, is commonly applied instead [89]. The SPH discretization follows to

$$\psi(\boldsymbol{r}) \approxeq \frac{1}{\xi(\boldsymbol{r})}\sum_j \frac{m_j\xi_j}{\rho_j}\left(\psi(\boldsymbol{r}_j)-\psi(\boldsymbol{r})\right)\nabla W(\boldsymbol{r}-\boldsymbol{r}_j',h). \tag{2.28}$$

However, Eq. (2.28) loses its anti-symmetric form and, thus, violates conservation when employed for the approximation of the momentum conservation law. The introduced set of equations forms the basis of the SPH method.

2.5.2 Density Equation

The density field at the position of particle i can simply be derived by substitution of the field ψ in Eq. (2.25):

$$\rho_i = \sum_j m_j W_{ij}. \tag{2.29}$$

For brevity, the index notations $\rho(\boldsymbol{r}_i) = \rho_i$ and $W_{ij} = W(\boldsymbol{r}_i - \boldsymbol{r}_j, h)$ are introduced here. In this equation, the mass of neighbor particles j is smoothed to evaluate the density at the position of particle i. Besides this basic formulation, two important alternative density summations exist. By rewriting Eq. (2.29) as

$$\rho_i = \rho_i \sum_j V_j W_{ij}, \tag{2.30}$$

neighbor particles contribute only with their volume rather than their mass. Alternatively, it can also be considered that particles merely contribute by their distribution [51]. Applying this concept to the density equation yields

$$\rho_i = m_i \sum_j W_{ij}. \tag{2.31}$$

Note that even for high density differences between particles, Eq. (2.30) and Eq. (2.31) will still give sharp results at interfaces. Hence, the two formulations are particularly well-suited for multiphase algorithms.
In the context of fluid mechanics, density can also be evaluated by the solution of the continuity equation (2.1). The straight forward substitution of Eq. (2.28) yields

$$\frac{d\rho_i}{dt} = \sum_j m_j \left(v_j - v_i\right) \nabla_i W_{ij}, \tag{2.32}$$

where ξ was chosen as ρ. Due to the applied gradient formulation, a constant velocity field will show no variation in density. Again, considering a volume or distribution-based approach will give better results for flow scenarios with high density differences [20].

2.5.3 Equation of Motion

Gringold and Monaghan [33, 88] have shown that the equation of motion for SPH particles can be directly derived from a Lagrangian. The resulting equation depends only on the choice of particle contribution via their mass, volume, or distribution, respectively [106]. In the following, an equation of motion is derived based on the concept of no mass contribution of neighbor particles. Derivations based on mass and volume contribution can be found in [33, 90] and [91, 106], respectively.
The Lagrangian

$$L = T - V, \tag{2.33}$$

is the difference between kinetic, T, and potential, V, energy. The equation of motion follows from the Euler-Lagrange equation

$$\frac{d}{dt}\left(\frac{\partial L}{\partial \boldsymbol{v}}\right) = \frac{\partial L}{\partial \boldsymbol{r}}. \tag{2.34}$$

The SPH Lagrangian has the form

$$L = \sum_k m_k \left(\frac{1}{2} \boldsymbol{v}_k^2 - u_k(\rho_k) \right), \tag{2.35}$$

with particle mass m_k, velocity $\boldsymbol{v_k}$, and internal energy $u_k(\rho_k)$ of all particles k in the domain, respectively [91, 106]. Then, the left and right-hand side of the Euler-Lagrange equation for particle i follow to

$$\frac{d}{dt}\left(\frac{\partial L}{\partial \boldsymbol{v}_i} \right) = m_i \frac{d\boldsymbol{v}_i}{dt} \tag{2.36}$$

and

$$\frac{\partial L}{\partial \boldsymbol{r_i}} = -\sum_k m_i \left(\frac{\partial u_k(\rho_k)}{\partial \rho_k} \right) \frac{\partial \rho_k}{\partial \boldsymbol{r}_i}, \tag{2.37}$$

respectively. Here, mass m_k was substituted by mass m_i, following the assumption of no mass contribution by neighboring particles.
The change of inner energy with density is determined from the first law of thermodynamics

$$dU = TdS - pdV, \tag{2.38}$$

with the thermal energy TdS and work of volume change pdV. Using the volume expression $V = m/\rho$ and assuming constant entropy S, the change in inner energy is given by

$$\frac{\partial U}{\partial \rho} = \frac{mp}{\rho^2}. \tag{2.39}$$

Now, substituting density by $\rho = m/V$ again and using quantities per unit mass yields,

$$\frac{\partial u}{\partial \rho} = \frac{pV^2}{m^2}. \tag{2.40}$$

So far, no SPH approximations have been applied in the derivation. Now, the gradient of SPH density summation, Eq. (2.31), is used to evaluate the density gradient at particle k with respect to particle i

$$\frac{\partial \rho_k}{\partial \boldsymbol{r}_i} = m_i \nabla_i W_{ik} + m_i \sum_j \nabla_i W_{ij}. \tag{2.41}$$

Introducing the discrete Dirac delta functions δ_{ki} and δ_{ji} Eq. (2.41) can be rewritten to [106]

$$\frac{\partial \rho_k}{\partial \boldsymbol{r}_i} = m_i \sum_j \nabla_i W_{kj} (\delta_{ki} - \delta_{ji}). \tag{2.42}$$

Substituting Eq. (2.40) and Eq. (2.42) in Eq. (2.37) yields

$$\frac{\partial L}{\partial \boldsymbol{r}_i} = \sum_k \sum_j m_i m_i \frac{p_k V_k^2}{m_i^2} \nabla_i W_{kj} (\delta_{ki} - \delta_{ji}), \tag{2.43}$$

which can be rearranged to

$$\frac{\partial L}{\partial \boldsymbol{r_i}} = \sum_j m_i m_i \frac{p_i V_i^2}{m_i^2} \nabla_i W_{ij} + \sum_k m_i m_i \frac{p_k V_k^2}{m_i^2} \nabla_i W_{ik} \tag{2.44}$$

Assuming summation over all particles of the domain, i.e., the same set of particles j and k, the equation of motion for particle i finally yields,

$$m_i \frac{d\boldsymbol{v}_i}{dt} = \sum_j \left(p_i V_i^2 + p_j V_j^2 \right) \nabla_i W_{ij}. \tag{2.45}$$

Note that this form of the equation of motion corresponds to the form derived in [51]. In the derivation, particle contribution by mass was discarded by substituting neighbor particle masses with the mass of particle i. When, instead, particles are chosen to contribute by their mass or volume, the equation of motion takes the form

$$\frac{d\boldsymbol{v}_i}{dt} = \sum_j m_j \left(\frac{p_i}{\rho_i^2} + \frac{p_j}{\rho_j^2} \right) \nabla_i W_{ij} \tag{2.46}$$

or

$$m_i \frac{d\boldsymbol{v}_i}{dt} = \sum_j V_i V_j \left(p_i + p_j \right) \nabla_i W_{ij}, \tag{2.47}$$

respectively [91, 106]. Eq. (2.45), Eq. (2.46), and Eq. (2.47) are the three common equations of motion in SPH. Since particle density does not enter the summation in Eq. (2.45) and (2.47) they are more suitable for high density ratio multiphase flows. Note that equal inter-particle forces act between particle pairs, making all three formulations linear and angular momentum conservative. In Weakly Compressible SPH, the equation of motion, the density equation, and the equation of state ensure that density variations remain low by acting toward a homogeneous particle distribution.
In [51], Hu and Adams show that it is reasonable to approximate fields by their inter-particle-averaged values in the summation. Applying this approach to the equation of motion yields

$$m_i \frac{d\boldsymbol{v}_i}{dt} = \sum_j \left(V_i^2 + V_j^2 \right) \overline{p}_{ij} \nabla_i W_{ij}, \tag{2.48}$$

with the average pressure $\overline{p}_{ij}$ of particles i and j. One example of an inter-particle pressure,

$$\overline{p}_{ij} = \frac{\rho_i p_j + \rho_j p_i}{\rho_i + \rho_j}, \tag{2.49}$$

is derived from considering a continuous pressure force at the interface between phases with different densities [53].

2.5.4 Momentum Equation

In fluid mechanics, motion is governed by the momentum equation, as stated in the Lagrangian form in Eq. (2.2). Discretization of the pressure force term directly follows from the derivation above.

Viscous Forces

To account for the acceleration of a particle due to shear forces requires the determination of second derivatives. One possibility is to approximate the second derivative of the viscous term by a combination of SPH and finite differences approximations of first derivatives. The resulting viscous force term follows to

$$\boldsymbol{F}^{\nu} = \sum_j \left(\mu_i + \mu_j \right) V_i V_j \frac{\boldsymbol{v}_{ij}}{\|\boldsymbol{r}_{ij}\|^2} \boldsymbol{r}_{ij} \cdot \nabla_i W_{ij}, \tag{2.50}$$

with dynamic viscosity μ [94]. In multiphase problems, velocity and shear stress are continuous across the interface. From this condition, an inter-particle averaged shear stress can be formulated, with a divergence of

$$\boldsymbol{F}^{\nu} = \sum_j \frac{2\mu_i\mu_j}{\mu_i+\mu_j}\left(V_i^2+V_j^2\right)\frac{\boldsymbol{v}_{ij}}{\|\boldsymbol{r}_{ij}\|^2}\boldsymbol{r}_{ij}\cdot\nabla_i W_{ij}, \tag{2.51}$$

where viscosity follows from the harmonic mean of both phases [51]. With Eq. (2.50) and Eq. (2.51), linear momentum is conserved exactly. Alternatively, the point-wise formulation

$$\boldsymbol{F}^{\nu} = \zeta\sum_j \frac{4\mu_i\mu_j}{\mu_i+\mu_j}V_iV_j\frac{\boldsymbol{v}_{ij}\cdot\boldsymbol{r}_{ij}}{\|\boldsymbol{r}_{ij}\|^2}\nabla_i W_{ij}, \tag{2.52}$$

of Cleary [18] can be employed. Note, their form is angular momentum conservative. Here, the theoretical value of $\zeta = DIM + 2$ [36, 52] is often calibrated [18, 23].

Surface Tension Modeling

In SPH, surface tension is typically modeled through two principal methods. Based on a molecular understanding, it can be conceptualized as the collective interplay of inter-particle interactions at the phase interface. Alternatively, from a macroscopic perspective, it can be treated as a boundary condition imposed at the interface. From the former approach, the inter-particle force model is derived, where a force is defined between two particles, and the summation of these forces over neighboring particles yields the local surface tension force. Nugent and Posch [100] initially employed this approach, using a Van der Waals equation of state to introduce an inter-particle attraction force. The model was further developed by Tartakovsky [123], who introduced a short-range repulsion and long-range attraction inter-particle force. Through the repulsion term, local particle clustering is avoided. Multiple parameters and formulations for the inter-particle force have been proposed in the literature. A review can be found in [126]. To the best of my knowledge, the inter-particle approach has yet to be applied to simulations of the powder bed fusion process. Instead, the macroscopic perspective of a surface tension boundary condition is commonly employed [6, 11, 25, 29, 69, 70, 76, 78, 81, 113]. As an exact reconstruction of the interface location and geometry is cumbersome in SPH, the continuous surface approach proposed by Brackbill [15] is adopted. This approach extends the sharp surface tension boundary condition to operate within a continuous volume surrounding the phase interface. Particles within this volume contribute to the surface tension force in inverse proportion to their distance from the interface.

As the interface is captured and tracked implicitly in SPH, further modeling of the continuous surface approach concerns the extraction of geometrical information. A common approach is the introduction of a color function. This function defines a zero color field in one phase and unity in the other, with a transition zone at the interface that can be either sharp [51] or smoothed [93]. More complex formulations of this field variable exist, such as using the minimum eigenvalue of a normalization tensor [12]. Generally, any field exhibiting a distinct variation at the phase interface is applicable. This variation is utilized to determine the color gradient [51]

$$\nabla c_i = V_i\sum_j\left(c_iV_i^2+c_jV_j^2\right)\nabla W_{ij}, \tag{2.53}$$

which in turn defines the local interface's normal direction. This straightforward formulation of a color function is hence used to extract geometric information about the local surface, allowing for the evaluation of surface tension forces. The magnitude of the color gradient also defines the size of the continuous interface volume, being zero outside of it.

From the mathematical description of surface tension, the continuous surface force and continuous surface stress formulation arise. In the CSF approach, the surface tension force is determined by evaluating the surface curvature, as stated in Eq. (2.6). The curvature is derived from the divergence of local normal vectors. Two common approaches of divergence evaluation are

$$\kappa_i = \nabla_i \cdot \boldsymbol{n_i} = \frac{\sum_j \min(N_i, N_j) V_j \left(\boldsymbol{n}_i - \boldsymbol{n}_j\right) \cdot \nabla_i W_{ij}}{\sum_j \min(N_i, N_j) V_j W_{ij}} \tag{2.54}$$

by Morris [93] and

$$\kappa_i = \nabla_i \cdot \boldsymbol{n_i} = \frac{D \sum_j V_j \left(\boldsymbol{n}_i - \boldsymbol{n}_j\right) \cdot \nabla_i W_{ij}}{\sum_j ||\boldsymbol{r}_{ij}|| V_j \frac{\partial W}{\partial r_{ij}}} \tag{2.55}$$

by Adami et al. [3]. The main difference is the normalization factor. At the fringes of the continuous surface, color gradients can strongly deviate from the correct interface's normal direction, which leads to a wrong divergence. Therefore, particles at the fringes are discarded in the approach by Morris [93] by introducing

$$N_i = \begin{cases} 1, & \text{if} \quad |\nabla c_i| > \epsilon \\ 0, & \text{else} \end{cases} \tag{2.56}$$

to Eq. (2.54) with $\epsilon = 0.01/h$. To account for the loss of interface contribution, the divergence is normalized by the local number density. Adami et al. [3] derive a divergence-conserving formulation where non-full support of interface particles is accounted for by

$$f_c = \frac{D}{\sum_j ||\boldsymbol{r}_{ij}|| V_j \frac{\partial W}{\partial r_{ij}}} \tag{2.57}$$

with the dimension D and kernel gradient magnitude following $\nabla_i W_{ij} = \boldsymbol{r}_{ij}/||\boldsymbol{r}_{ij}|| \frac{\partial W_{ij}}{\partial r_{ij}}$. Both formulations have been proven to capture multiple surface tension dominated phenomena and are utilized in numerical investigations of powder bed fusion processes.

Besides determining the capillary force by evaluating local curvature, it can also be assessed via the divergence of a surface stress tensor. Lafaurie [64] defines a stress tensor

$$\Pi = \sigma \left(\mathbf{I} - \mathbf{n} \otimes \mathbf{n}\right) \delta_s \tag{2.58}$$

with the unity matrix $\mathbf{I}$ and a surface delta function δ_s being non zero at the interface only. This stress tensor comprises a product of the surface tension coefficient, surface-tangential projection matrix, and surface delta function. In the continuous surface formulation, via substitution of the color gradient, the stress tensor yields

$$\Pi_i = \sigma \left(\mathbf{I} - \mathbf{n}_i \otimes \mathbf{n}_i\right) ||\nabla c_i|| \tag{2.59}$$

where the contribution of the respective particles within the interface volume are considered via their color gradient magnitude. Morris [93] notes that the stress formulation has a trace inversely proportional to the particle spacing, which can potentially become unstable at high resolutions. As a remedy, Hu and Adams [51] reformulate the stress tensor to

$$\Pi_i = \sigma \left(\frac{1}{D}\mathbf{I} - \mathbf{n}_i \otimes \mathbf{n}_i\right) ||\nabla c_i|| \tag{2.60}$$

with a trace of zero. Eventually, the surface tension forces follow from the divergence of the stress tensor as

$$\mathbf{F}_i^{\sigma} = \nabla \cdot \Pi_i = \sum_j \left(\Pi_i V_i^2 + \Pi_j V_j^2\right) \cdot \nabla W_{ij}. \tag{2.61}$$

The relation between the CSF and CSS formulation becomes evident when considering the stress divergence

$$\mathbf{F}_i^{\sigma} = \nabla \cdot \Pi_i = \sigma_i \nabla \cdot (\mathbf{I} - \mathbf{n}_i \otimes \mathbf{n}_i) ||\nabla c_i|| + (\nabla \sigma_i)(\mathbf{I} - \mathbf{n}_i \otimes \mathbf{n}_i) ||\nabla c_i||. \tag{2.62}$$

The first term on the right-hand side corresponds to the capillary force term. With

$$\nabla \cdot (||\nabla c_i|| \mathbf{I}) = \nabla ||\nabla c_i|| = (\mathbf{n}_i \cdot \nabla) \nabla c_i \tag{2.63}$$

and

$$\nabla \cdot (\mathbf{n}_i \otimes \nabla c_i) = (\nabla \cdot n_i) \nabla c_i + (n_i \cdot \nabla) \nabla c_i \tag{2.64}$$

the CSF capillary force formulation

$$\mathbf{F}_i^{\kappa} = -\sigma_i (\nabla \cdot \mathbf{n}_i) \nabla c_i \tag{2.65}$$

is derived. The second term on the right-hand side of Eq. (2.62) describes the Marangoni force where the gradient in surface tension is projected tangential to the interface. While in the CSS formulation, Marangoni forces are implicitly considered by the stress divergence, in the CSF formulation, an additional force term

$$\mathbf{F}_i^{\kappa} = ||\nabla c_i|| \nabla \sigma_i - (\nabla \sigma_i \cdot \mathbf{n}_i) \mathbf{n}_i \tag{2.66}$$

has to be solved.
Surface tension-dominated problems are often defined by two phases with large density differences. In powder bed fusion processes, the density between melt and shielding gas can typically differ by three orders of magnitude. The formulations above apply the same force to both phases at the boundary. Consequently, a strong acceleration of the lighter phase occurs, leading to stability problems and restrictive time steps. Adami et al. [3] introduce a density-weighted color function, which shifts the surface force toward the heavier phase. This reduces the acceleration of the lighter phase, allowing for more relaxed time steps. In the CSF formulation color gradient magnitudes do not enter the divergence evaluation Eq. (2.55). Hence, the approach corresponds to a straightforward density weighting of the surface tension force Eq. (2.65).

Recoil Force

When evaporation effects are approximated by the recoil pressure approach, an additional force term is added to the momentum equation. Then, recoil force is applied as body force at the surface of the evaporating material [127]. In the continuous surface approach [15], each particle within the transition band contributes to the interface area by $A_i = V_i \, ||\nabla c_i||$, with the color gradient magnitude $||\nabla c_i||$. The recoil pressure force then yields

$$F^{ev} = 2 V_i \nabla c_i p^{ev}. \tag{2.67}$$

Factor 2 is introduced when the entire action of recoil force is applied to only one of the phases, i.e., in the case of a gas melt interface, it is reasonable to apply the force to the melt phase only [127].

Buoyancy Force

Gravitation is considered as body force term via

$$\mathbf{F}_i^g = \rho_i \mathbf{g}, \tag{2.68}$$

acting on all particles. A shift in particle position and corresponding variation in particle density and hydrostatic pressure is considered. When weakly compressibility or incompressibility is incorporated, no buoyancy effects are regarded. As a remedy, particle motion due to variations in the density field is accounted for by adjustment of the gravitation body force term. A common approach is the Boussinesq approximation [127],

$$\mathbf{F}^g = (1-\beta)\mathbf{g}\Delta T \tag{2.69}$$

where the temperature is directly coupled to the gravitational field through a thermal expansion coefficient β. In scenarios where the assumptions of the Boussinesq approach are no longer valid, buoyancy can be considered by a corrected density [122].

Equation of State

A link between the mass and momentum equation is required to close the set of equations. In truly incompressible formulations, pressure and velocity are coupled using a pressure Poisson equation. A common alternative in SPH is a relaxation of the incompressibility constraint to allow for a weak compression in the density field. A natural choice for coupling density and pressure field are the respective equations of state. However, high sound speeds and, as a result, small time steps make this physical approach numerically impractical [94]. Instead, pressure and density are coupled by a stiff, barotropic equation of state that limits fluctuations to a problem-specific range. The sound speed is chosen to be low enough to ensure reasonable time step sizes and high enough to maintain a small impact of density and pressure fluctuations on the flow problem. A common choice is Cole's equation of state [21]

$$p = \frac{c_s^2 \rho_0}{\gamma}\left[\left(\frac{\rho}{\rho_0}\right)^\gamma - 1\right], \tag{2.70}$$

with sound speed c_s, reference density ρ_0 and an exponent often chosen as $\gamma = 7$. A drawback of high exponents is the translation from small errors in the density field to large errors in the pressure field [94]. When choosing γ as unity, a simplified equation of state with proportional error translation is found:

$$p = c_s^2(\rho - \rho_0). \tag{2.71}$$

A shift in density translates to a shift in pressure and, thus, to a restoring pressure force through the coupled governing equations.

2.5.5 Energy Equation

Discretization of the energy equation closely follows the approaches introduced in the previous section.

Thermal Diffusion

In [19] Cleary and Monaghan derive with

$$Q^\lambda = \sum_j \left(\lambda_i + \lambda_j\right) V_i V_j \left(T_i - T_j\right) \partial W_{ij} / \partial r_{ij} \tag{2.72}$$

and

$$Q^{\lambda} = \sum_j \frac{4\lambda_i \lambda_j}{\lambda_i + \lambda_j} V_i V_j \left(T_i - T_j\right) \partial W_{ij} / \partial r_{ij} \tag{2.73}$$

two discretized Fourier equations that closely match the discretization of the viscous force term in Eq. (2.50) and Eq. (2.51). From the requirement of continuous heat flux at the interface between two phases with different thermal conductivities follows the harmonic mean of thermal conductivities in Eq. (2.73) just as in the case of a continuous shear-stress the harmonic mean viscosity follows in Eq. (2.51).

Evaporative Cooling

In the continuous surface approach, the cooling flux induced by material evaporation is incorporated into the energy equation of surface particles by

$$Q^{ev} = V_i ||\nabla c_i|| (h_i + h_{ev}) J_{ev}, \tag{2.74}$$

where the particle's contribution to the interface surface is considered by the fractional surface element $V_i ||\nabla c_i||$.

Laser Model

A variety of laser models of different complexity exist in literature. A popular approach uses a volumetric intensity distribution with a pre-defined penetration depth of the laser irradiation. A common choice is the Beer-Lambert approach with exponential intensity decay into the material [5, 6, 29, 69, 70, 80, 81]. Knowledge of the melt-pool surface in the continuous surface approach allows us to more closely capture the energy deposition within a deforming vapor cavity. The laser energy is then distributed to the particles according to their contribution to the continuous surface [127]. The most accurate but computationally demanding approach commonly applied in powder bed fusion simulations is ray tracing schemes [128]. Here, the laser beam is modeled as a collection of discrete rays, each carrying a fraction of its total energy [117]. Different beam shapes are modeled by distributing the respective intensity following the position of a ray within the beam profile [128]. Multi-reflections are accounted for by tracing the rays based on geometrical optics principles [50]. During each laser-matter interaction, energy is transferred to the material, causing attenuation of the ray's energy. The ray's path is tracked until its energy drops below a defined threshold [117]. Different approaches exist to determine the ray reflection point and local interface normal direction [50, 117, 128]. The material-specific normal absorbance governs the actual energy deposition. The normal absorptivity is corrected for the incident angle between laser ray and local surface normal according to the materials-specific complex refractive index [50, 117] or approximations thereof as, for instance, Schlick's approximation [115]. Finally, to avoid artifacts by local peaks, the deposited energy can be distributed between neighboring interface particles [128]. Rays are propagated during a SPH time step or in pseudo-time between two SPH time steps [50, 117, 128].

2.5.6 Boundary Conditions

Boundary conditions define interface constraints at the domain boundaries and between the fluid and solid phases. This work follows the approach by Adami et al. [2], where dummy particles are introduced at domain boundaries to ensure full support of the kernel. They are included in the density, momentum, and energy evaluation. Slip or no-slip conditions are enforced by prescribing an extrapolated fluid velocity to these particles. Penetration through solids is avoided by evaluating the appropriate pressure to the boundary particles [2]. At the domain boundaries, a constant prescribed far-field temperature is used for

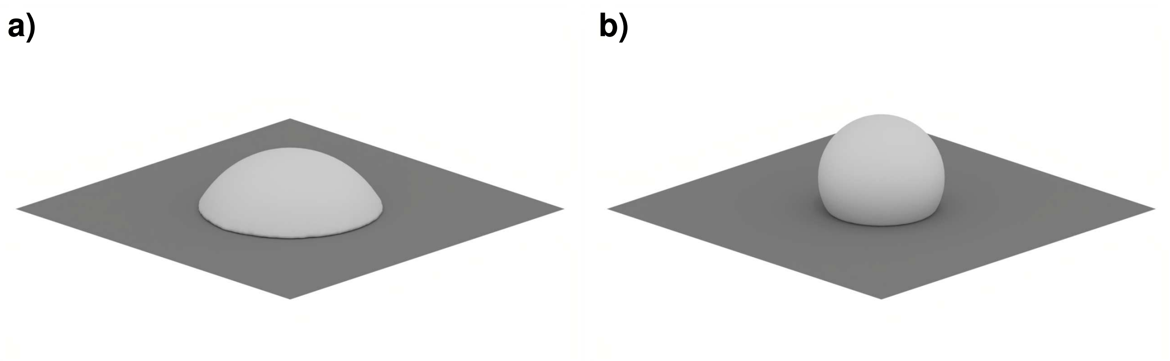

Figure 2.5: Three dimensional droplet shape for a wetting and non wetting scenario with wetting angles of a) $\theta_w = 60^\circ$ and b) $\theta_w = 120^\circ$

a Dirichlet condition to the Fourier equation.

In powder bed fusion, wetting of the liquid melt on powder and substrate significantly impacts melt pool morphology. In Fig. 2.5, the droplet shape on a wetting and non-wetting substrate is exemplary demonstrated. Special care should hence be taken to capture the behavior accurately. In the continuous surface approach, wetting can be incorporated by prescribing the normal vectors at the triple line corresponding to the target static wetting angle [15, 17]. Then, these normal vectors are used in Eqs. (2.54) and (2.66) to induce a force towards their target equilibrium. A straightforward prescription of normal vectors in the fluid phase introduces numerical artifacts, which can be reduced by a smooth transition between evaluated and prescribed normal vectors [17, 102]. Incorporating the solid phase particles in the evaluation of color gradients and forces can further improve the results [17, 26, 28, 141].

2.5.7 Time Stepping

The system of equations is advanced in time using an explicit Velocity-Verlet time integration scheme [121]. To maintain numerical stability throughout the simulation, several time-step criteria limit the maximum allowable time step. In the algorithm used in this work, the following time step constraints are taken into account. The Courant-Friedrichs-Lewy (CFL) condition

$$\Delta t \leq 0.25 \frac{h}{|\mathbf{v}_{max}| + |\mathbf{c}_{max}|} \tag{2.75}$$

where the sum of maximum flow velocity $|\mathbf{v}_{max}|$ and maximum artificial speed-of-sound $|\mathbf{c}_{max}|$ account for the maximum propagation speed of information allowed throughout the simulation. In Weakly Compressible SPH, an artificial speed-of-sound is used to restrict density fluctuations to one percent of the reference density [19, 51, 88, 95].

In addition to the CFL condition, time step criteria regarding particle acceleration by body forces [88],

$$\Delta t \leq 0.25 \left(\frac{h}{|\mathbf{a}|} \right)^{1/2}, \tag{2.76}$$

viscous diffusion [95]

$$\Delta t \leq 0.125 \frac{h^2 \rho_0}{\eta_0}, \tag{2.77}$$

surface tension [51]

$$\Delta t \leq 0.25 \min \left(\frac{\min\left(\rho^k, \rho^l\right) h^3}{2\pi\sigma^{kl}} \right)^{1/2}, \tag{2.78}$$

and thermal diffusion [19]

$$\Delta t \leq 0.125 \frac{c_p h^2 \rho_0}{k}. \tag{2.79}$$

are considered. Note, for powder bed fusion simulations the surface tension criterion becomes restrictive as the gas density has to be used in Eq. (2.78).

Chapter 3

Contributions

3.1 A partitioned continuous surface stress model for multiphase smoothed particle hydrodynamics

From the approaches for modeling surface tension forces presented in Section 2, the CSF formulation is predominantly utilized in melt pool simulations with SPH. Some of its advantages can be partially transferred to the CSS formulation, thereby combining the benefits of both models.

In [93], the continuous surface approach was first utilized to model surface tension forces in SPH, where both a CSF and a CSS model are formulated. In the CSF approach, the contribution of normals at the transition band fringes is disregarded due to their inaccurate evaluation. This is addressed by incorporating a correction term into the curvature equation. An alternative divergence approximation, with different correction term, is presented in [3]. Additionally, they introduce a sharp, density-weighted color function resulting in an asymmetric distribution of surface tension forces skewed towards the higher-density phase. This enhancement is demonstrated to improve stability and to decrease the necessary time step size.

The initial application of the CSS formulation in [93] utilizes the stress tensor formulation by Lafurie [64]. However, its divergence introduces an attractive force proportional to the surface delta function, which is inversely proportional to resolution. As this could induce instabilities at high resolutions, Hu and Adams [51] adjust the stress tensor to mitigate this potential issue. Although their formulation violates the tangential nature of surface stress [62], accurate and stable results are achieved for many surface-tension-dominated flow phenomena. While Lafuries [64] formulation theoretically could induce instabilities, several studies have found no issues with its application [36, 62, 138]. Therefore, both formulations of the stress tensor are considered good choices for the CSS model [36].

In laser-based powder bed fusion, the introduced CSF models are employed [6, 11, 25, 29, 69, 70, 76, 78, 81, 113]. In contrast, only a single SPH algorithm has been identified that utilizes the CSS formulation to model surface tension effects [127]. Nevertheless, the CSS approach has several favorable properties compared to the CSF model. Scaling the stress tensor by the color-gradient magnitude prior to divergence evaluation results in minimal contributions of erroneous color gradients at the transition band fringes. Since they are accounted for during divergence evaluation, no correction factors are necessary due to the kernel gradient's non-full support. In laser-based powder bed fusion, the Marangoni force due to surface tension gradients plays a significant role in melt pool dynamics. An additional force term in the momentum equation is required in CSF formulations. In contrast, the divergence of the CSS tensor implicitly evaluates this force component as well.

Despite these advantages, the CSF formulation remains the established approach in SPH powder bed fusion process simulations. An issue with current CSS formulations is the application of equal forces on both sides of the interface. While this ensures the conservation of linear momentum, high accelerations in lighter phases can introduce instabilities requiring a reduced time step size. Another crucial issue is the current status of wetting models for CSS formulations. In combination with the CSF approach, particularly the static wetting model has been successfully applied in powder bed fusion simulations [70, 73, 80, 81, 85, 133]. In contrast, a CSS wetting model employing a total stress tensor formulation with contributions from fluid and wall surface stresses [51] is associated with high spurious currents [27]. While these currents are reduced in a model where normal vectors are prescribed in both the fluid and wall phases, this alternative approach is computationally demanding, as it involves determining the position of the triple line to extend the interface into the wall [27].

A surface tension model that combines the advantages of the CSS formulation while incorporating the more advanced features of current CSF formulations promises a more stable and computationally efficient treatment of surface tension in simulations of laser-based powder bed fusion processes using the SPH method.

C. Zöller, N. A. Adams, and S. Adami: *A partitioned continuous surface stress model for multiphase smoothed particle hydrodynamics*, Journal of Computational Physics, Volume 472, 111716, 2023 [148]

The paper presents a novel density-partitioned continuous surface-stress model within a multiphase SPH framework, addressing critical limitations of existing CSS formulations. Firstly, the density partitioning of surface tension forces, as introduced to the CSF model by Adami et al. [3], is translated to the CSS model. A direct application of partitioning factors to surface-tension forces is incorporated as a color gradient weighting does not give satisfactory results. The stress divergence then takes the form

$$\frac{d\boldsymbol{v}_i^k}{dt} = \frac{2\rho_0^k}{\rho_i\left(\rho_0^k+\rho_0^l\right)}\sum_j V_j\left(\Pi_i^{kl}-\Pi_j^{kl}\right)\nabla W_{ij}, \tag{3.1}$$

with a scaling factor dependent on phase reference densities. Secondly, conventional speed-of-sound and time-step criteria pose constraints in surface-tension-dominated flows with high density ratios. With the density partitioning scheme, relaxed criteria suffice. Finally, we introduce a color-gradient treatment incorporating a static contact-angle wetting model at the triple line to reduce spurious currents inherent in current CSS formulations. Color gradients are adjusted for both wall boundary particles and fluid particles. Our approach aims to balance computational efficiency and accuracy when simulating wetting phenomena by introducing a simple normal extrapolation of the wetting line.

Several test cases validate all proposed adaptations. Accurate and stable results are achieved even at high density and viscosity settings. First, the impact of force partitioning on the static and dynamic interface responses to surface tension forces is investigated. The analytical solutions of the Laplace-law, capillary-wave dynamics, and thermo-capillary rise agree well with the simulation results. Notably, deviations from the reference solutions are observed as the applied surface tension force is shifted towards the heavier phase. However, these errors decline with increasing particle resolution. In addition, a significant reduction of parasitic currents in the lighter phase is achieved while maintaining the kinetic energy in the heavy phase. Thus, the density shifting scheme enhances stability even as simulations are conducted with increased time step sizes.

Finally, single droplet wetting of straight walls evaluates the CSS wall-wetting boundary condition. Droplet dimensions agree well with the analytical target over a wide range of contact angles. For extreme hydrophilic and hydrophobic wall wetting, deviations increase but are comparable to established approaches in the literature. The combined partitioning and wall-wetting model was shown to significantly reduce the kinetic energy in the system at a steady state, indicating more stable results.

Following the contributor roles taxonomy (CRediT) used by several publishers, including Elsevier, where the contribution is published, my contributions to this work comprise Conceptualization, Data curation, Formal analysis, Investigation, Methodology, Software, Validation, Visualization, and Writing - original draft.

3.2 Numerical investigation of balling defects in laser-based powder bed fusion of metals with Inconel 718

The balling defect presents a particularly challenging problem in powder bed fusion. To study this phenomenon demands not only high spatial and temporal resolutions but also the consideration of various influencing factors. Conducting experimental in-situ measurements is impractical as defining exact process conditions for the sensitive balling mechanism is cumbersome. Consequently, researchers rely on high-fidelity numerical models to understand the underlying process. However, resolving the strongly deforming multiphase flow with simultaneous phase transition necessitates utilizing a comprehensive set of numerically robust models.
Several numerical studies have tried to predict the balling process using different algorithms. The studies identified several influencing factors and enabled a close examination of the balling process. An investigation of single melt tracks with AlOx3 ceramic powder found an increased balling frequency with reduced power density [92]. A detailed analysis of flow behavior for stainless steel 316L powder at low power density revealed that the partial melting of powder particles leads to melting agglomeration and thus discontinuous melt tracks [32]. A numerical absorptivity study by Ren et al. [108] revealed that due to balling substrate rather than melt is exposed to the laser energy at low power density settings. The consequence is reduced absorbed laser energy and, thus, less melting. The power density and the powder layer properties have to be considered. While balling shows no dependence on the random powder packing, it is strongly influenced by powder layer thickness and powder size distribution [136]. Surface tension is generally identified as the driving force of balling, while inertia and viscous forces act as resistance. However, a sensitivity study of surface tension and viscosity highlights the importance of also considering coalescence times when evaluating influencing factors [14]. In addition, the substrate and oxide layers play a crucial role in pool breakup. Simulation results at different wetting conditions demonstrate a higher balling tendency at low wetting angles, which depend on these substrate surface conditions [67]. The present and prior layers were shown to contribute to the balling process. The simulations by Gu et al. [44] demonstrate how inhomogeneities in the first layers can facilitate the breakup and clustering of melt in consecutive layers.
The above studies rely mainly on traditional grid-based methods like the finite volume and finite element method in combination with phase-field, volume-of-fluid, and level-set interface algorithms. While SPH is particularly well suited for the problem, to the best of my knowledge, it has yet to be utilized in a thorough study of balling. The investigated regime is usually characterized by partially melted powder and small melt pools due to low power densities. Balling in this regime is attributed to the low amount of melt that clusters rather than forms a melt pool. However, balling also occurs in a regime where the powder is fully melted, and even a considerate substrate remelting takes place. Here, an increase in power density does not suffice to suppress balling. In this regime, balling acts as a limit to the production speed of powder bed fusion. Hence, extending numerical analysis for a better understanding is particularly important.

C. Zöller, N. A. Adams, and S. Adami: *Numerical investigation of balling defects in laser-based powder bed fusion of metals with Inconel 718*, Additive Manufacturing, Volume 73, 103658, 2023 [146]

In this publication, the balling process is studied numerically to clearly identify the contributions of driving forces. A Smoothed Particle Hydrodynamics multiphase model is used with the previously published partitioned continuous surface stress model. Single melt track simulations with Inconel 718 powder are conducted at seven process parameter combinations. The considered section of the process map is characterized by long liquid melt pools and considerate remelting of the previous substrate layer. Validation with experimental data shows good agreement of single track depths and widths. The capability to predict balling is validated by comparison of simulation and experimental data of single tracks both in the presence and absence of balling. In two different settings, the model was shown to be capable of predicting balling and non-balling behavior. Besides, the results confirm the previously reported increased tendency of disturbed track topology, inhomogeneous melt pools, and breakup at higher laser scan speeds and lower laser power.

Subsequently, the melt pool's breakup process is closely studied in terms of driving forces. Four melt pool regions are identified, namely depression, transition, neck, and tail. Balling is mainly determined in the neck and tail. Strong surface tension gradients are recorded in the depression region. They quickly decrease in the transition region and remain small in the neck and tail region. Over time, the gradients further attenuate and are small when the ball pinch-off occurs. The consequence is weak Marangoni forces acting towards melt spreading in the neck and tail region. The impact of capillary forces on the flow field is studied by measurement of the capillary pressure in the neck region. As the neck radius decreases, the pressure rises, which leads to upstream and downstream pressure gradients. The resulting convective melt flow contributes to further necking. The investigation reveals a more substantial contribution by capillary than Marangoni forces to the breakup of the melt pool.

Finally, the balling formation after melt pool breakup is investigated. The results show an initial contraction rather than a spreading of the melt pool. Before the melt can further wet the substrate surface, a solidification front has already advanced, which suppresses further wetting.

The study of balling at two different power densities reveals similar balling mechanisms yet different final ball sizes. In the regime under investigation, the final size of balls depends on the onset of necking rather than the total melt pool volume.

The presented SPH model demonstrates a more natural treatment of the complex interface dynamics of the balling process than conventional grid-based methods. The model can predict the balling process and allows a detailed analysis of influencing factors.

Following the contributor roles taxonomy (CRediT) used by several publishers, including Elsevier, where the contribution is published, my contributions to this work comprise Conceptualization, Data curation, Formal analysis, Investigation, Methodology, Software, Validation, Visualization, Writing - original draft and Writing – review & editing.

3.3 Beam-shaping in laser-based powder bed fusion of metals: A computational analysis of point-ring intensity profiles

Application of alternative beam shapes to the industrial standard Gaussian beam proof beneficial to the powder bed fusion process, i.e., temperature gradients in the melt pool can be reduced by application of transverse or longitudinal elliptical Gaussian [1] or Bessel beams [125] and the keyhole free parameter space is extended by doughnut [132] and elliptical beams. Common beam shapes under research include the Gaussian elliptical, top-hat, doughnut, Bessel, and point-ring profile.

Besides a more stable process, beam-shaping also shows the potential to advance laser-based powder bed fusion capabilities by enabling the manufacturing of locally varying alloys and targeted local material properties. This requires process control at small spatial and temporal scales. One major issue of variable alloy application is feedstock contamination due to alloy mixing. For local material properties, the micro-structure has to be tuned, i.e., by cooling rate or melt pool shape adjustments [118]. Research shows that through beam-shaping, evaporation can be reduced, and the melt pool properties can be adjusted. Hence, it can enable both locally varying alloying and local material properties.

In [119], a comparison of a large top hat beam to a small Gaussian profile shows less evaporation and spatter for the former beam shape. In addition, the top-hat profile is found to reduce the denudation of the powder bed [101]. The doughnut profile is characterized by a more uniform energy distribution than the Gaussian profile, leading to less evaporation as well [37, 132]. A spatter reduction is also found for Bessle-beams [124].

Several beam shapes are shown to influence the melt-pool shape. Elliptical beams can lead to shallow, short, and wide melt pools with larger supercooled regions compared to the Gaussian beam [118]. A large top-hat beam produces larger width-to-depth ratios [144]. Shallow and wide melt tracks are also found after the application of doughnut profiles [132]. To manufacture narrow and deep melt pools, the Bessle-beam can be used [125].

Analysis of corresponding micro-structures shows that elliptical beams lead to equiaxed and mixed equiaxed-columnar distributions for more process parameter combinations than the Gaussian profile [111]. A numerical study finds transverse elliptical beams to result in more grain nucleation and equiaxed grains [110]. The top-hat profile can be utilized for the generation of more epitaxial growth of columnar grains [144].

One promising beam shape is the point-ring profile. It consists of a central Gaussian spot and an outer ring intensity peak. Depending on the energy distribution to the central spot or outer ring, it can generate targeted melt pool behavior. In the experimental study by Nahr et al. [98], an increased process window, smoother surface topology, and less hot cracking are observed with point-ring profiles. Ultimately, the application of point-ring profiles enables faster build rates [39]. Its advantages for local alloying are demonstrated in [40] where less spatter is recorded.

Research shows that laser beam size and shape are crucial parameters for tailored powder bed fusion processes. Nevertheless, the influence of beam size on the beam-shaping effect for point-ring profiles has yet to be systematically investigated. Further, no numerical investigation into the point-ring profile is found, which allows for studying local flow dynamics and quantifying contributing factors.

C. Zöller, N. A. Adams, and S. Adami: *Beam-shaping in laser-based powder bed fusion of metals: A computational analysis of point-ring intensity profiles*, Additive Manufacturing, Volume 73, 103658, 2023 [147]

This publication studies the influence of laser beam size on the beam-shape effect for point-ring laser profiles. The numerical investigation is conducted with a high fidelity, Weakly Compressible Smoothed Particle Hydrodynamics model coupled to a laser ray-tracing scheme. Both fixed laser irradiation and single melt track simulations at the powder-scale are compared with respect to melt-pool shape, surface temperature, evaporation, and flow dynamics. The laser profiles are applied at two beam sizes and the same laser power. This allows us to research the influence of beam shape at different power densities.
First, the used models are briefly recapitulated, focusing on the physical models of evaporation and surface tension effects. The applied ray tracing scheme is summarized, and relevant simplifications are discussed.
A Ray-resolution study demonstrates accurate laser beam modeling. To resolve the pronounced intensity variations within small spatial dimensions of the point-ring profile, a resolution of 4000 rays is identified as sufficient. The whole numerical model is validated by comparison to experimental data from the literature. Good agreement is found for single melt track dimensions for both deep and narrow as well as shallow and wide tracks.
A study of fixed laser beam irradiation allows us to highlight the isolated effect of beam shape on the melt. Laser beam size impacts the energy density and thus the contribution of Marangoni and evaporation forces to the resulting melt pool. The shape then controls the distribution of these forces and the resulting melt pool shape and local dynamics. By shaping the laser beam, the forming vapor cavity can be adjusted mainly at low power densities or short irradiation times. Once deep cavities form, apparent differences between the beam profiles vanish.
Single melt track simulations show a minor impact of the beam profile on melt-pool dimensions at high energy densities. In contrast, at low energy densities, Marangoni forces lead to changes in flow direction. Depending on the power density, the beam shape is found to increase or decrease evaporation, highlighting the importance of power density in beam-shaping studies. Overall, the effect of the laser profile on global quantities, such as the melt pool size and kinetic energy within the melt pool, is small compared to the impact of laser beam size.
Power density and, thus, beam size are shown to influence the effect beam-shaping has on the melt-pool dynamics. It is essential to differentiate between size and shape effects when investigating new beam shapes. Finding the desired process behavior for local alloying or target material properties requires carefully tuning power density together with the beam shape. Furthermore, beam-shaping affects the local melt-pool dynamics at low energy densities, suggesting its potential to induce more desirable melt-pool dynamics. For the specific process parameters and beam shapes considered in the study, the beam shape has a relatively small impact on the global melt-pool dimension and overall kinetic energy.
Following the contributor roles taxonomy (CRediT) used by several publishers, including Elsevier, where the contribution is published, the contributions comprise Conceptualization, Data curation, Formal analysis, Investigation, Methodology, Software, Validation, Visualization, Writing - original draft and Writing – review & editing.

Chapter 4

Discussion and Conclusion

Laser powder bed fusion at the micro-scale is defined by multiple physical phenomena happening simultaneously while being sensitive to numerous influencing factors, making it difficult to predict and control. However, precise control is essential to prevent defects such as balling and to achieve targeted material properties. Numerical investigations offer deep insights into the process behavior and aid in developing optimized processing strategies. This, however, requires stable numerical algorithms that remain robust even during violent multiphase interactions. In this work, contributions are presented that improve the applicability of the Smoothed Particle Hydrodynamics method in process simulation. The developed surface tension model is applied to explore the underlying mechanisms of surface tension-dominated melt pool instability and balling phenomena. A particularly interesting region is analyzed, defined by high laser energy and high scanning speeds, representing the limits of processing speed. Furthermore, the model is used to study the influence of laser beam shape and size, exploring the applicability of beam-shaping to achieve targeted material properties and multi-material combinations.

In the simulation of powder bed fusion using SPH algorithms, the continuum surface force model is predominantly applied for surface tension modeling. At the same time, only a few studies have utilized the continuum surface stress formulation. This is primarily due to the current state-of-the-art model robustness and more developed boundary condition handling in the CSF model. The CSS model introduced in Section 3.1 incorporates the well-established improvement of density-weighted forces from the CSF approach. Thus, a more efficient application of the CSS approach in powder bed fusion simulations is enabled while retaining its advantages, such as reduced erroneous contributions from fringe particles and implicit consideration of Marangoni forces. Compared to the CSS formulations found in the literature, the model reduces spurious currents and allows for significantly larger time step sizes. Additionally, the introduced wetting model effectively reduces spurious currents at the triple line while also eliminating the need for complex triple-line localization. These enhancements result in a novel scheme that is robust and capable of accurately capturing both balling phenomena and beam-shaping effects.

The balling defect is one of the critical limitations in powder bed fusion, making a precise understanding of its underlying behavior necessary. While numerous numerical studies have examined the balling process in regimes characterized by insufficient powder melting, only a few numerical studies were found that investigate balling in long melt pools under full powder melting conditions, considering substrate remelting. The analysis detailed in section 3.2 confirms a surface tension-driven melt pool breakup mechanism. As the melt contracts, a reduction in surface tension gradients in the neck region indicates a decrease in Marangoni flow, leading to reduced spreading. As the curvature in the neck increases and the temperature drops, capillary forces intensify. This results in pressure-induced convective flow away from the neck region. After pinch-off, the results reveal a competing mechanism between melt contraction and spreading forces. During this initial contraction, the solidification front advances into the forming ball, suppressing further melt spreading. This initial contraction phase should be incorporated to refine existing analytical models that rely solely on the competition between spreading and solidification mechanisms for predicting meltpool balling.

Finally, the developed model was applied to investigate the influence of power density on beam-shaping effects by capturing melt pool shapes, surface temperatures, evaporation, and melt dynamics for both Gaussian and point-ring laser irradiation profiles. Experimental studies have demonstrated the potential of point-ring irradiation for enhancing process stability and enabling localized alloying. However, a detailed analysis of the interaction between beam shape, beam size, and irradiation time for the point-ring profile is not found in the literature. Additionally, no numerical studies have focused on the local melt pool dynamics induced by point-ring laser irradiation. The findings suggest that the shape of the laser beam can adjust the contributions of evaporation and Marangoni forces, thus enforcing distinct melt pool shapes and dynamic behavior. This effect is particularly pronounced at low energy densities and during the initial stages of vapor cavity formation. However, as deeper melt cavities form, the influence of beam shape diminishes, with melt pool contours and temperature distributions becoming similar between Gaussian and point-ring irradiations. This weakening of the beam shape effect is attributed to the increase in multi-reflections within the melt cavity. The results also demonstrate that beam-shaping can suppress evaporation while maintaining the same power density, highlighting its potential for precise process control. The results demonstrate the importance of selecting appropriate power densities to amplify the beam-shaping effect on the melt pool. As evaporation and melt pool morphology can be tailored through beam-shaping, it is a promising technique for localized alloying and manufacturing targeted material properties.

In conclusion, the developed SPH model has demonstrated robustness and the potential to enhance the micro-scale understanding of powder bed fusion processes. Future work should focus on extending the surface tension model to interactions between three fluid phases and improving boundary treatments for under-resolved scenarios. The model's capabilities could also be utilized to explore more complex scan path configurations, including turns, multi-track, multi-layer, and different scan strategies. Further research is needed to examine detailed interactions between single tracks and defects such as balls or pores. Lastly, coupling the thermofluid dynamic model with a microstructure model will enable deeper investigations into beam-shaping effects and their influence on targeted material properties.

Appendix A

A partitioned continuous surface stress model for multiphase smoothed particle hydrodynamics

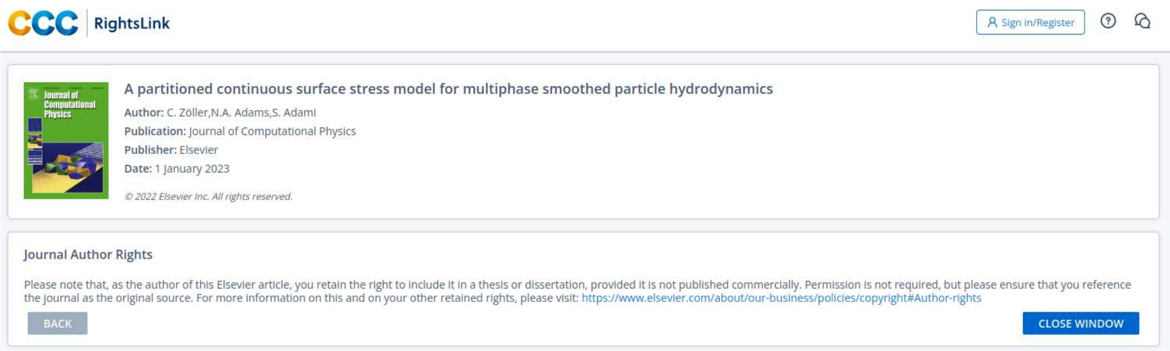
RightsLink

Sign in/Register

A partitioned continuous surface stress model for multiphase smoothed particle hydrodynamics

Author: C. Zöller,N.A. Adams,S. Adami

Publication: Journal of Computational Physics

Publisher: Elsevier

Date: 1 January 2023

Journal Author Rights

Please note that, as the author of this Elsevier article, you retain the right to include it in a thesis or dissertation, provided it is not published commercially. Permission is not required, but please ensure that you reference the journal as the original source. For more information on this and on your other retained rights, please visit: https://www.elsevier.com/about/our-business/policies/copyright#Author-rights

BACK

CLOSE WINDOW

Journal of Computational Physics 472 (2023) 111716

Contents lists available at ScienceDirect

Journal of Computational Physics

journal homepage: www.elsevier.com/locate/jcp

A partitioned continuous surface stress model for multiphase smoothed particle hydrodynamics

C. Zöller [a,b,*], N.A. Adams [a,b], S. Adami [a,b]

[a] *Technical University of Munich, School of Engineering and Design, Department of Engineering Physics and Computation, Chair of Aerodynamics and Fluid Mechanics, Boltzmannstraße 15, 85748 Garching, Germany*
[b] *Technical University of Munich, Munich Institute of Integrated Materials, Energy and Process Engineering, Lichtenbergstr. 4a, 85748 Garching, Germany*

A R T I C L E   I N F O

Article history:
Received 29 November 2021
Received in revised form 25 August 2022
Accepted 15 October 2022
Available online 24 October 2022

Keywords:
Smoothed particle hydrodynamics
Continuum surface stress
High density ratios
Capillary force
Marangoni force

A B S T R A C T

A density partitioned continuous surface-stress (CSS) model is presented within a multi-phase smoothed particle hydrodynamics (SPH) framework. We follow the original work of Adami et al. (2010) [1] to partition the surface-tension force from a zeroth-order consistent continuum surface-stress model. As a consequence of the scaled surface-tension force, both the surface-tension based artificial speed of sound and the numerical time step criteria can be relaxed for phase interfaces with high density ratio. A new color-gradient treatment and a static contact angle based surface-stress boundary condition is introduced to incorporate wetting behavior. All models are validated by comparison to analytical solutions of several surface-tension dominated flows. The resulting scheme is demonstrated to handle both capillary and Marangoni forces for high density and viscosity ratios.

1. Introduction

Accurate modeling of multi-phase flow phenomena continues to receive much attention as it offers a wide field of application yet still poses numerical challenges. Particularly, flows with high density ratios including liquid-gas interfaces such as droplets [2], bubbles [3] and melts [4] require special considerations to address discontinuous fluid states or material properties. Moreover, violent motion and large topological changes demand robust multi-phase models including interface detection and tracking. In mesh-based methods, special interface-treatment techniques such as the volume-of-fluid [5] and level-set [6] method are successfully applied to multi-phase problems. However, additional transport equations are required and special reconstruction schemes increase computational efforts. Moving meshes can struggle with distortion and folding due to complex interface deformations and require expensive remeshing [7]. In addition, adequate normal and curvature evaluation by high mesh resolutions or adaptive mesh refinement further drive computational costs. In contrast, particle-based methods such as SPH implicitly capture interfaces via the particle distribution as each particle is associated to a particular phase. Instead of fixed neighbor links as in mesh based methods, these SPH particles move freely with the flow following Newton's laws. Thus, interface tracking over time is handled implicitly. This ease of interface-treatment makes SPH an attractive discretization method for surface-tension dominated problems with complex flow topologies.

* Corresponding author at: Technical University of Munich, School of Engineering and Design, Department of Engineering Physics and Computation, Chair of Aerodynamics and Fluid Mechanics, Boltzmannstraße 15, 85748 Garching, Germany.
E-mail addresses: christopher.zoeller@tum.de (C. Zöller), nikolaus.adams@tum.de (N.A. Adams), stefan.adami@tum.de (S. Adami).

https://doi.org/10.1016/j.jcp.2022.111716

Within SPH, the two prevalent approaches to incorporate surface-tension effects are the inter particle force (IPF) and continuous surface models. The IPF formulation is motivated by a microscopic understanding of surface-tension forces induced by discrete particle interactions, while the continuous surface models capture surface-tension by a smoothed volumetric force [8]. In the original IPF model by Nugent and Posh [9] surface-tension effects are mimicked by a force arising from a cohesive pressure term in the Van der Waals equation of state. While the net attraction force vanishes in the bulk, interface particles are exposed to a resulting interface-normal force. One drawback of the method is its requirement to consider particles within a range of twice the kernel cut off radius to achieve accurate results [9]. The IPF model is enhanced by Tartakovsky et al. [10] to include a short-range repulsive and long-range attractive force contribution within the momentum equation. The initial drawback of model parameter calibration to accurately resolve the surface-tension and contact angles is addressed in a later publication [11]. An overview on different formulations for the attractive and repulsive force terms is presented in [7].

In the alternative continuous-surface force or stress approaches, volumetric surface-tension forces are added to the momentum conservation equation acting at the interface between phases. Here, the macroscopic understanding of surface-tension forces arising from a stress boundary condition is utilized. However, instead of a sharp surface, Brackbill et al. [8] represent the interface by a transition region between the phases. This transforms the surface boundary conditions to a continuous surface force. A color-function can be used to differentiate between phases. Gradients of this color-function at the interface are then employed to determine the surface normal direction. Now, the interface geometry is fully described and the surface-tension forces are evaluated. Within the continuous surface model two approaches of surface-tension modeling are established, namely the continuous surface force (CSF) and continuous surface-stress (CSS) models. A first introduction of the continuous surface force model to SPH is found in [12]. Here, a smoothed color-function is used for the evaluation of the continuous surface force at each particle. Normals at the transition band fringes are found to be erroneous, they are discarded and a correction term is added to the divergence equation. Adami et al. [1] propose a CSF model with a sharp, density-weighted color-function resulting in asymmetric surface-tension forces shifted towards the heavy phase. This force partitioning shows to enhance stability and allows to relax the numerical time step. In addition, they formulate a new divergence approximation. Both formulations of the CSF model are widely used in literature [3,7,13–15].

In the continuous surface-stress approach, surface-tension forces are not determined from curvature, but instead, as divergence of a surface-stress tensor. In [16] such a stress tensor is derived with a divergence that exactly reproduces capillary forces. An SPH representation of the CSS model is first presented by Morris [12]. It is pointed out that the stress formulation by Lafaurie et al. [16] introduces a tension proportional to the surface-delta function and, thus, inversely proportional to particle resolution. This attractive force can lead to instabilities when the resolution is increased [12]. Hu and Adams [17] therefore adjust the stress tensor to discard the negative pressure force. It is shown, that their CSS model successfully reproduces a variety of surface-tension dominated flow phenomena. Nevertheless, in [18–20] no such instability issues are raised when the surface-stress formulation by Lafaurie [16] is applied. Grenier et al. [18] state that no benefit nor disadvantages are found between the two formulations. Krimi et al. [19] point out that the adjustment of Hu and Adams [17] violates the tangential character of the surface-stress. Besides the potential instability issue for high resolutions, the CSS formulation offers several favorable properties compared to the curvature-based CSF model. First of all, the CSS approach allows to formulate a linear momentum conservative model, see [12] and [17]. Since, stress tensors are scaled by the color-gradient magnitude prior to the evaluation of their divergence, erroneous contributions by particles at the fringes of the transition band remain small. In turn, as these particles are not discarded, no special considerations concerning full support of the kernel gradient are required. In scenarios of variable surface-tension coefficients, an additional force term needs to be introduced into the CSF formulation to account for Marangoni forces [13]. In a CSS formulation, however, this contribution is implicitly evaluated by the stress divergence [21], thus reducing computational efforts. These advantages make the CSS formulation a viable alternative to the curvature-based CSF model.

Besides pure fluid-fluid interface behavior, surface-tension effects at wall contact points are of particular importance in many surface-tension driven flow scenarios. In the CSF model, wetting is commonly incorporated either by numerically enforcing normal vectors based on the static wetting angle [8] or by introducing a wall tangential force based on the difference between static and dynamic wetting angles [22]. In [8], Brackbill et al. introduce wetting behavior by prescribing normal vectors in proximity of the wetting line according to a defined static wetting angle. These normals are in turn applied in the divergence calculation of curvature. Hence, enforcing normal vectors at the wetting line induces a force on the fluid phases towards the prescribed static wetting angle. Breinlinger et al. [23] find that a sharp transition between prescribed normal vectors and non-prescribed normal vectors outside the wetting line proximity introduces a nonphysical curvature and, thus, errornous surface-tension force. As a remedy, they use a blending function based on the wall distance of SPH particles for a smooth transition between prescribed and evaluated normal vectors. This blending function is advanced in the model of Olejnik and Pozorski [24] for accurate results at super-hydrophilic and -hydrophobic wetting conditions. In contrast, Huber et al. [22] derive a contact-line model from a force balance at the triple line to study the dynamics of wetting processes. Instead of prescribing normal vectors, a wall-tangential force is applied to fluid particles in the vicinity of the wetting line. As this force is found from the difference between static and dynamic wetting forces, special dynamic wetting behavior can easily be incorporated. Breinlinger et al. [23] already point out the deficiencies when wall particles are neglected during the estimation of the near-wall color-gradients and normals. This issue is addressed in Yeganehdoust et al. [25] by adding a color-value to dummy boundary particles and including them in the color-gradient evaluation. However, their model relies on an empirical fitting parameter. Dong et al. [26] introduce virtual boundary particles as an extension of the fluid interface into the wall. Here, virtual particles are associated to the fluid phase on the respective side of the interface extension. Besides the creation of virtual particles, the model relies on an accurate evaluation of the wetting line at each time step. In the CSS formulation by Hu and Adams [17], wetting behavior is incorporated by means of a total surface-stress tensor consisting of a fluid and a wall surface-stress component. Here, the surface-tension coefficient between the wall and the fluid phase is chosen to comply with the Young Laplace theory. Farrokhpanah et al. [27] show that high spurious currents can occur with this approach. Instead, the CSS formulation is coupled with prescribed normal vectors in the fluid phases at the triple line and an extrapolation of the fluid interface. The model relies on an accurate determination of the wetting line for the subsequent extension of the interface into the wall.

Despite the mentioned advantages of the CSS model we found a lack of its application in literature in comparison to the CSF approach. One reason might be, that the CSS models presented in literature do not apply a density based surface-tension force partitioning. The resulting force distribution and subsequent particle accelerations pose strong restrictions on the time step size and speed-of-sound in surface tension dominated flows, making the partitioned CSF model [1] a more viable alternative. Secondly, the proposed wall wetting models for the CSS approach either induce significant spurious currents or require cumbersome wetting line evaluations and interface extrapolations.

In this work, we present a stable and efficient CSS formulation within a multi-phase SPH framework. Three issues of the current state-of-the-art in CSS models are addressed. First, to the best of our knowledge, no density partitioning of surface-tension forces as in the CSF model by Adami et al. [1] exists for the CSS approach. A straight-forward application of the color-gradient weighting does not suffice. Instead, we propose to apply a partitioning factor directly to the surface-tension forces. Second, in surface-tension dominated flows with high density ratio the commonly applied speed-of-sound and time step criteria become restrictive. Based on the density partitioning, we propose a relaxation of these criteria following [1]. Finally, a new color-gradient treatment and a wetting model based on the static wetting angle [23] at walls are introduced. The aim is to reduce spurious currents as seen in present CSS formulations while keeping the computational efforts low. All proposed adaptations are validated with a range of test cases. The work is organized as follows: In sec. 2, the governing conservation laws for mass, momentum and energy are introduced. Subsequently, an SPH discretization particularly well-suited for multi-phase flows is applied to these equations in sec. 3. Here, the proposed density partitioning, time step adjustments and boundary treatment are formulated. Finally, the validity and stability of the proposed model is shown in sec. 4.

2. Governing equations

In this work, the weakly compressible Navier-Stokes equations in Lagrangian form

$$\frac{d\rho}{dt} = -\rho\,\nabla\cdot\mathbf{v} \tag{1}$$

$$\frac{d\mathbf{v}}{dt} = \frac{1}{\rho}\left[-\nabla p + \mathbf{F}^{(\eta)} + \mathbf{F}^{(st)}\right] + \mathbf{g} \tag{2}$$

are applied, where ρ and $\mathbf{v}$ correspond to the density and the velocity vector, respectively. As right-hand-side terms in the momentum conservation equation, the pressure gradient $-\nabla p$, viscous force $\mathbf{F}^{(\eta)}$, surface-tension force $\mathbf{F}^{(s)}$ and body force $\mathbf{g}$ are considered. For incompressible Newtonian fluids with constant dynamic viscosity η, viscous forces follow from a Laplacian of the velocity field

$$\mathbf{F}^{(\eta)} = \eta\nabla^2\mathbf{v}. \tag{3}$$

Assuming a sharp interface, the divergence of the interface stress tensor for immiscible fluids can be expressed by a normal and a tangential surface force contribution [8]

$$\mathbf{F}^{(st)} = \nabla\Pi^{st} = -\sigma\,\kappa\,\mathbf{n} + \nabla_s\sigma, \tag{4}$$

where the normal contribution scales with the local surface curvature κ projected in normal direction $\mathbf{n}$. The tangential component follows from the surface gradient ∇_s of the surface-tension coefficient σ. In this work, such gradients in surface-tension coefficient result from a temperature dependence $\sigma(T)$. Note, besides thermo-capillary, surface-tension variations can result from other effects, such as soluto-capillary [21,28] or electro-capillary [29] effects.

Discarding the rate of body and surface work, i.e. viscous heating and surface-tension work, the energy equation reduces to the thermal conduction equation by Fourier's law. In enthalpy form this reads

$$\frac{dh}{dt} = \frac{1}{\rho}\nabla\cdot(k\nabla T) \tag{5}$$

with enthalpy h, thermal conductivity k and temperature T. Following the weakly-compressible SPH (WCSPH) approach [30], the set of equations is closed by a direct link between pressure and density through Tait's equation of state

$$p(\rho) = p_0 \left[\left(\frac{\rho}{\rho_0} \right)^{\gamma} - 1 \right]. \tag{6}$$

Here, p_0, ρ_0, and γ correspond to the reference pressure, reference density and ratio of specific heat capacities, respectively. While this barotropic equation of state does not enforce incompressibility, its parameters are chosen to limit density variations to one percent [31]. In the present work, the exponent γ is set equal to one and the reference pressure is expressed by reference density and the numerical speed-of-sound c_s as

$$p_0 = \rho_0 c_s^2. \tag{7}$$

A proper choice of the numerical speed-of-sound ensures admissible density variations [31]. Note, in multi-phase flows, phase specific properties are chosen in the evaluation of Eq. (6). By also determining a phase specific numerical speed-of-sound, we allow for a phase specific reference pressure.

3. Numerical method

The SPH discretization of the governing equations closely follows the weakly compressible multi-phase method introduced by Hu and Adams [17]. In general, within the WCSPH formulation, a particle denoted by index i represents a fluid volume V_i and carries momentum a_i, enthalpy h_i and a fixed mass m_i. Field variables are determined from weighted summations over neighboring particles j. These neighbor particles can be associated with the same phase, other phases or boundaries. Boundary conditions are incorporated by means of dummy particles as described in [32]. The SPH algorithm is implemented using OpenFPM [33] and supports multi-CPU- and multi-GPU-architectures.

3.1. Weakly-compressible SPH

In the SPH multi-phase model by Hu and Adams [17], density is evaluated via a density summation equation where neighbor particles contribute only to the number density via

$$\rho_i = m_i \sum_j W\left(\mathbf{r}_{ij}, h\right) = \frac{m_i}{V_i}. \tag{8}$$

Here, $\mathbf{r}_{ij} = \mathbf{r}_j - \mathbf{r}_i$ is the particle distance and h the constant kernel smoothing length. The sum over the kernel $W_{ij} = W\left(\mathbf{r}_{ij}, h\right)$ approximates the particle number density and is equivalent to the reciprocal particle volume. Note, Eq. (8) allows to handle large density discontinuities between phases as neighboring particles contribute only to the number density.
The choice of the kernel function has an influence on stability, accuracy and computational cost of the SPH algorithm. A kernel function should fulfill three conditions namely the partition-of-unity $\int_0^\infty W(\mathbf{r}, h) d\mathbf{r} = 1$, the Dirac delta function limit $\lim_{h\to 0} W(\mathbf{r}, h) = \delta(\mathbf{r})$ and compact support $W_{ij} \geq 0$ for $\mathbf{r}_{ij} \leq r_c$ with cut-off radius r_c [34]. A common choice are compact Gaussian-like functions with monotonic decay in particle distance (which reaches zero at the cut-off radius [30]). Within this work, a quintic spline kernel function is employed as it shows a good balance of accuracy and computational cost [35]. In all simulations the smoothing length h is set equal to the initial particle spacing Δx. For more information on kernel functions, the reader is referred to [36].

Applying the multi-phase pressure formulation by [17] yields

$$\frac{d\mathbf{v}_i^{(p)}}{dt} = -\frac{1}{\rho_i} \nabla p_i = -\frac{1}{m_i} \sum_j \left(V_i^2 + V_j^2 \right) \widetilde{p}_{ij} \frac{\partial W}{\partial r_{ij}} \mathbf{e}_{ij}, \tag{9}$$

where $\mathbf{v}_i^{(p)}$ refers to the velocity induced by pressure forces. Here, the kernel gradient formulation $\nabla W_{ij} = \frac{\partial W}{\partial r_{ij}} \mathbf{e}_{ij}$ with $\mathbf{e}_{ij} = \mathbf{r}_{ij} / \left|\mathbf{r}_{ij}\right|$ and the inter-particle averaged pressure

$$\widetilde{p}_{ij} = \frac{\rho_i p_j + \rho_j p_i}{\rho_i + \rho_j}, \tag{10}$$

are used. This density weighting during the interaction of two particles ensures a continuous acceleration by the pressure gradient even for density discontinuities [37]. While this formulation conserves both linear and angular momentum, it is not zeroth-order consistent. Hence, for a constant pressure field the numerical gradient only vanishes for symmetric particle distributions, which in general are not present.

For the viscous force term discretization, Hu and Adams [17] compute the Laplacian from the gradient of the first order inter-particle average. In addition, an inter-particle averaged shear stress is formulated that incorporates continuity of shear stress and velocity at a phase interface. Combining this inter-particle averaged shear stress with the inter-particle averaged Laplacian, the viscous force term is discretized as

$$\frac{d\mathbf{v}_i^{(\eta)}}{dt} = \frac{\eta_i}{\rho_i}\nabla^2\mathbf{v}_i = \frac{1}{m_i}\sum_j \left(V_i^2 + V_j^2\right)\widetilde{\eta}_{ij}\frac{\mathbf{v}_{ij}}{r_{ij}}\frac{\partial W}{\partial r_{ij}} \tag{11}$$

with the velocity induced by viscous forces, $\mathbf{v}_i^{(\eta)}$ the harmonic mean particle viscosity $\widetilde{\eta}_{ij} = \frac{2\eta_i\eta_j}{\eta_i+\eta_j}$ and the relative particle velocity $\mathbf{v}_{ij} = \mathbf{v}_i - \mathbf{v}_j$. While this formulation of the Laplacian conserves linear momentum it does not conserve angular momentum. An angular momentum conservative formulation can be found in [38].
Discretization of the heat conduction equation follows the same approach as applied to the viscous force. First, the inter-particle averaged heat flux is determined by a continuity constraint at the interface. Substituting the flux in the inter-particle averaged gradient, yields a discretized energy equation via

$$\frac{dh_i}{dt} = \frac{1}{m_i}\sum_j \left(V_i^2 + V_j^2\right)\widetilde{k}_{ij}\frac{T_{ij}}{r_{ij}}\frac{\partial W}{\partial r_{ij}}, \tag{12}$$

where $\widetilde{k}_{ij} = \frac{2k_ik_j}{k_i+k_j}$ is the harmonic inter-particle average of thermal conductivity and T_{ij} the temperature difference, respectively.

In WCSPH, negative inter-particle pressure values can lead to particle clumping and the tensile instability [39]. As a remedy, a constant background-pressure field p_b can be added to the equation of state, Eq. (6), to avoid any negative pressures throughout the simulation [40]. However, as the discretized gradient operator, Eq. (9), is not zeroth-order consistent, this constant pressure field generates a spurious gradient and introduces numerical dissipation. Hence, depending on the choice of the background pressure, the simulation results may differ. To avoid this problem the transport-velocity formulation was introduced in [41] and is employed in this work. Here, particles are advected with a momentum velocity corrected for a constant background pressure gradient

$$\widetilde{\mathbf{v}}(t+\Delta t) = \mathbf{v}(t) + \Delta t\left(\frac{\widetilde{d}\mathbf{v}}{dt} - \frac{1}{\rho}\nabla p_b\right), \tag{13}$$

where $\widetilde{\mathbf{v}}$ is the transport-velocity, t and Δt are current time and time step, $\widetilde{d}\mathbf{v}/dt$ follows from the corrected momentum equation, and p_b is the background pressure. In all simulations we use $p_b = p_0$. The discrepancy of advection and momentum velocity is considered in the momentum equation, Eq. (2), in terms of a momentum convection tensor

$$\frac{\widetilde{d}\mathbf{v}}{dt} = \frac{d\mathbf{v}}{dt} + \frac{1}{\rho}\nabla\cdot\left(\rho\mathbf{v}\left(\widetilde{\mathbf{v}} - \mathbf{v}\right)\right) \tag{14}$$

Finally, the particle position $\mathbf{r}$ is updated by

$$\frac{d\mathbf{r}}{dt} = \widetilde{\mathbf{v}}. \tag{15}$$

With this separation of momentum and background pressure gradient the positive effects of the background pressure on the particle distribution are maintained while the numerical dissipation of momentum is avoided. As the background pressure merely appears as prefactor of the gradient operator a multi-phase application is realized by simply applying the background pressure of the respective phase. This transport-velocity model drives particles towards a homogeneous distribution suppressing tensile instabilities while avoiding numerical dissipation [41], and leads to a significant improvement of robustness when complex multi-phase flows are investigated.

3.2. Continuous-surface-stress model

The surface-tension force term in the momentum equation is discretized by a zeroth-order consistent divergence formulation of the continuous surface-stress tensor. The resulting force term is applied as a volumetric force within a transition region between the considered phases. In general, SPH particles are associated with a phase tag. Thus, interfaces are captured and tracked implicitly. To evaluate surface-tension forces, only the retrieval of geometrical information about the interface is modeled explicitly. To obtain this information a color-function defined by

$$c_i^k = \begin{cases} 1 & \text{if particle } i \text{ does not belong to phase } k \\ 0 & \text{else} \end{cases}$$

is introduced. While it is zero within the bulk phase, it exhibits a unit jump at any phase interface. In turn, the gradient of the color-function approximates a surface-delta function. Applying the SPH gradient formulation from [17] to the color-field yields

$$\nabla c_i^{kl} = \frac{1}{V_i}\sum_j \left(V_i^2 c_i^k + V_j^2 c_j^l\right)\frac{\partial W}{\partial r_{ij}}\mathbf{e}_{ij}, \tag{16}$$

where the superscript kl denotes the interface between phases k and l. By Eq. (16) the surface-delta function is smoothed within a transition band with a width of the kernel cut-off distance. This color-gradient field contains the required geometrical information about the interface, as it approximates the surface normal vector via

$$\mathbf{n}_i^{kl} = \frac{\nabla c_i^{kl}}{\left|\nabla c_i^{kl}\right|}. \tag{17}$$

This simple color-function model is sufficient to incorporate surface-tension effects in SPH.
In [16], Lafaurie et al. show that the divergence of the surface-tensor formulation

$$\Pi = \sigma\left(\mathbf{I} - \mathbf{n} \otimes \mathbf{n}\right)\delta_s \tag{18}$$

exactly reproduces capillary forces. Here, $\mathbf{I}$ is the identity matrix and δ_s denotes the surface-delta function. Substitution of the color-gradient formulation yields

$$\Pi_i^{kl} = \sigma^{kl}\left(\mathbf{I} - \frac{\nabla c_i^{kl}}{\left|\nabla c_i^{kl}\right|} \otimes \frac{\nabla c_i^{kl}}{\left|\nabla c_i^{kl}\right|}\right)\left|\nabla c_i^{kl}\right|. \tag{19}$$

As is evident in Eq. (19), surface-tension is scaled by the color-gradient magnitude and is therefore non-zero only for particles which reside within the phase transition region. As $|\nabla c|$ approaches zero at the fringes of the transition band, an explicit evaluation of the normal vector poses a problem. As a remedy, Wu et al. [42] utilize the small number decay of powers by rewriting Eq. (19) as

$$\Pi_i^{kl} = \sigma^{kl}\frac{1}{\left|\nabla c_i^{kl}\right|}\left(\mathbf{I}\left|\nabla c_i^{kl}\right|^2 - \nabla c_i^{kl} \otimes \nabla c^{kl}\right), \quad k \neq l. \tag{20}$$

Finally, the surface-tension forces are evaluated by a zeroth-order consistent divergence approximation

$$\frac{d\mathbf{v}_i^k}{dt} = \frac{1}{\rho_i}\sum_j V_j\left(\Pi_i^{kl} - \Pi_j^{kl}\right)\frac{\partial W}{r_{ij}}\mathbf{e}_{ij}. \tag{21}$$

The described surface-tension model does not take density variations between phases into consideration. Consequently, a surface-tension force with comparable magnitude applied on both sides of an interface can result in vastly different accelerations and, thus, demand very small time steps for surface-tension dominated flow scenarios with liquid-gas interfaces. As a remedy, in [1] a density-weighted color-gradient is introduced. This allows to shift the applied surface-tension force towards the heavier phase, which ultimately relaxes the time step criterion. This approach is subsequently applied in both CSF and CSS formulations [3,19]. However, as the color-gradient magnitude enters the divergence evaluation in the CSS model, a straight-forward application of the density-weighting is not suitable for CSS models, see Eq. (21). Instead, we apply the density partitioning factor $s = \frac{2\rho_0^k}{\rho_0^k+\rho_0^l}$ to the surface-tension force, where reference densities of the respective interface phases are used for simplicity. The final form of the stress divergence for particle i of phase k at the interface to phase l then follows as

$$\frac{d\mathbf{v}_i^k}{dt} = \frac{2\rho_0^k}{\rho_i\left(\rho_0^k + \rho_0^l\right)}\sum_j V_j\left(\Pi_i^{kl} - \Pi_j^{kl}\right)\frac{\partial W}{\partial r_{ij}}\mathbf{e}_{ij}. \tag{22}$$

This formulation can be interpreted as a partitioning of the surface-tension coefficient, i.e., the heavy phase experiences an increased effective surface-tension coefficient, while the effective surface-tension coefficient of the lighter phase is reduced. While the force distribution is altered, the total force applied at the interface remains unaffected by the partitioning.

3.3. Boundary treatment

In this section, we discuss the proposed color-gradient and boundary condition modifications to incorporate wetting behavior at fluid-fluid-wall triple lines. Incomplete support in the stress divergence Eq. (21) results in a deviation in both magnitude and direction of the surface-tension force at the triple line. Therefore, we propose to include the SPH wall particles in the summations. In turn, appropriate surface-stress tensors and thus color-gradients are required in the wall phase.
This is achieved by associating wall particles at the triple line to either one of the two neighboring fluid phases. Instead of a cumbersome evaluation of the exact location and subsequent extrapolation of the triple line, we approximate the interface in the wall by a wall-normal extrapolation. A nearest neighbor particle flag is introduced, that associates wall phase particles to the nearest neighboring fluid phase. The nearest neighbor fluid phase is found by evaluation of the maximum kernel sum

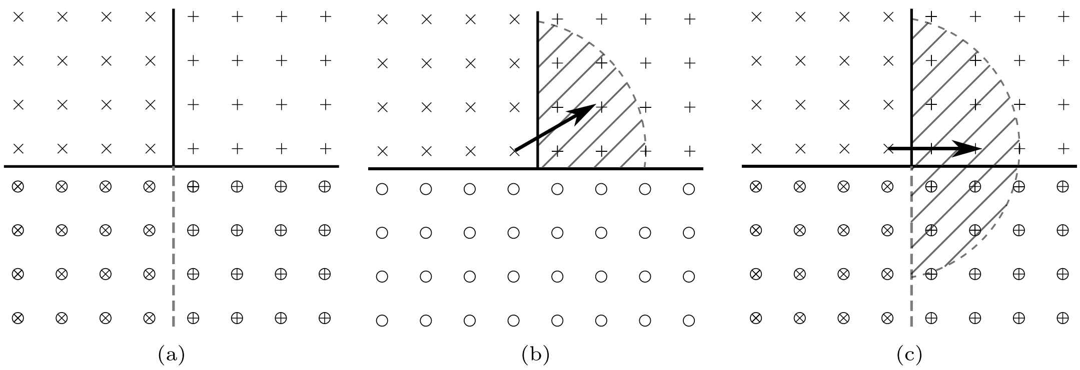

Fig. 1. Normal vector illustration at triple point between fluid $\times$, fluid $+$ and wall $\circ$. (a) Wall particles associated to nearest neighbor fluid phase, (b) poor prediction of $\mathbf{n}$ in fluid due to missing wall particle correction, (c) $\mathbf{n}$ correction in fluid phase by interface extrapolation.

$\max_l \left(\sum_j V_j W_{ij}\right)$ with l fluid phases for each wall dummy particle. In Fig. 1 a) this extrapolation is indicated by marked wall particles. Here cross ($\times$) and plus ($+$) symbols correspond to separate fluid phases while circles ($\circ$) represent a wall phase. Phase interfaces are drawn as bold lines, while dashed lines indicate a fluid interface extrapolation in the wall. The flagged particles are now regarded as fluid particles in the color-gradient, Eq. (16), and surface-stress, Eq. (20), evaluation. Exemplarily, the fluid-fluid color-gradient at the triple line is illustrated prior and post the interface extension in Fig. 1 b) and c). Hatched areas indicate the considered particles in the color-gradient evaluation. As shown, the adjustment leads to a better approximation of both color-gradient direction and magnitude.

In order to determine a surface stress tensor in flagged wall particles, a color-gradient to the non-dominant neighbor fluid phase is evaluated. In this summation all particles of the non-dominant fluid phase, as well as, wall particles flagged as non-dominant fluid phase are considered. Hence, a color-gradient regarding the fluid-fluid interface is associated to each SPH particle in the proximity of the triple line.

Surface wetting is then incorporated according to Young's equation

$$\sigma^{kl}\cos(\theta_w) + \sigma^{lw} - \sigma^{kw} = 0, \tag{23}$$

which induces a surface-tension force at wetting lines to form the equilibrium wetting angle θ_w [8]. Here, index w indicates the fluid wall interface for fluid phases k and l. In order to incorporate this behavior in the CSS model, the direction of the newly formulated color-gradients is transformed to

$$\mathbf{n} = \mathbf{n}_t \sin(\theta_w) + \mathbf{n}_n \cos(\theta_w) \tag{24}$$

with the user defined equilibrium wetting angle θ_w and wall tangential $\mathbf{n}_t$ and wall normal $\mathbf{n}_n$ vector in both fluid and wall phases [8]. Note, while the direction of color-gradients is changed, their magnitude remains the same. In fluid phases an accurate wall normal vector can be evaluated. However, a simple normal-vector formulation using Eq. (16) results in erroneous approximations of the surface normals in wall SPH particles. As each fluid phase is considered individually, erroneous wall normal vectors follow. Hence, instead of a gradient evaluation towards each neighboring fluid phase, a single normal-vector towards all neighboring fluid phases is determined. This normal vector is then associated with the dominant nearest neighbor fluid phase in accord with the wall particles fluid phase flag. The wall tangential vector, $\mathbf{n}_{w,t}$, can then be determined from

$$\mathbf{n}_{w,t} = \frac{\mathbf{n}_{w,nd} - \left(\mathbf{n}_{w,nd}\cdot\mathbf{n}_{w,n}\right)\mathbf{n}_{w,n}}{\left|\mathbf{n}_{w,nd} - \left(\mathbf{n}_{w,nd}\cdot\mathbf{n}_{w,n}\right)\mathbf{n}_{w,n}\right|}, \tag{25}$$

where $\mathbf{n}_{w,nd}$ is the normal vector of wall particles to the non-dominant neighbor fluid phase and $\mathbf{n}_{w,n}$ is the normal vector of wall particles to all neighbor fluid phases. Fig. 2 a) depicts an adjusted wall normal vector and its normal $\mathbf{n}_{w,n}$ and tangential $\mathbf{n}_{w,t}$ contributions. In fluid phases the normal vector $\mathbf{n}_{f,nf}$ to the neighbor fluid phase is used to find the wall tangential vector

$$\mathbf{n}_{f,t} = \frac{\mathbf{n}_{f,nf} - \left(\mathbf{n}_{f,nf}\cdot\mathbf{n}_{f,n}\right)\mathbf{n}_{f,n}}{\left|\mathbf{n}_{f,nf} - \left(\mathbf{n}_{f,nf}\cdot\mathbf{n}_{f,nf}\right)\mathbf{n}_{f,n}\right|}, \tag{26}$$

with $\mathbf{n}_{f,n}$, the normal vector of a fluid phase to the wall phase. In addition, the smoothed normal correction from [23] is applied in fluid particles.

The scenario shown in Fig. 2 a) is a non-equilibrium state. When the newly formulated normal vectors are used together with the color-gradient magnitude in the surface-stress evaluation, Eq. (20), a driving force is introduced at the wetting point acting towards the prescribed wetting angle until steady-state is reached. This steady-state is shown in Fig. 2 b). Note,

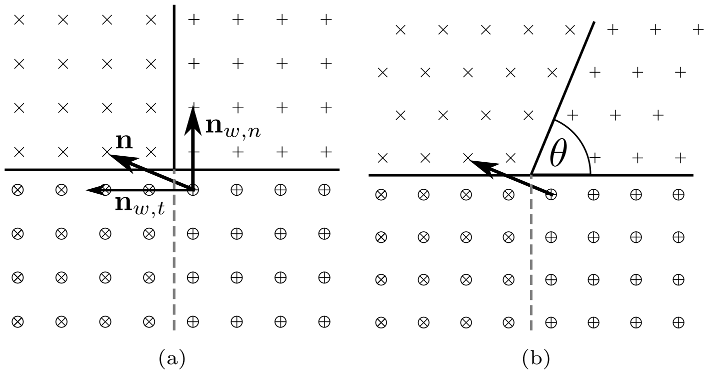

Fig. 2. Normal vector illustration at a triple point between fluid ($\times$), fluid ($+$) and a wall ($\circ$). (a) Prescribed normal vector $\mathbf{n}$ in wall particles at the triple point vs. (b) steady-state with wetting angle θ.

the surface-tension coefficient between fluid phases is also applied in the wall phase surface-stress evaluation. Hence, the model can be understood as an extrapolation of the fluid-fluid interface into the wall. As the wetting model is limited to few particles in proximity of typically few triple lines, the overhead of the additional compute efforts is marginal.

3.4. Time stepping

To ensure numerical stability throughout the simulation, a number of time-step criteria impose a limit on the maximum feasible time step in the employed explicit velocity verlet time integration scheme. Within the presented algorithm, the following time step restrictions are considered. The Courant-Friedrichs-Lewy (CFL) condition

$$\Delta t \leq 0.25 \frac{h}{|\mathbf{v}_{max}| + |\mathbf{c}_{max}|} \tag{27}$$

as function of the maximum flow velocity $|\mathbf{v}_{max}|$ and maximum artificial speed-of-sound $|\mathbf{c}_{max}|$ accounts for sound waves and flow propagation. In addition to the CFL condition, time step criteria regarding particle acceleration by body forces [43],

$$\Delta t \leq 0.25 \left(\frac{h}{|\mathbf{a}|} \right)^{1/2}, \tag{28}$$

viscous diffusion [40]

$$\Delta t \leq 0.125 \frac{h^2 \rho_0}{\eta_0}, \tag{29}$$

and thermal diffusion [44]

$$\Delta t \leq 0.125 \frac{c_p h^2 \rho_0}{k} \tag{30}$$

are considered. Finally, to maintain numerical stability when surface-tension forces are involved, an additional time step condition is required. Brackbill et al. [8] introduce a condition based on two capillary waves approaching each other. With a maximum velocity, found for the minimal resolvable wavelength of $2\,\Delta x$, the restriction of the time step follows from

$$\Delta t \leq \left(\frac{\frac{1}{2}\left(\rho^k + \rho^l\right) h^3}{2\pi \sigma^{kl}} \right)^{1/2}, \tag{31}$$

where the averaged density at a phase interface is used. However, a direct application to the CSS model in SPH is not possible as accelerations and thus velocities can exceed stable conditions in the lighter fluid phase of the interface. Hence, it is adjusted in literature [17] to consider the minimum interface density as

$$\Delta t \leq 0.25 \min \left(\frac{\min\left(\rho^k, \rho^l\right) h^3}{2\pi \sigma^{kl}} \right)^{1/2}. \tag{32}$$

The criterion can become restrictive in surface-tension dominated problems as usage of the lighter fluid density leads to small time steps. However, the proposed force partitioning scheme reduces the applied force on the lighter interface particles. The force partitioning can be understood as partitioning of the surface tension coefficient. Now, when the partitioning factor s is applied to σ in Eq. (32), we again achieve the arithmetic mean of both interface densities in the time step condition

$$\Delta t \leq 0.25 \min \left(\frac{\left(\rho^k + \rho^l\right) h^3}{4\pi \sigma^{kl}} \right)^{1/2}, \tag{33}$$

allowing for significant time-step constraint relaxation at high density ratios in the CSS model for SPH simulations.
In WCSPH, an artificial speed-of-sound instead of the physical speed-of-sound is used to increase the time step size [40]. In this work, the estimates introduced in [40,43,44] are applied to restrict density fluctuations to one percent of the reference density. For considering surface-tension forces, the speed-of-sound condition

$$c^2 \geq \max \left(\frac{\sigma^{kl}}{\min\left(\rho^k, \rho^l\right) l_{ref}\ \delta} \right) \tag{34}$$

with reference length l_{ref} and compressibility δ is added [17]. Again, the condition is relaxed to

$$c^2 \geq \max \left(\frac{2\sigma^{kl}}{\left(\rho^k + \rho^l\right) l_{ref}\, \delta} \right) \tag{35}$$

by applying the partitioning factor. Note, with this adjustment the identical numerical speed-of-sound is used in both fluid phases for scenarios when the surface-tension condition is dominant.

4. Model validation

In this section, the functionality of the proposed surface-tension model is evaluated by several test cases. First, the influence of the force partitioning on static and dynamic interface behavior is shown for a square droplet deformation and capillary waves. Overall, a good agreement with the analytical solution is found. While the force partitioning introduces a slight error for large density ratios as compared to the original model, it is shown to decline with increasing particle resolution. Next, the effect of force partitioning on static and dynamic thermo-capillary forces is analyzed by the droplet rise test case. Here, we find the model to accurately reproduce droplet rise velocities for different density ratios for high resolutions, while at low resolutions the analytical target velocity is significantly underestimated. Finally, the wall boundary model is evaluated by static droplet wall wetting for several wetting angles and Eötvös numbers. Good agreement is found for a wide range of contact angles. At extremely hydrophobic and hydrophilic conditions, the contact angles are under- and overestimated by the wall model as shown for other aproaches [23,24]. Unless otherwise stated, in all simulations the relaxed artificial speed-of-sound and time step criteria are applied. Note, this implies drastically increased time steps by a factor of up to $\sqrt{(\rho_k + \rho_l)/2\rho_k} \approx 22$ for an water-air interface. The kernel smoothing length is fixed to $h/\Delta x = 1$ with particle spacing Δx. All specifications are given in SI units. The test cases are characterized by the set of non-dimensional numbers listed in Table 1.

4.1. Laplace law

The first surface-tension dominated flow case considered is the deformation of a squared fluid volume into a circular droplet [1,19]. Here, fluid 1 is forming a square box with side length $l = 0.6m$ centered in a bulk fluid box of size $L = 1.0m$. The domain is confined by dummy particles enforcing no-slip and no-penetration boundary conditions. Due to surface-tension forces the initial setup is deformed towards a droplet at steady-state as shown in Fig. 3. In the following, the influence of the introduced force partitioning is investigated for different density ratios and Reynolds numbers. For all test cases the flow is characterized by a capillary number and Reynolds number based on the heavy fluid material properties. At steady-state a pressure discontinuity at the droplet interface is forming. The Young-Laplace law in two dimensions yields a pressure increase of

$$\Delta p = \frac{\sigma}{R} = \frac{\sigma\sqrt{\pi}}{l} \tag{36}$$

in the droplet, which solely depends on the effective droplet radius R and surface-tension coefficient σ. As this pressure is induced by capillary forces only, it is used as measure to evaluate the model quality. First, the influence of density ratios and thus surface-tension force scaling factors is examined. The flow is characterized by a Reynolds number of $Re = 3$ and capillary number of $Ca = 0.2$, where the reference velocity is chosen to be $1m/s$ and reference length is l. All simulations are run at a resolution of $\Delta x = 0.01m$. All pressure profiles displayed in Fig. 4 are smoothed using the Shepard weighting $p_i^k = \sum_j V_j^k p_j^k W_{ij} / \sum_j V_j^k W_{ij}$, where the superscript k indicates the respective phase. In Fig. 4 a) pressure profiles are plotted over the radial coordinate for density ratios of $\Theta_\rho = 10$ and $\Theta_\rho = 1000$, which in turn correspond to scaling factors of $s = 20/11$ and $s = 2000/1001$ on the droplet phase. A viscosity ratio comparable to a water air interface of $\Theta_\eta = 100$ is

Table 1
Characteristic non-dimensional numbers for test cases in section 4.

Non-dimensional numbers	
Reynolds	$Re = \frac{\rho v_{ref} l_{ref}}{\eta}$
Capillary	$Ca = \frac{\eta v_{ref}}{\sigma}$
Marangoni	$Ma = \frac{\sigma \lvert \nabla T \rvert l_{ref}}{\eta}$
Laplace	$La = \frac{\sigma \rho l_{ref}}{\eta}^2$
Eötvös	$E\ddot{o} = \frac{\rho g l_{ref}^2}{\sigma}$

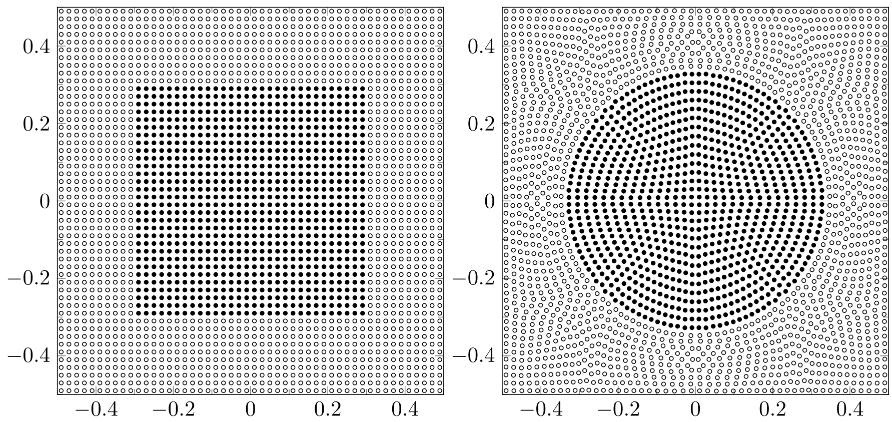

Fig. 3. Initial (left) and steady-state (right) particle distribution of the square to droplet deformation test case.

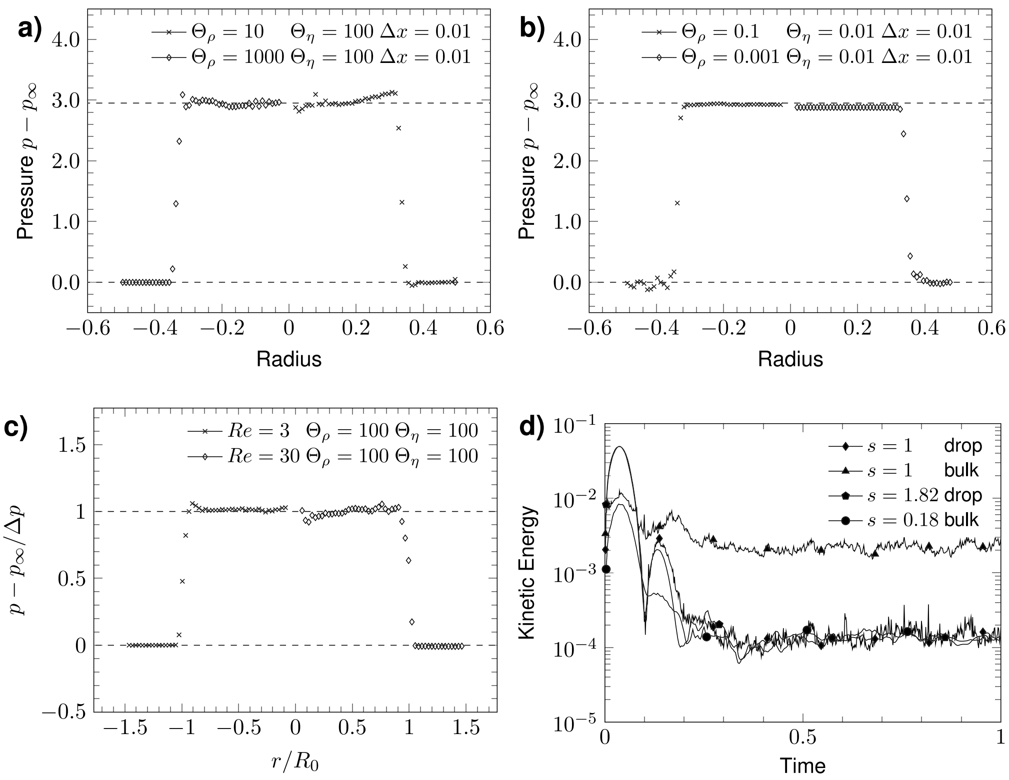

Fig. 4. Square to droplet deformation steady-state pressure distribution along horizontal center line for droplet-bulk density ratios a) $\Theta_\rho = 10$ and $\Theta_\rho = 1000$, b) $\Theta_\rho = 0.1$ and $\Theta_\rho = 0.001$, c) Reynolds numbers $Re = 3$ and $Re = 30$ for $\Theta_\rho = 100$ and d) kinetic energy over time for drop and bulk phase with density scaling factors of $s = 1$, $s = 1.82$ and $s = 0.18$ for $\Theta_\rho = 10$.

chosen. Dashed lines indicate the analytical solution of the Young-Laplace law. The steady-state pressure jump is in good agreement with the analytical solution for both investigated density ratios. The results do not indicate a significant influence of the partitioning factor on the pressure field. Next, heavy and light fluid phases are switched to mimic a bubble within a heavier bulk phase. The resulting pressure profiles shown in Fig. 4 b) again match the Young-Laplace pressure jump very well. However, compared to the droplet case, the pressure difference is slightly reduced. As indicated by Adami et al. [1], a density-based scaling of surface-tension forces shifts the effective interface towards the heavy phase and, thus, slightly changes the effective radius of the droplet. This also becomes apparent by comparison of the pressure profiles with density ratios of $\Theta_\rho = 0.1$ and $\Theta_\rho = 0.001$ directly. However, this effect decreases with resolution. In order to test the sensitivity of the density partitioning on the viscosity two cases characterized by $Re = 3$ and $Re = 30$ with $Ca = 0.2$, $\Theta_\rho = 100$ and $\Theta_\eta = 100$ are compared next. In Fig. 4 c), the pressure profiles show a slightly less accurate approximation of the pressure jump with the Reynolds number increase. This negative effect of a Reynolds number increase to the pressure approximation is attributed to parasitic currents at the interface [19]. These currents can be expressed by high kinetic energies in the flow field at steady-state. Hence, a comparison of the kinetic energy evolution over time shows the impact of the model on these spurious currents. In Fig. 4 d), the kinetic energy for $Re = 3$, $\Theta_\rho = 10$, $\Theta_\eta = 100$ is depicted both with and without the density scaling enabled. Initially, high kinetic energy is expected as the square shape deforms into a droplet. Once the droplet is formed, low kinetic energy can be interpreted to correspond to low parasitic currents. Density scaling shows to decrease the kinetic energy in the lighter phase by more than an order of magnitude while, no increase in the heavy phase is found. This indicates a reduction of spurious currents within the system. Hence, stability of the droplet is enhanced by the partitioning. Additionally, the scaled speed-of-sound is increased in the droplet by 34.9% and decreased in the bulk by 57.4%, while the time step is increased by 133%.

4.2. Droplet oscillation

In a second test case we investigate the dynamic response of capillary forces on an initial velocity field [1,13,17]. The domain is set up with a droplet of radius $R = 0.2$ at its center, surrounded by a second fluid within a square box of size $L = 1.0m$. At the boundaries no slip and no penetration conditions are enforced. Within the droplet a velocity field with x and y components of

$$U_x = U_0 \frac{x}{r_0}\left(1 - \frac{y^2}{r_0 r}\right)\exp\left(-\frac{r}{r_0}\right) \tag{37}$$

$$U_y = -U_0 \frac{y}{r_0}\left(1 - \frac{x^2}{r_0 r}\right)\exp\left(-\frac{r}{r_0}\right) \tag{38}$$

is initialized, where $U_0 = 10m/s$ and $r_0 = 0.05m$. First, a flow field characterized by $Ca = 0.18$ and $Re = 28.8$ is investigated. Here $L_{ref} = 2R$ and $U_{ref} = 3.6m/s$ are chosen as reference length and reference velocity. The density ratio is set to $\Theta_\rho = 2$ between droplet and bulk phase. In turn, a force partition of 1.33 : 0.67 is applied. The surface-tension coefficient is chosen to be $\sigma = 2N/m$. In Fig. 5, particle snapshots at time steps 0.0, 0.8, 0.16, and 0.26 show the droplet movement. Convergence is shown by a resolution study for the x and y position of the center of mass evolution of the upper right droplet quarter in Fig. 6 a). Note, that the number of particles within the cut-off radius is kept constant while the initial particle spacing is decreased for the sake of simplicity.

In order to determine the influence of the force partitioning, the same test case is set up with a force partitioning factor of $s = 1$, while the density ratio is maintained at $\Theta_\rho = 2$. In Fig. 6 b), a discrepancy between the mass center position due to force partitioning is shown for a resolution of $\Delta x = 1/120m$. With increasing resolution of $\Delta x = 1/30m$, over $\Delta x = 1/60m$, to $\Delta x = 1/120m$ the relative difference between the oscillation period decreases from 3.8%, over 1.9% to 1.6%. This discrepancy is attributed to the difference in effective drop radius, which results from the capillary-force partitioning. In a next test case the influence of a varying capillary number on small scale oscillations is investigated. Here, the material properties are changed to correspond to a density ratio of $\Theta_\rho = 1000$ and viscosity ratio of $\Theta_\eta = 100$. These settings resemble a physical water/air phase interface. The initial flow field velocity magnitude is set to $U_0 = 1.0m/s$. The flow field is characterized by $Re = 2.88$ and capillary numbers between $Ca = 0.0128$ and $Ca = 0.03$. The measured oscillation periods displayed in Fig. 7 are in good agreement with the analytical solution $\tau = 2\pi\sqrt{R^3\rho/6\sigma}$.

4.3. Static Marangoni force

We test the capability of the proposed CSS model to accurately evaluate Marangoni forces through Eq. (22). Therefore, a square domain of side length $L = 5.76e^{-3}m$ is filled with two fluids separated by a vertical interface at the domain center [13]. Particle-disorder effects are eliminated here, by looking at a fixed particle calculation. Marangoni forces are induced by initializing a linear temperature profile in vertical direction. With a temperature gradient of $\nabla T = 200K$ and a surface-tension coefficient dependence on temperature of $d\sigma/dT = -0.002N/K\ m$, a Marangoni force of $0.4N$ is expected to be applied along the interface. First, the force partitioning is disabled. Samples of the predicted volumetric force magnitude along the horizontal domain center are shown in Fig. 8 a) for different resolutions. With increase in resolution, the interface width decreases while the volumetric force magnitude increases. Integration along one horizontal line of particles yields the

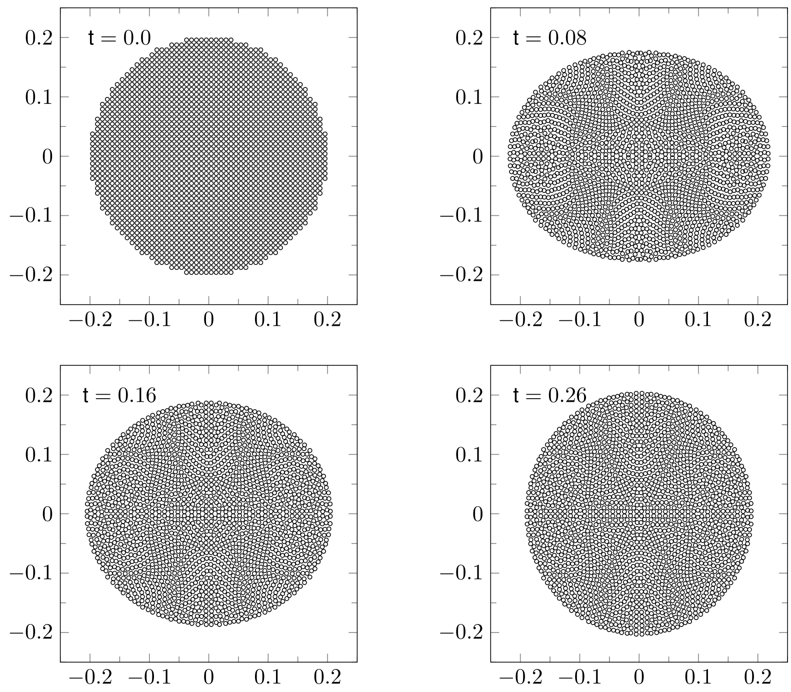

Fig. 5. Capillary wave with $\Theta_\rho = 2$, particle snapshots of droplet at time $t = 0.0, 0.08, 0.16$, and 0.26.

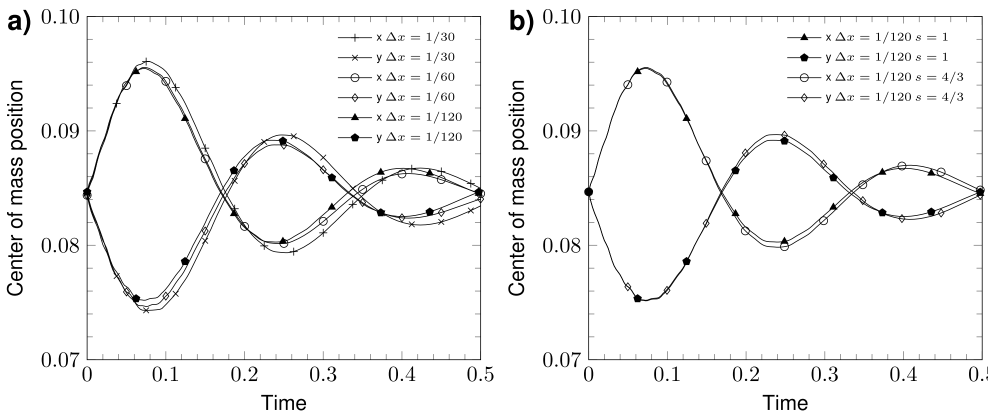

Fig. 6. Capillary wave center of mass evolution of the upper right droplet quarter over time with a) $\Theta_\rho = 2$ at resolutions $\Delta x = 1/30m$, $\Delta x = 1/60m$, $\Delta x = 1/120m$ and b) $\Theta_\rho = 2$ and $\Theta_\rho = 1$ at resolution $\Delta x = 1/120m$.

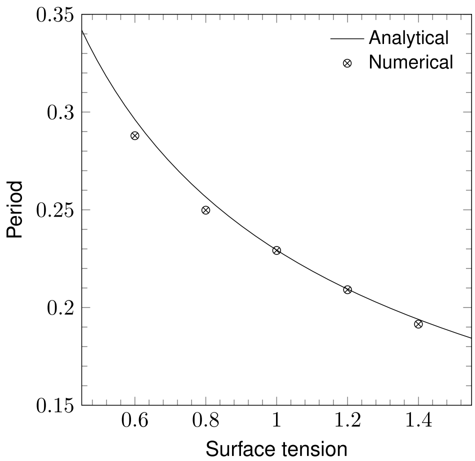

Fig. 7. Capillary wave with $\Theta_\rho = 1000$ and $\Theta_\eta = 100$ comparison of numerical oscillation period to analytical value $\tau = 2\pi\sqrt{R^3\rho/6\sigma}$.

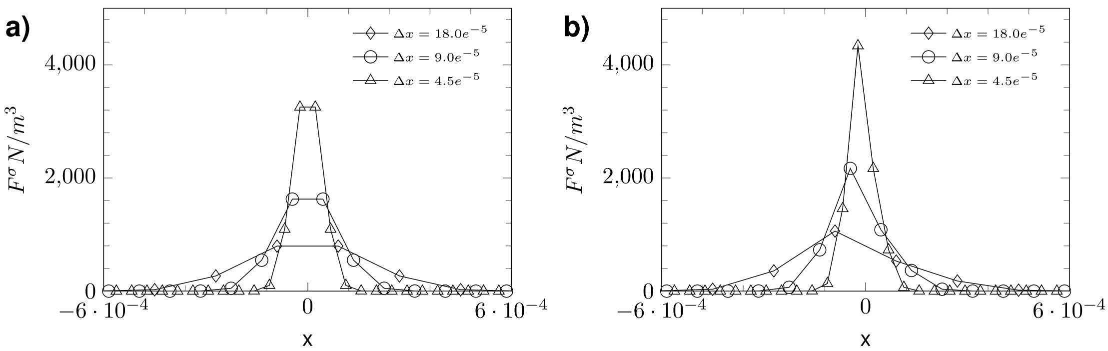

Fig. 8. Static Marangoni force per volume plotted perpendicular to interface for $\Theta_\rho = 2$ a) $s = 1$ and b) $s = 4/3$ and $s = 2/3$ on heavy and light phase.

predicted Marangoni force applied per interface segment Δx. With a predicted force magnitude of $0.400569N$ a constant relative error of 0.14% is achieved for all resolutions. No change is expected as in this test case a resolution change has no influence on the evaluation of Eq. (21). This simple example confirms the capability of the described model to accurately evaluate Marangoni forces. Now, the density of the left fluid is increased and the force partitioning is enabled. Thus, Marangoni force on the heavy fluid is increased while it is decreased on the lighter fluid. In Fig. 8 b), the force partitioning effect is demonstrated. Here, the partition factor is $s = 4/3$ and $s = 2/3$ for the heavy and light fluid respectively. The redistribution of the Marangoni force maintains the total force applied, overall, no changes in the relative error are observed.

4.4. Thermo-capillary rise

Now, the partitioning CSS-model is applied to the thermocapillary rise problem [28,45–47]. A rectangular domain of height $7.5D$ and width $5D$ is filled with a bulk fluid. A droplet of diameter D is placed on the vertical center line at a distance of $1.5D$ from the bottom wall. Top and bottom walls enforce Dirichlet temperature and no slip velocity boundary conditions while, adiabatic slip boundary conditions are applied at the side-walls. A constant linear temperature in vertical direction is enforced in all phases. The thermal surface-tension dependence is given by

$$\sigma = \sigma_0 + \frac{d\sigma}{dT}(T - T_0)\,. \tag{39}$$

Consequently, unevenly distributed capillary forces and a tangential surface-tension gradient induce a resulting droplet motion. In Fig. 9 a), a representative droplet is depicted with the particle distribution. The particles and velocity vectors are colored by temperature and velocity magnitude, respectively.

A theoretical relation for the steady rise velocity of the droplet is derived by Young et al. [48] as

$$u_{YBG} = \frac{\sigma_T |\nabla T| D}{9\eta_d + 6\eta_b} \tag{40}$$

with $\sigma_T = d\sigma/dT$, and bulk and droplet viscosities η_b and η_d.

We first study a case characterized by $\rho_b = \rho_d = 0.2kg/m^3$, $\eta_b = \eta_d = 0.1Pa\,s$ and $D = 1.0m$. A temperature of $T_0 = 0.0K$ and $T_1 = 1.0K$ is prescribed at the bottom and top wall, resulting in a temperature gradient of $\nabla T = 1/7.5K/m$. Heat capacity and thermal conductivity of the bulk and droplet phase are set to $c_p = 1J/kg\,K$ and $k = 0.1W/m\,K$, respectively. With a theoretical steady rise velocity of $u_{YBG} = 0.088m/s$, the case is defined by $Re = 0.888$, $Ca = 8.8e^{-3}$ and Marangoni number $Ma = 0.178$. The reference length $l_{ref} = 3D/32$ is chosen for speed-of-sound and time step criteria. The net droplet rise velocity is extracted from the integrated momentum via

$$u_{rise} = \frac{\sum_i m_i v_{y,i}}{\sum_i m_i}. \tag{41}$$

From a resolution study we find the deviation of the steady rise velocity to the analytical solution to decrease from 2.49%, over 1.99% to 1.19% for resolutions of $D/\Delta x = 16$, $D/\Delta x = 32$ and $D/\Delta x = 64$, respectively. Exemplary, the non-dimensional rise velocity is shown in Fig. 9 b) for a simulation with resolution of $D/\Delta x = 64$. After an initial transient phase, the rise velocity fluctuates around the analytical rise velocity slightly under predicting it. These results agree well with literature [28,45–47].

Next, the influence of the density partitioning on the rise velocity is studied. In order to isolate the effect of adapting the effective droplet radius towards the heavier phase we first apply a force partitioning corresponding to a density ratio of $\Theta_\rho = 10$ between droplet and bulk phase. The density in both phases, however, is set identical. Thus, besides speed-of-sound also the correction pressure in the transport velocity scheme are equivalent in both phases. The droplet rise velocity is shown for different resolutions in Fig. 10 a). When surface-tension forces are partitioned, the steady rise velocity deviates

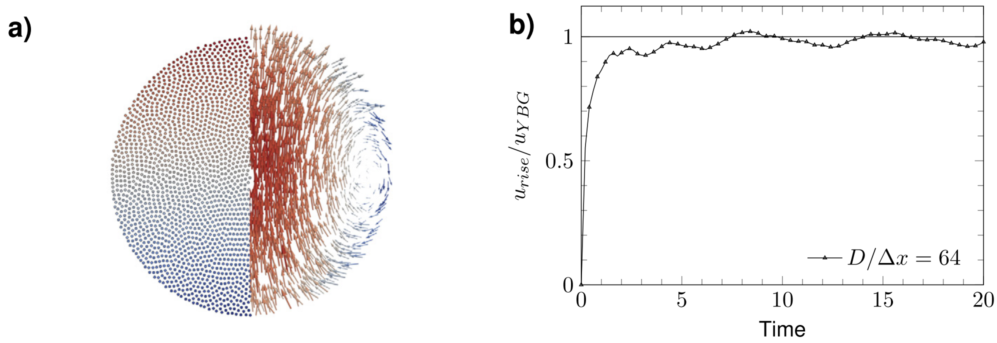

Fig. 9. Thermo-capillary induced droplet rise, a) color-coded temperature (left) and velocity vectors (right), b) average normalized droplet rise velocity over time for resolution $D/\Delta x = 64$. (For interpretation of the colors in the figure(s), the reader is referred to the web version of this article.)

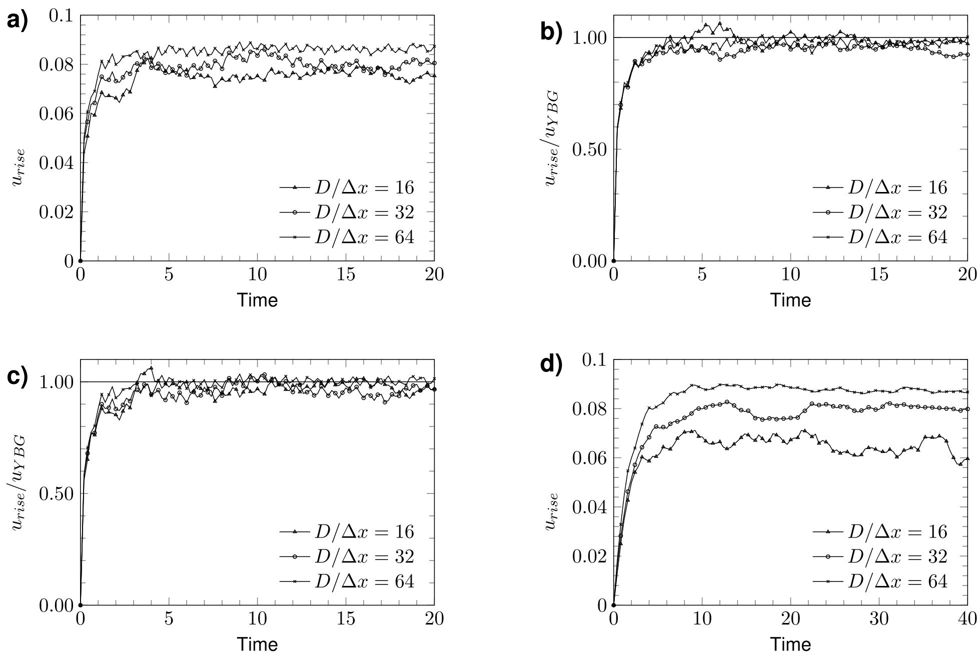

Fig. 10. Thermo-Capillary rise velocity for resolutions $D/dx = 16$, $D/dx = 32$ and $D/dx = 64$ at same densities in droplet and bulk phase a) enforcing force partitioning of $10:1$, b) normalized rise velocity by analytical target velocity without force partitioning, c) normalized rise velocity by analytical target velocity with adjusted radius enforcing force partitioning of $10:1$, and d) rise velocity at density ratio $\Theta_\rho = 10$ between droplet and bulk phase with applied force partitioning.

from the analytical solution in accordance with particle resolution. We attribute this change in the rise velocity to the effective radius 'seen' by the surface-tension forces. By approximating the radius shift as Δx the corresponding analytical rise velocities are found as $u_{YBG} = \sigma_T |\nabla T| (D - \Delta x) / (9\eta_d + 6\eta_b)$. In Fig. 10 b) and c) the rise velocities normalized by their respective corrected analytical rise velocity are plotted over time for both the non-partitioned and partitioned cases. As the results are in good agreement, we conclude that the force partitioning can be applied to both capillary and Marangoni forces. Now, the droplet density is changed to $\rho_d = 2kg/m^3$. For this case, we decrease the reference length to minimize density variations. As the acceleration phase of the now heavier droplet is extended, the total physical simulation time is doubled. In Fig. 10 d), the average rise velocity for resolutions $D/\Delta x = 16$, $D/\Delta x = 32$ and $D/\Delta x = 64$ are plotted over time. The rise velocity increases with resolution approaching the analytical target velocity of $u_{YBG} = 0.088m/s$ again, as expected, with increasing resolution.

4.5. Droplet wetting

In this last example, we show the functionality of the proposed wall contact model. Here, we study the wetting behavior of droplets on a solid wall [22–24]. An initially square box of size $l = 0.025m$ filled with fluid 1 is placed onto a wall in a domain of width $w = 0.1m$ and height $h = 0.05m$. All walls are modeled with no slip and no penetration boundary conditions. Due to surface-tension forces, fluid 1 is expected to wet the wall forming a circular segment with a static contact angle θ_w. At first, we compare the spurious currents at the wetting line observed with the new approach and an earlier formulation [17], where wetting conditions are incorporated by means of wall surface-stress components scaled according

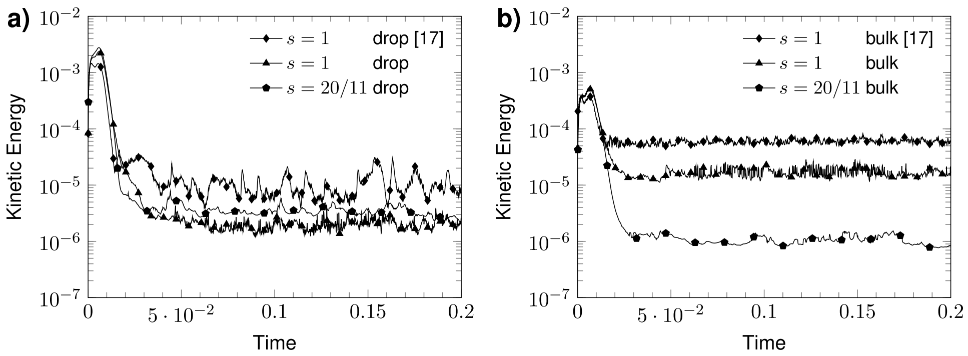

Fig. 11. Droplet wetting at wetting angle $\theta_w = 60°$, $\Theta_\rho = 10$ and $\Theta_\eta = 10$, kinetic energy of a) droplet and b) bulk over time for reference model [17], current model without and with density partitioning.

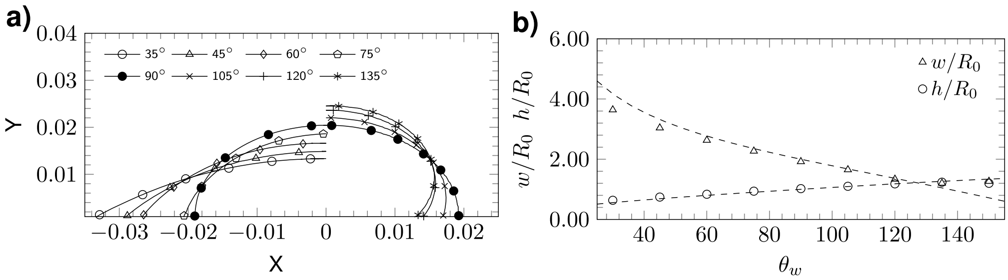

Fig. 12. a) Droplet wetting contours and b) droplet width w/R_0 and height h/R_0 plotted for several wetting angles θ_w, analytical solution as dashed lines.

to the Young Laplace wetting theory. The test case is characterized by a Laplace number of $La = \frac{\sigma \rho l_{ref}}{\eta^2} = 20$, density ratio of $\Theta_\rho = 10$ and viscosity ratio of $\Theta_\eta = 10$ between the droplet and the bulk phase. Reference length and velocity are chosen as $l_{ref} = 0.02m$ and $v_{ref} = 1.0m/s$. The domain is discretized with $l/\Delta x = 40$ particles. In Fig. 11 a), the kinetic energy evolution within the liquid drop for a wetting angle of $\theta_w = 60°$ is shown for the reference model [17] and the model proposed in this work, both with and without force partitioning. The overall level of kinetic energy is of the same order of magnitude for all setups, yet with the present wall model it fluctuates less. Note, that even when the applied force on the droplet is increased by the force partitioning, no significant increase in kinetic energy is found. Examining the kinetic energy within the lighter bulk phase, see Fig. 11 b), a strong decrease is found for the partitioned model.

To further examine the proposed wall contact model, the droplet wetting behavior on solid walls for different prescribed contact angles is studied. Here, the flow is characterized by a Laplace number of $La = 20$, density ratio of $\Theta_\rho = 1000$ and viscosity ratio of $\Theta_\eta = 100$ between the droplet and the bulk phase. The domain is again discretized with $l/\Delta x = 40$ particles. The steady-state droplet height h_{ana} and wall contact width w_{ana} can be determined from

$$R_{ana} = R_0 \sqrt{\frac{\pi}{2\left(\theta_w - \sin(\theta_w)\cos(\theta_w)\right)}}, \tag{42}$$

$$h_{ana} = R_{ana}\left(1 - \cos(\theta_w)\right), \tag{43}$$

$$w_{ana} = 2\, R_{ana} \sin(\theta_w), \tag{44}$$

where R_{ana} and R_0 are the analytical and reference radius, respectively [24]. Fig. 12 a) shows a collection of droplets ranging from wetting angles of $\theta_w = 60°$ up to $\theta_w = 120°$. The shown interfaces agree well with the expected droplet shape for both wetting and non-wetting constellations. A comparison of the wetting length and droplet height with the analytical solution as shown in Fig. 12 b) indicates good agreement for a wide range of wetting and non-wetting angles. Similar behavior is reported in literature [23,24] for other approaches.

Now, the droplet wetting case is extended to include gravity to examine the interplay of surface-tension and body forces. Their balance is expressed by the Eötvös number $\text{Eö} = \frac{\rho g l_{ref}^2}{\sigma}$. With increasing Eö, the spherical droplet segment flattens. For gravity-dominated cases (Eö >> 1), the segment height is given by

$$h = 2\sqrt{\frac{\sigma}{\rho g}} \sin\left(\theta_w/2\right) \tag{45}$$

with the droplet density ρ and gravity g [24]. In the following, both a wetting $\theta_w = 60°$ and non-wetting $\theta_w = 120°$ case are investigated for Eötvös numbers between 0.01 and 50. The ratios of density and viscosity are set to $\Theta_\rho = 1000$ and

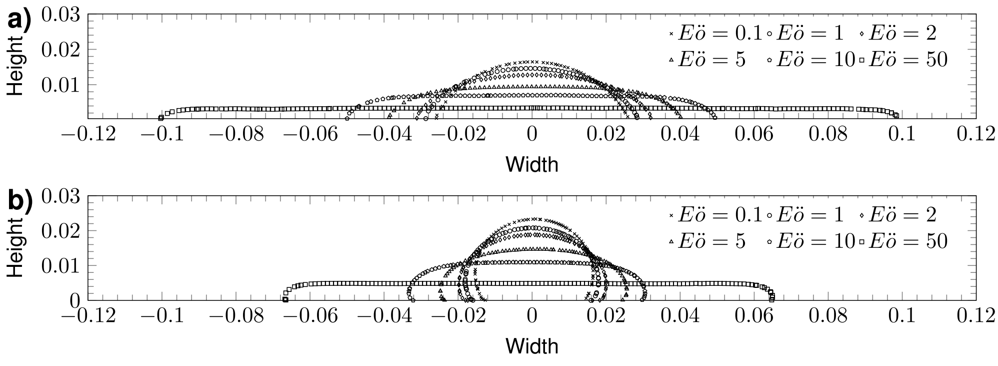

Fig. 13. Droplet wetting contours at different Eötvös numbers for wetting angle a) $\theta_w = 60°$ and b) $\theta_w = 120°$.

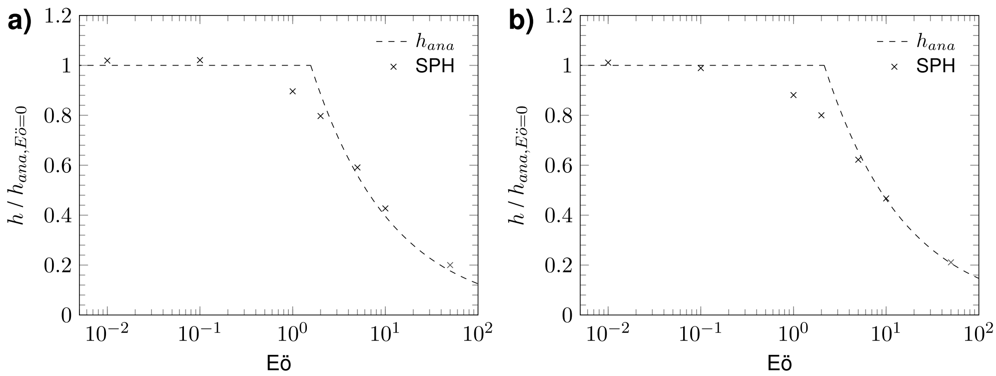

Fig. 14. Droplet wetting height measurement at different Eötvös numbers for wetting angle a) $\theta_w = 60°$ and b) $\theta_w = 120°$.

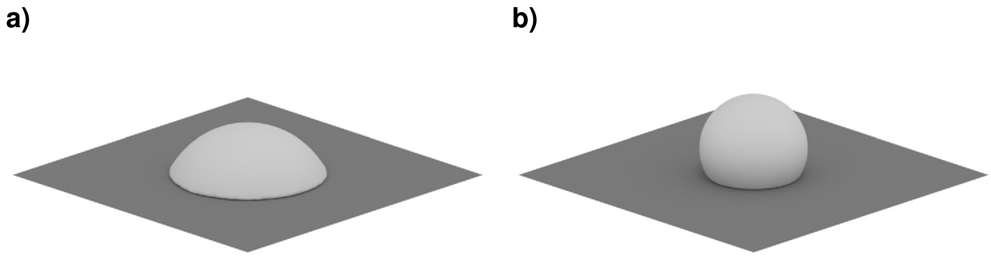

Fig. 15. Three dimensional droplet shape for a wetting a) $\theta_w = 60°$ and b) non-wetting $\theta_w = 120°$ bottom wall.

$\Theta_\eta = 100$. For the strongly flattened cases we use a large domain size of $w = 0.3m$ to reduce boundary effects. The resolution is maintained at $l/\Delta x = 40$ for the Eö$= 0.1$ to Eö$= 10$ cases and increased to $l/\Delta x = 80$ for the Eö$= 50$ case. Fig. 13 shows the droplet interfaces for wetting a) and non-wetting b) droplets of different Eötvös numbers. The corresponding estimates for the width and height agree well with the analytical approximation, see Fig. 14.

Finally, we demonstrate the applicability of the model to heterogeneous wetting scenarios in three dimensions [49–52]. Initially, a liquid cuboid of side length $l = 0.025m$ is placed at the center of the bottom wall of a box with dimensions $(0.1m, 0.1m, 0.05m)$. The remainder of the box is filled with gas. At all walls no slip boundary conditions are applied. Again, the case is characterized by a Laplace number of $La = 20$, density ratio of $\Theta_\rho = 1000$ and viscosity ratio of $\Theta_\eta = 100$. The domain is discretized by $l/\Delta x = 40$ particles.

To validate the wetting model in three dimensions, the scenarios of homogeneous wetting, $\theta_w = 60°$, and non-wetting, $\theta_w = 120°$, conditions are studied first. Steady state droplet shapes for a wetting, Fig. 15 a), and non-wetting, Fig. 15 b), bottom wall are in good agreement with the obtained two dimensional results. Thus we conclude, a general applicability of the proposed models to three dimensional scenarios.

Now, the wetting properties of the bottom wall are changed to include both wetting and non-wetting sections. Two orthogonal stripes of width $d = 0.01m$ are placed on the x and y central axis. These stripes are characterized by different static wetting angles compared to the remainder of the bottom wall. In Fig. 16 a) the steady-state droplet shape is shown for stripes with a wetting angle of $\theta_s = 60°$ and a bottom-wall wetting angle of $\theta_w = 120°$. Due to these wetting properties a square-like droplet forms which extends along the stripes and contracts on the remaining surface. When the inverse wetting setup is considered, the droplet deforms towards the four hydrophilic sections while it retracts on the stripe-surfaces, see Fig. 16 b). The steady state wetting line contours for both cases are plotted in Fig. 16 c) and d). These results are in

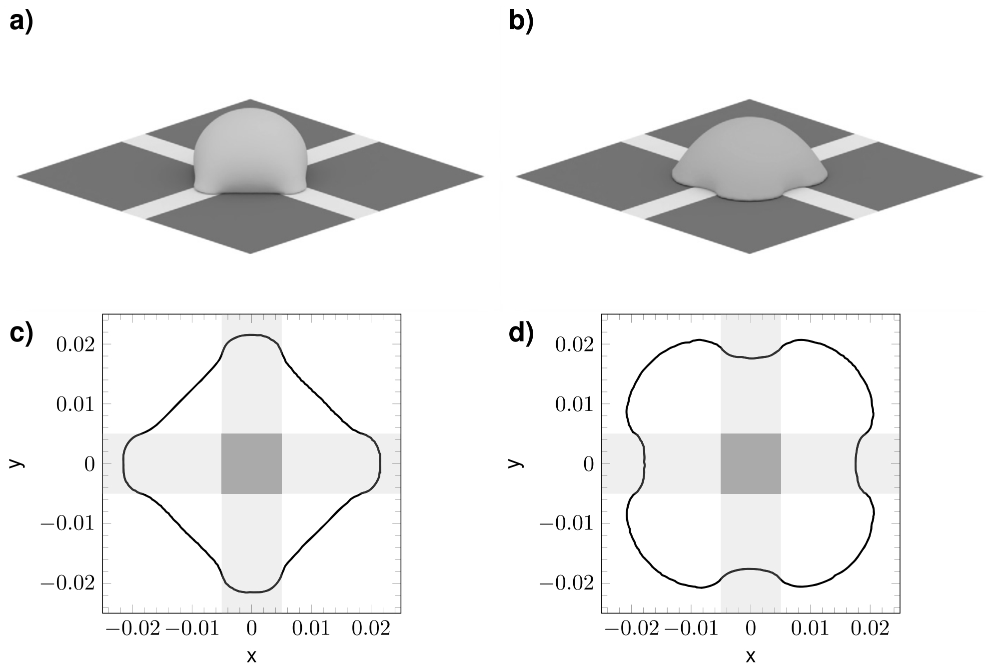

Fig. 16. Droplet shape for a) wetting and b) non-wetting stripes and wetting line at steady state for c) wetting and d) non-wetting stripes.

good qualitative agreement with reference literature [49–52] and demonstrate the functionality of the proposed method for general three-dimensional problems.

5. Conclusion

A density partitioned continuous surface-stress (CSS) model is proposed in this work. The weighting of the CSF approach in Adami et al. [1] is applied to the divergence of the total surface stress to yield comparable accelerations from surface tension in both phases at the interface. As a result, the artificial speed-of-sound and time step criteria based on surface-tension are relaxed for density ratios larger than one. In addition, a static contact-angle wetting model is incorporated at the contact line. Here, color-gradients are adjusted for a better representation of the interface normal vectors. Wetting behavior is incorporated by prescribing normal vectors in wall boundary particles and fluid particles at the triple line.

In all investigated flow cases the partitioned CSS model facilitates numerically stable solutions at high density and viscosity ratios. It is demonstrated that the minor relocation of effective capillary forces causes only a small change in static and dynamic response of the system. Such small deviations can be attributed to a minor relocation of effective curvature and are shown to diminish with resolution. The kinetic energy of spurious currents present at a phase interface are reduced by up to an order of magnitude in the lighter phase, while their level is maintained in the heavy phase. Investigation of the thermo-capillary droplet rise and, thus, partitioning of both capillary and Marangoni forces shows accurate results for high particle resolutions. Again, an underestimation of the terminal rise velocity for low resolutions is attributed to an effective shift in the droplet radius. The study of droplet wall wetting reveals good agreement with the analytical solution for a wide range of wetting angles. The kinetic energy in the system at steady-state is reduced by an order of magnitude as compared to the previous treatment [17]. For all presented cases, the numerical time step is highly increased with respect to previous criteria while maintaining numerical stability.

CRediT authorship contribution statement

C. Zöller: Conceptualization, Data curation, Formal analysis, Investigation, Methodology, Software, Validation, Visualization, Writing – original draft, Writing – review & editing. **N.A. Adams:** Funding acquisition, Project administration, Resources, Writing – review & editing. **S. Adami:** Conceptualization, Formal analysis, Investigation, Methodology, Software, Supervision, Writing – review & editing.

Declaration of competing interest

The authors declare that they have no known competing financial interests or personal relationships that could have appeared to influence the work reported in this paper.

Data availability

Data will be made available on request.

Acknowledgements

Christopher Zoeller is supported by the German Research Foundation (Deutsche Forschungsgemeinschaft, DFG) under project DFG ID: 387081806. In addition the authors gratefully recognize the Gauss Centre for Supercomputing e.V. (www.gauss-centre.eu) for providing computing time at the Leibniz Supercomputing Centre (www.lrz.de). Stefan Adami also wants to acknowledge support of the German Research Foundation (Deutsche Forschungsgemeinschaft, DFG) through project 389373218.

References

[1] S. Adami, X. Hu, N. Adams, A new surface-tension formulation for multi-phase SPH using a reproducing divergence approximation, J. Comput. Phys. 229 (2010) 5011–5021, https://doi.org/10.1016/j.jcp.2010.03.022, http://linkinghub.elsevier.com/retrieve/pii/S0021999110001324.
[2] M. Hirschler, G. Oger, U. Nieken, D. Le Touzé, Modeling of droplet collisions using smoothed particle hydrodynamics, Int. J. Multiph. Flow 95 (2017) 175–187.
[3] A. Zhang, P. Sun, F. Ming, An sph modeling of bubble rising and coalescing in three dimensions, Comput. Methods Appl. Mech. Eng. 294 (2015) 189–209.
[4] J. Weirather, V. Rozov, M. Wille, P. Schuler, C. Seidel, N.A. Adams, M.F. Zaeh, A smoothed particle hydrodynamics model for laser beam melting of ni-based alloy 718, Comput. Math. Appl. 78 (2019) 2377–2394.
[5] C.W. Hirt, B.D. Nichols, Volume of fluid (vof) method for the dynamics of free boundaries, J. Comput. Phys. 39 (1981) 201–225.
[6] S. Osher, J.A. Sethian, Fronts propagating with curvature-dependent speed: Algorithms based on Hamilton-Jacobi formulations, J. Comput. Phys. 79 (1988) 12–49.
[7] Z.-B. Wang, R. Chen, H. Wang, Q. Liao, X. Zhu, S.-Z. Li, An overview of smoothed particle hydrodynamics for simulating multiphase flow, Appl. Math. Model. 40 (2016) 9625–9655.
[8] J.U. Brackbill, D.B. Kothe, C. Zemach, A continuum method for modeling surface tension, J. Comput. Phys. 100 (1992) 335–354.
[9] S. Nugent, H. Posch, Liquid drops and surface tension with smoothed particle applied mechanics, Phys. Rev. E 62 (2000) 4968.
[10] A. Tartakovsky, P. Meakin, Modeling of surface tension and contact angles with smoothed particle hydrodynamics, Phys. Rev. E 72 (2005) 026301.
[11] A.M. Tartakovsky, A. Panchenko, Pairwise force smoothed particle hydrodynamics model for multiphase flow: surface tension and contact line dynamics, J. Comput. Phys. 305 (2016) 1119–1146.
[12] J.P. Morris, Simulating surface tension with smoothed particle hydrodynamics, Int. J. Numer. Methods Fluids 33 (2000) 333–353, https://doi.org/10.1002/1097-0363(20000615)33:3<333::AID-FLD11>3.0.CO;2-7.
[13] M. Hopp-Hirschler, U. Nieken, A Smoothed Particle Hydrodynamics approach for thermo capillary flows, Comput. Fluids 176 (2018) 1–19, https://doi.org/10.1016/j.compfluid.2018.09.010.
[14] K. Szewc, J. Pozorski, J.-P. Minier, Simulations of single bubbles rising through viscous liquids using smoothed particle hydrodynamics, Int. J. Multiph. Flow 50 (2013) 98–105.
[15] Q. Yang, J. Yao, Z. Huang, M. Asif, A comprehensive SPH model for three-dimensional multiphase interface simulation, Comput. Fluids 187 (2019) 98–106, https://doi.org/10.1016/j.compfluid.2019.04.001, URL.
[16] B. Lafaurie, C. Nardone, R. Scardovelli, S. Zaleski, G. Zanetti, Modelling merging and fragmentation in multiphase flows with surfer, J. Comput. Phys. 113 (1994) 134–147.
[17] X. Hu, N. Adams, A multi-phase SPH method for macroscopic and mesoscopic flows, J. Comput. Phys. 213 (2006) 844–861, https://doi.org/10.1016/j.jcp.2005.09.001, http://linkinghub.elsevier.com/retrieve/pii/S0021999105004195.
[18] N. Grenier, D. Le Touzé, A. Colagrossi, M. Antuono, G. Colicchio, Viscous bubbly flows simulation with an interface sph model, Ocean Eng. 69 (2013) 88–102.
[19] A. Krimi, M. Rezoug, S. Khelladi, X. Nogueira, M. Deligant, L. Ramírez, Smoothed Particle Hydrodynamics: A consistent model for interfacial multiphase fluid flow simulations, J. Comput. Phys. 358 (2018) 53–87, https://doi.org/10.1016/j.jcp.2017.12.006.
[20] L. Yang, M. Rakhsha, D. Negrut, Comparison of surface tension models in smoothed particles hydrodynamics method, in: International Design Engineering Technical Conferences and Computers and Information in Engineering Conference, vol. 59261, American Society of Mechanical Engineers, 2019, V006T09A028.
[21] S. Adami, X. Hu, N. Adams, A conservative SPH method for surfactant dynamics, J. Comput. Phys. 229 (2010) 1909–1926, https://doi.org/10.1016/j.jcp.2009.11.015, http://linkinghub.elsevier.com/retrieve/pii/S0021999109006342.
[22] M. Huber, F. Keller, W. Säckel, M. Hirschler, P. Kunz, S.M. Hassanizadeh, U. Nieken, On the physically based modeling of surface tension and moving contact lines with dynamic contact angles on the continuum scale, J. Comput. Phys. 310 (2016) 459–477.
[23] T. Breinlinger, P. Polfer, A. Hashibon, T. Kraft, Surface tension and wetting effects with smoothed particle hydrodynamics, J. Comput. Phys. 243 (2013) 14–27.
[24] M. Olejnik, J. Pozorski, A robust method for wetting phenomena within smoothed particle hydrodynamics, Flow Turbul. Combust. 104 (2020) 115–137.
[25] F. Yeganehdoust, M. Yaghoubi, H. Emdad, M. Ordoubadi, Numerical study of multiphase droplet dynamics and contact angles by smoothed particle hydrodynamics, Appl. Math. Model. 40 (2016) 8493–8512.
[26] X. Dong, Z. Li, X. Zhang, Contact-angle implementation in multiphase smoothed particle hydrodynamics simulations, J. Adhes. Sci. Technol. 32 (2018) 2128–2149.
[27] A. Farrokhpanah, B. Samareh, J. Mostaghimi, Applying contact angle to a 2D multiphase smoothed particle hydrodynamics model, J. Fluids Eng. 137 (4) (2015), https://doi.org/10.1115/1.4028877.
[28] F.S. Schranner, N.A. Adams, A conservative interface-interaction model with insoluble surfactant, J. Comput. Phys. 327 (2016) 653–677.
[29] S.L. Carnie, L. Del Castillo, R.G. Horn, Mobile surface charge can immobilize the air/water interface, Langmuir 35 (2019) 16043–16052.
[30] J.J. Monaghan, H.E. Huppert, M.G. Worster, Solidification using smoothed particle hydrodynamics, J. Comput. Phys. 206 (2005) 684–705, https://doi.org/10.1016/j.jcp.2004.11.039, http://linkinghub.elsevier.com/retrieve/pii/S0021999105000112.
[31] J.P. Morris, P.J. Fox, Y. Zhu, Modeling low Reynolds number incompressible flows using SPH, J. Comput. Phys. 136 (1997) 214–226.
[32] S. Adami, X. Hu, N. Adams, Simulating three-dimensional turbulence with SPH, in: Proceedings of the Summer Program, 2012, p. 177, http://citeseerx.ist.psu.edu/viewdoc/download?doi=10.1.1.386.2820&rep=rep1&type=pdf, http://ctr.stanford.edu/Summer/SP12/02.11_adami.pdf.

[33] P. Incardona, A. Leo, Y. Zaluzhnyi, R. Ramaswamy, I.F. Sbalzarini, Openfpm: A scalable open framework for particle and particle-mesh codes on parallel computers, Comput. Phys. Commun. 241 (2019) 155–177.
[34] G.-R. Liu, M.B. Liu, Smoothed particle hydrodynamics: a meshfree particle method, World scientific, 2003.
[35] J. Hongbin, D. Xin, On criterions for smoothed particle hydrodynamics kernels in stable field, J. Comput. Phys. 202 (2005) 699–709.
[36] M. Liu, G. Liu, Smoothed particle hydrodynamics (SPH): an overview and recent developments, Arch. Comput. Methods Eng. 17 (2010) 25–76.
[37] X. Hu, N.A. Adams, An incompressible multi-phase sph method, J. Comput. Phys. 227 (2007) 264–278.
[38] X. Hu, N. Adams, Angular-momentum conservative smoothed particle dynamics for incompressible viscous flows, Phys. Fluids 18 (2006) 101702.
[39] J.J. Monaghan, Sph without a tensile instability, J. Comput. Phys. 159 (2000) 290–311.
[40] J.P. Morris, A study of the stability properties of smooth particle hydrodynamics, Publ. Astron. Soc. Aust. 13 (1996) 97–102.
[41] S. Adami, X.Y. Hu, N.A. Adams, A transport-velocity formulation for smoothed particle hydrodynamics, J. Comput. Phys. 241 (2013) 292–307, https://doi.org/10.1016/j.jcp.2013.01.043, http://linkinghub.elsevier.com/retrieve/pii/S002199911300096X.
[42] J. Wu, S.-T. Yu, B.-N. Jiang, Simulation of two-fluid flows by the least-squares finite element method using a continuum surface tension model, Int. J. Numer. Methods Eng. 42 (1998) 583–600.
[43] J.J. Monaghan, Smoothed particle hydrodynamics, Annu. Rev. Astron. Astrophys. 30 (1992) 543–574.
[44] P.W. Cleary, J.J. Monaghan, Conduction modelling using smoothed particle hydrodynamics, J. Comput. Phys. 148 (1999) 227–264.
[45] M. Muradoglu, G. Tryggvason, A front-tracking method for computation of interfacial flows with soluble surfactants, J. Comput. Phys. 227 (2008) 2238–2262.
[46] M. Herrmann, J. Lopez, P. Brady, M. Raessi, Thermocapillary motion of deformable drops and bubbles, in: Proceedings of the Summer program, Stanford University, Center for Turbulence Research, 2008, p. 155.
[47] K.E. Teigen, P. Song, J. Lowengrub, A. Voigt, A diffuse-interface method for two-phase flows with soluble surfactants, J. Comput. Phys. 230 (2011) 375–393.
[48] N. Young, J. Goldstein, M.J. Block, The motion of bubbles in a vertical temperature gradient, J. Fluid Mech. 6 (1959) 350–356.
[49] Y.Y. Yan, Y.Q. Zu, A lattice boltzmann method for incompressible two-phase flows on partial wetting surface with large density ratio, J. Comput. Phys. 227 (2007) 763–775.
[50] T. Pravinraj, R. Patrikar, Modelling and investigation of partial wetting surfaces for drop dynamics using lattice boltzmann method, Appl. Surf. Sci. 409 (2017) 214–222.
[51] Q. Chang, J. Alexander, Analysis of single droplet dynamics on striped surface domains using a lattice boltzmann method, Microfluid. Nanofluid. 2 (2006) 309–326.
[52] Y.Q. Zu, Y.Y. Yan, Lattice boltzmann method for modelling droplets on chemically heterogeneous and microstructured surfaces with large liquid–gas density ratio, IMA J. Appl. Math. 76 (2011) 743–760.

Appendix B

Numerical investigation of balling defects in laser-based powder bed fusion of metals with Inconel 718

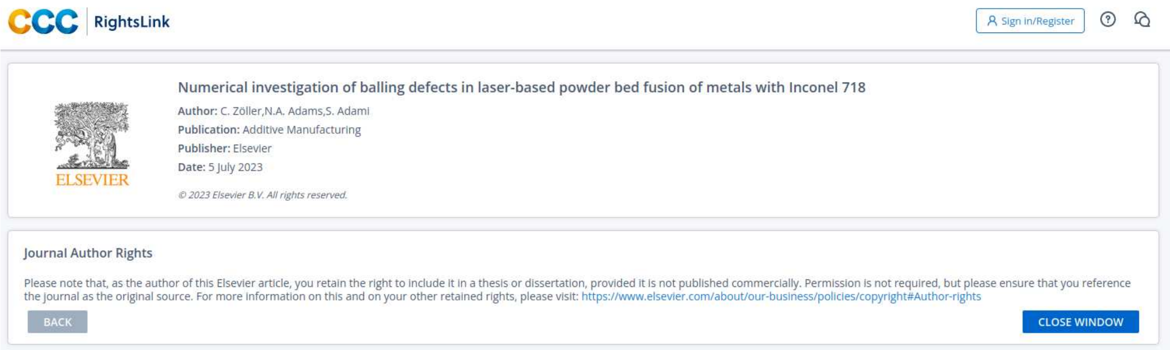
RightsLink

Sign in/Register

Numerical investigation of balling defects in laser-based powder bed fusion of metals with Inconel 718

Author: C. Zöller,N.A. Adams,S. Adami

Publication: Additive Manufacturing

Publisher: Elsevier

Date: 5 July 2023

© 2023 Elsevier B.V. All rights reserved.

Journal Author Rights

Please note that, as the author of this Elsevier article, you retain the right to include it in a thesis or dissertation, provided it is not published commercially. Permission is not required, but please ensure that you reference the journal as the original source. For more information on this and on your other retained rights, please visit: https://www.elsevier.com/about/our-business/policies/copyright#Author-rights

BACK

CLOSE WINDOW

Additive Manufacturing 73 (2023) 103658

Contents lists available at ScienceDirect

Additive Manufacturing

journal homepage: www.elsevier.com/locate/addma

Research paper

Numerical investigation of balling defects in laser-based powder bed fusion of metals with Inconel 718

C. Zöller [a,*], N.A. Adams [a,b], S. Adami [a,b]

[a] Technical University of Munich, TUM School of Engineering and Design, Chair of Aerodynamics and Fluid Mechanics, Boltzmannstraße 15, 85748 Garching, Germany

[b] Technical University of Munich, Munich Institute of Integrated Materials, Energy and Process Engineering, Lichtenbergstraße 4a, 85748 Garching, Germany

ARTICLE INFO

Keywords:
Smoothed particle hydrodynamics
SPH
Balling
Process map
Single melt track defect
Powder bed fusion
Selective laser melting

ABSTRACT

Balling is one of the main single melt track defects limiting stable production of dense parts with laser-based powder bed fusion of metals (PBF-LB/M) additive manufacturing. A fundamental understanding of balling therefore is critical for process control and optimization. Violent interface dynamics present a severe challenge for mesh-based numerical schemes, and can be dealt with by particle methods. In this study, we focus on investigating single melt tracks by smoothed particle hydrodynamics (SPH). The considered regime is characterized by long liquid melt pools and remelting of the previous layer. The balling mechanism is driven by Marangoni and capillary forces. The resulting convective melt flux leads to the accumulation of melt in the tail region and leaves an exposed area of marginal layer build-up. In addition to the competing mechanisms of solidification and spreading, a competition between spreading and melt contraction shortly after the melt pinch-off is observed. We find a similar balling behavior yet different ball size at different laser power settings. We stress that SPH with accurate interface modeling has the capability to quantify balling processes and to improve the understanding of balling mechanisms.

1. Introduction

Laser-based powder bed fusion is becoming an increasingly competitive manufacturing technique. A high energy laser beam is applied to selectively melt powder particles within a powder bed. The molten particles coalesce to form a melt pool that subsequently fuses and consolidates with the previous layer of material. With an appropriate selection of process parameters a successive layer-by-layer buildup allows for the fabrication of dense parts with high design flexibility, for instance, by enabling complex part production down to the micro scale and tailored material properties. Powder bed fusion is applied to a variety of materials such as alloys [1,2], ceramics [3] and polymers [4] and is also utilized in the development of new material composites [5,6]. Hence, laser-based powder bed fusion is a promising addition to established formative and substractive manufacturing approaches.

The fundamental building unit in laser-based powder bed fusion is the single melt track since each manufactured layer is composed of consecutive single tracks. Manufacturing defects of final parts often originate from melt-flow instabilities during single track formation. It is important to understand the defect generation in single track melt pools and their dependence on process parameters. Much effort has been dedicated to identify process maps that lead to stable single melt tracks [7–9], where a known process map constraint is due to melt pool balling.

Balling describes the breakup of continuous melt pools into melt agglomerates. The process is also referred to as ’aggregation of melt islands’ or ‘humps’ [10,11]. It is found to occur in melt tracks of quite different materials such as aluminum [12], titanium [9], nickel [13], and steel [14] alloys. As balling is observed at high laser scan speeds in combination with both high [15] and low [10] laser power, as well as low laser scan speeds and high laser power [16], it is considered as one of the key defect mechanisms [1]. Large-size balling can cause a non-uniform powder distribution in the consecutive powder layer, poor wettability of the previous layer [2,3], pore formation [14], and even an interruption of the build process due to a collision with the paving roller [14]. Final parts show a rough surface morphology [14], higher porosity [15] or poor inter layer bonding [17] around balls.

Several factors are identified to affect balling in single track melt pools. In general, balling occurs due to a minimization of the surface free energy by capillary forces. The overall intensity of capillary forces depends on melt temperature as, for many materials, surface tension decreases with increasing temperature. Consequently, Marangoni

* Corresponding author.
E-mail addresses: christopher.zoeller@tum.de (C. Zöller), nikolaus.adams@tum.de (N.A. Adams), stefan.adami@tum.de (S. Adami).

https://doi.org/10.1016/j.addma.2023.103658
Received 7 February 2023; Received in revised form 16 June 2023; Accepted 18 June 2023
Available online 22 June 2023

flow induced by high temperature gradients at the melt pool surface contributes to the breakup of continuous tracks [18]. Balling is further driven by poor wettability between the liquid metal and its surrounding powder particles and substrate [12,16,17,19]. Insufficient remelting of the previous layer is particularly problematic when oxide layers are formed on the substrate, as they increase the wetting angles between the liquid and solid material [20]. Sufficient remelting therefore is important to destroy such oxide layers [21] as well. Additionally, oxidation can invert surface tension gradients leading to surface flows directed towards the melt pool center and thus support melt aggregation [6]. At low power density settings balling can occur in the form of melt island-aggregates. Insufficient heating leads to partially melted particles, unmelted substrate beneath the powder, and a melt pool that tends to cluster rather than wet the surface [22,23]. Low melt temperatures and thus high melt viscosity and surface tension further enhance the process [1,5,14]. A commonly suggested solution to avoid such events is to increase the energy input [1] or reduce the powder layer thickness [9]. At high scan velocities, the melt pool width and thus the wetted substrate area decreases [24]. Long and narrow melt pools are prone to the Plateau–Rayleigh instability [2,3,7,10,13,15–18,24–26]. Poor melt pool spreading and shallow melt pool penetration further enhance the pool instability and breakup [7,12,14]. Analytical stability models [7,11,21,27] are used as breakup conditions for continuous single melt tracks [12,28–30], yet their ability to predict the onset of balling is still in question [31]. As the melt-pool-length-to-diameter ratio increases with increasing laser scan velocity, the melt pool is particularly susceptible to Plateau–Rayleigh instabilities in the process window of high scan speed and high laser power [24]. Ball formation also is found at low scan speeds and high energy input. High energy content within the melt pool reduces the rate of solidification. Hence, the time scale at which surface tension affects pool breakup increases as well [30]. This type of balling at large liquid formation is referred to as 'self balling' [16,32]. Ball formation itself is identified as a competitive non-equilibrium process between melt spreading and solidification [8,33,34]. Final droplet shapes depend on the complex interplay of capillary forces, inertia, solidification, thermal properties and heat content [33]. While balling is avoided when the melt can spread out before it solidifies, quick cooling rates lead to premature termination of spreading and enhance balling [8].

Extensive research is required to better understand the multitude of simultaneous mechanisms and to identify and enhance process maps for stable production. Process complexity in combination with temporal and spatial scales at the micro level make experimental in-situ measurements infeasible. Hence, increasing attention is devoted to numerical investigations [3,9,16,17,22,25,35–37]. An adequate representation of selective laser melting at the powder scale, however, requires comprehensive numerical modeling. Its multi-phase nature in combination with phase transitions and complex interface topologies with strong deformations pose severe challenges to the underlying algorithms.

Yet, several numerical studies are able to reproduce the balling phenomenon and allow for an in-depth analysis of the melt-pool breakup process. Ren et al. [22] apply the finite volume method in combination with a volume-of-fluid interface algorithm and ray-tracing laser model to study the absorptive behavior and flow kinetics of a copper alloy. Their single melt track study shows intense absorptivity oscillations, which are ascribed to balling and result in increased exposure of substrate rather than melt to the laser beam. A discrete element method including viscous coalescence and densification models has been used for the study of balling phenomena of a nickel alloy by Boutaous et al. [35]. Large variations of melt track widths indicate the presence of balling. From a sensitivity study on surface tension and viscosity they conclude that neither of the two have a significant influence on balling as coalescence of the melt is too fast. Li et al. [17] apply a phase-field method to 2D simulations of single melt tracks for pure nickel powder on stainless steel substrate. Their study of various wetting conditions between melt and substrate reveals a decreasing frequency of melt pool breakup for low wetting angles. Single melt track simulations of 316L stainless steel show discontinuous tracks and melt agglomeration at partially melted powder particles [36]. The finite volume method algorithm by Gu et al. [37] is coupled with the volume of fluid interface model to study melt pool behavior in multi-layer scenarios. They show that the melt track of the first layer is discontinuous and exhibits melt agglomerates. A subsequent second layer leads to further clustering of melt and lack of fusion between the two layers. While at an increased power density a wavy but continuous first melt track is formed, in the second layer balling still occurs. It is concluded that the surface morphology of the first layer contributes to balling of consecutive layers. Single melt tracks of AlSi10Mg are investigated by Yu et al. [16] with a finite volume algorithm and volume of fluid interface treatment. They find melt pool breakup at high power densities. A detailed analysis of heating, melting and coalescing process of two powder particles reveals a flow pattern dominated by buoyancy and capillary forces. In [3], Moniz et al. apply a finite element method and the level-set interface method to study laser beam melting of Al2O3 oxide ceramics. They find the frequency of balling to increase with a reduction of power densities. They point out the lack of layer build up between balls due to the melt agglomeration. Balling of single melt tracks of titanium alloy Ti6Al4V is investigated by Yan et al. [9]. The results show partial melting of powder particles and a lack of substrate melting. The study of different powder setups reveals an independence of balling from the random powder packing, yet a strong dependence on the powder size distribution and powder layer thickness.

Most numerical research on balling processes is focused on balling in a regime characterized by low power densities, partially melted powder particles and small melt pools. Results show only slight or no melting of the substrate [10,16,17,22]. In this regime the low amount of melt commonly is given as reason for melt pool balling [1,3,16,36,37]. However, balling also occurs when there is full powder- and considerable substrate-melting [38]. Yet, a detailed numerical study of balling in this important part of the process map still is missing from literature. A material of particular interest for aerospace applications is the Inconel 718 nickel-based superalloy. Like many other alloys, the process map suffers from limitations in process parameter choice due to balling. Both, analytically [28] and experimentally [38] estimated power-scan-speed process maps including a balling threshold are available in literature. Only few numerical studies on balling can be found, none of which focuses on the analysis of driving forces of balling. Additionally, the majority of numerical research into balling is conducted with mesh based methods such as finite volume or finite element methods.

The aim of this work is to close the gap of balling research in the regime defined by a fully melted powder bed and considerable substrate remelting. We focus on the contribution of driving forces on the breakup mechanism and the ball formation in this regime. Thus, the research into balling of Inconel 718 melt tracks is extended by a more quantitative comparison of forces. To that end, we conduct several single melt track simulations at different laser power and laser scan speed settings. First, the simulation results are validated by comparison of melt pool depth and width with experimental data. Then, we focus on the balling process and compare simulation results at process parameter sets both with the presence and absence of balling to analytical and experimental references followed by an analysis of the underlying physical mechanisms. We also demonstrate the capability of smoothed particle hydrodynamics (SPH) to resolve such complex multi-phase phenomena, which to the best of our knowledge, has not been previously applied to the problem of balling in laser powder bed fusion. The remainder of this work is as follows: In section two, the physical model is introduced, relevant simplifications are stated and the numerical setup is described. Simulation results are shown and discussed in section three. Concluding remarks and observations are presented in the closing section.

2. Materials and methods

In this work smoothed particle hydrodynamics (SPH) is applied [39]. In contrast to finite volume or finite element methods it implicitly tracks the interface without requiring computationally demanding interface location and tracking algorithms making it particularly suitable for simulations that involve complex interfaces movements. SPH particles convect with the flow field eliminating the need for complex re-meshing or moving meshes. The method also is highly adaptable for simulating complex powder bed structures and fluid–solid boundaries, as different particles can be used for different materials. Additionally, the SPH method is stable for strong interface deformations, which makes it an ideal choice for simulating dynamic melt-pools and the balling process. For the accurate prediction of melt pool morphology and balling a WCSPH multi-phase model [40] is employed, extended by transport-velocity [41] and consistent boundary conditions [42]. For an accurate representation of melt pool dynamics, pressure, viscous, and gravity forces are taken into account. Evaporation effects on the melt are considered by a recoil-pressure model [43]. To account for the driving forces of balling, both capillary and Marangoni forces as well as wetting conditions are incorporated at the melt surface following [44]. A wetting angle of 70 degrees is chosen based on experimental contact angles measurements [8,45] and the cross section morphology in [38]. A precise representation of the energy balance is achieved by modeling thermal conduction in melt, powder and substrate [46], convective cooling by an ambient gas, evaporative cooling, a laser heat source, and solid–liquid phase change, considering the latent heat of melting and solidification. Material models from literature are applied to account for the temperature dependence of viscosity, surface tension, thermal conductivity, heat capacity and laser absorptivity, see A.3.

No ambient gas flow is induced and the surrounding gas is treated as isothermal to represent convective cooling. Thermal expansion within the melt pool and possibly resulting buoyancy forces are ignored. Thermal radiation and viscous heating are discarded. The applied absorptivity model accounts for the incidence angle, the dependence on temperature and an energy input at the material surface. As it does not consider multi-reflections within the vapor cavity, absorptivity is increased to match the target melt pool dimensions. While recoil pressure and evaporative cooling are included, mass loss due to evaporation is neglected. To account for increased viscosity of the melt in the mushy zone and to stabilize the simulations the dynamic viscosity is increased by a factor of ten, following [47,48]. The powder layer is explicitly resolved, yet powder particle motion is not incorporated at this stage.

The conservation laws of mass, momentum and energy govern the fluid mechanics and energy balance of balling. For incompressible fluids, the set of equations in Lagrangian form is

$$\frac{d\rho}{dt} = -\rho\, \nabla \cdot \mathbf{v}, \tag{1}$$

$$\frac{d\mathbf{v}}{dt} = \mathbf{F}^p + \mathbf{F}^\nu + \mathbf{F}^\sigma + \mathbf{F}^{ev} + \mathbf{F}^g, \tag{2}$$

$$\frac{dh}{dt} = Q^\lambda + Q^{ev} + Q^l, \tag{3}$$

where ρ, $\mathbf{v}$ and h are density, velocity, and enthalpy, respectively. Lagrangian-particle acceleration is due to pressure ($\mathbf{F}^p$), viscous ($\mathbf{F}^\nu$), surface tension ($\mathbf{F}^\sigma$), recoil pressure ($\mathbf{F}^{ev}$) and gravity ($\mathbf{F}^g$) forces. Changes in enthalpy are induced by thermal conduction $\left(Q^\lambda\right)$, evaporative cooling (Q^{ev}) and laser irradiation $\left(Q^l\right)$.

Pressure forces follow from gradients of the pressure field p as

$$\mathbf{F}^p = -\frac{1}{\rho}\nabla p. \tag{4}$$

Viscous forces are determined by the divergence of the strain rate tensor as

$$\mathbf{F}^\nu = \frac{1}{\rho}\nabla \cdot (\mu \nabla v), \tag{5}$$

where μ is the temperature dependent dynamic viscosity. At the melt ambient-gas interface, both capillary and Marangoni forces,

$$\mathbf{F}^\sigma = \frac{1}{\rho}\left[\sigma\kappa\mathbf{n} + \nabla_s \sigma\right], \tag{6}$$

are applied. Here, σ, κ, $\mathbf{n}$, and ∇_s are the surface tension coefficient, interface curvature, interface normal vector and surface tangential gradient operator, respectively. Note that, no special interface capturing and tracking algorithms are needed as SPH naturally handles different phases with separate particles. Wetting of melt on the substrate and powder is modeled by Young's equation

$$\sigma^{solid-gas} = \sigma^{solid-liquid} + \sigma^{liquid-gas}\cos\theta, \tag{7}$$

where an equilibrium between solid, liquid and gas surface tension is achieved at the wetting angle θ. To account for the recoil pressure force we apply an approach based on the Clausius-Clapeyron equation for ideal gases assuming a constant latent heat of phase change

$$\mathbf{F}^{ev} = \frac{1}{\rho} A\, c_1\, p_\infty \exp\left(\frac{\Delta H_{mol}}{R}\left(\frac{1}{T} - \frac{1}{T_{ev}}\right)\right), \tag{8}$$

with the evaporating surface area A, coefficient $c_1 = 0.54$, ambient pressure p_∞, molar latent heat of evaporation ΔH_{mol}, universal gas constant R, temperature T and boiling temperature T_{ev}, respectively [49]. Finally, gravity g acts as body force

$$\mathbf{F}^g = -g. \tag{9}$$

On the right-hand-side of the energy equation, Fourier's law of thermal conduction

$$Q^\lambda = \nabla \cdot (\lambda \nabla T), \tag{10}$$

with thermal conductivity λ is used in the melt, gas, and solid phase. Evaporative cooling of the melt is determined from the enthalpy flux of the evaporating material. Here, the mass flux approximation from [49] is given by

$$J_{ev} = c_2\, c_3\, p_r \sqrt{\frac{M}{2\pi R\, T}}, \tag{11}$$

where the coefficient $c_2 = 0.82$ and the sticking coefficient $c_3 = 1$ are chosen according to [49]. In Eq. (11), p_r is the recoil pressure and M the atomic mass of the evaporating (melt-) material. Evaporative cooling follows as

$$Q^{ev} = -A\,\left(h + h_{ev}\right) J_{ev}, \tag{12}$$

where both the enthalpy h and the specific heat of evaporation h_{ev} are considered. This heat sink is applied at the interface between melt and the ambient gas phase. Finally, laser irradiation is modeled by a Gaussian energy source term

$$Q^l = -\alpha \Omega A\, \frac{8\, P}{\pi d_s^2} \exp\left(-8\left(\frac{r_0 - r}{d_s}\right)^2\right) \tag{13}$$

with absorptivity α, directional absorptance correction Ω, laser power P, laser spot diameter d_s, laser axis location r_0 and radial coordinate r. Ω is approximated by Schlick's approach $\Omega = 1 - (1 - \cos(\phi))^5$, where ϕ is the angle between the laser axis and the incident area normal vector [50]. The energy deposition is considered to occur at the phase interface only [43].

Phase change is modeled in SPH by simply transforming particles from one phase to another. As criterion, we use an enthalpy threshold where latent heat of fusion and solidification is considered within the threshold. The rate of temperature change in the mushy zone between the two states is considered through specific heat capacity models, see A.3.

The set of equations is closed by Cole's [51] equation of state

$$p = p_0\left(\left(\frac{\rho}{\rho_0}\right)^\gamma - 1\right). \tag{14}$$

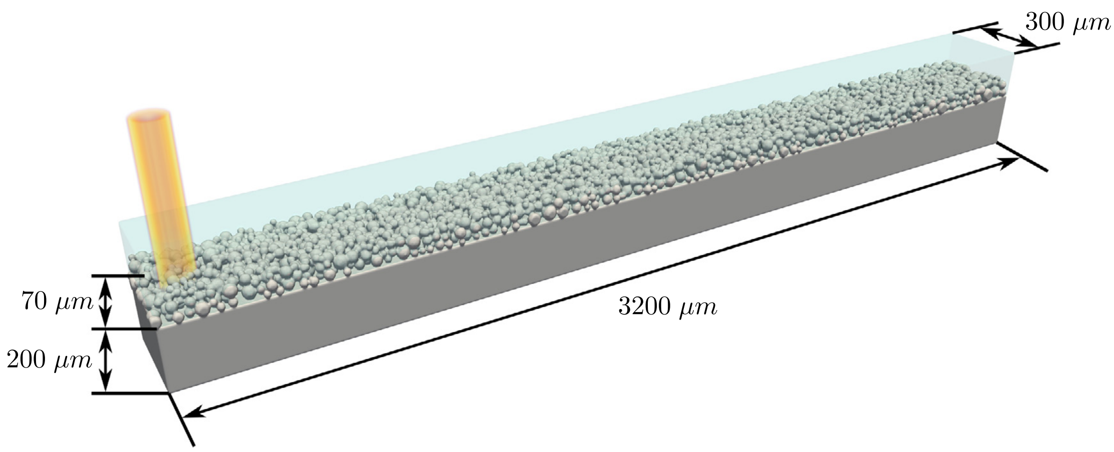

Fig. 1. Domain dimensions of substrate, powder and ambient gas. Laser scan path from $x = 0$ to $x = 3000$ μm.

Table 1
Single melt track simulation parameters.

Serial number	Laser power [W]	Scan speed [mm/s]	LED [J/m]	VED [J/mm^3]	Balling
1	180	800	225	32.1	No
2	200	1000	200	28.6	No
3	200	1200	167	23.8	Yes
4	240	800	300	42.9	No
5	250	1000	250	35.7	No
6	250	1200	208	29.8	Yes
7	300	1000	300	42.9	No

Here, reference pressure p_0 and isotropic exponent γ are chosen to limit density variations to 1% of the reference density ρ_0.

The set of equations is evolved in time using an explicit Velocity-Verlet time integration scheme [52]. The maximum allowed time-step size follows from the most restrictive stability condition out of the viscous, surface tension, recoil pressure, thermal conduction, and CFL criterion [44,46,53,54].

2.1. Numerical setup

We study single melt track balling of Inconel 718 material at different process conditions. The numerical results are validated with experimental data of Scime and Beuth [38]. In their work, ex-situ recordings of single melt tracks are presented for 36 parameter sets. At each power and scan speed combination 10 single tracks are generated with an EOS M290 machine. The investigated process map covers both stable parameters for constant melt tracks, as well as unstable parameter sets showing defects like balling.

Scime and Beuth use the nickel alloy Inconel 718. The base plate is an Inconel 718 plate from McMaster-Carr (P/N: 1099N8) and the powder material is Inconel 718 from EOS with a composition of Ni 50–55 wt%, Cr 17.0–21.0 wt%, Nb 4.75–5.5 wt%, Mo 2.8–3.3 wt%, Ti 0.65–1.15 wt%. For an accurate representation of the material, temperature dependent material properties are incorporated into the numerical model. The corresponding material models are extracted from [43] and listed in A.3.

In Scime and Beuth [38] a powder layer thickness of 70 ± 20 μm is chosen to achieve a target nominal 40 μm fused layer build-up. Thus, a consolidation factor $\left(1 - \rho_{powder}/\rho_{fused}\right)$ of 40% is assumed. No further specifications about the powder size distribution are made. To mimic a comparable powder bed setup, we apply the drop and roll algorithm from Zhou et al. [55]. The initial powder-size distribution of particles to be dropped follows a normal distribution defined by a mean diameter of 30 μm, a standard deviation of 10 μm, and a minimum and maximum particle diameter of 20 μm and 50 μm, respectively. Particles extending beyond a layer height of 70 μm are discarded. The resulting powder bed is defined by a packing density of 55%, slightly below the assumed 60% of the experiments.

The same computational setup is used in all simulations. The dimensions of the physical domain are set to 3200 μm x 300 μm x 370 μm (length, width, height). It is enclosed by three layers of boundary particles. With a uniform spatial discretization of $\Delta x = 3.5$ μm, the total number of SPH particles amounts to 9395040. The laser spot is resolved by about 33 SPH particles across its diameter, and the smallest powder particle is resolved by at least 5 SPH particles across its diameter. In Fig. 1 the simulation setup is shown. At initialization, the domain consists of a 3200 μm × 300 μm × 200 μm substrate plate, covered by a powder layer of thickness $l_p = 70$ μm. The remainder of the domain is filled with argon, shown in light blue in Fig. 1. In correspondence with the experiments, the domain is initialized at $80°C$ to resemble preheating. At all domain boundaries, isothermal no-slip boundary conditions are enforced. The laser is initially placed at position $[0, 0, 0]$, as indicated in Fig. 1. Throughout the simulation the laser moves at a constant scan speed u. The simulation is stopped once the laser has travelled 3000 μm. The laser spot diameter is set in accordance with the experiments to 100 μm. All investigated process parameter sets of laser power and laser scan speed are listed together with their corresponding linear energy densities $LED = P/u$ and volumetric energy densities $VED = P/\left(u\, d_s\, l_p\right)$ in Table 1. The quintic spline kernel is applied with a smoothing length equal to the particle spacing and cut-off radius $r = 3\Delta x$. For a reference length of 21 μm, reference velocity of 10 m/s and a numerical sound speed of 100 m/s the physical time step size is 7.95 ns.

To allow for high numerical resolutions at moderate computation times, the algorithm utilizes the scaleable OpenFPM C++ framework [56]. The applied domain decomposition, communication, data structures, memory management and cell lists ensure an execution of the comprehensive set of numerical models at reasonable computation times. All simulations were carried out on NVIDIA GeForce RTX 2080 Ti GPUs, and the computational time for 2500 μs physical time ranged from 291 to 360 h depending on the process parameter set.

3. Results and discussion

Since melt pool dimensions are of particular importance for the melt breakup process, we first validate them by comparison with experimental data. Next, the ability of the model to predict balling and non-balling parameter sets is assessed. Finally, the melt pool breakup and balling process is investigated to clarify detailed defect mechanisms.

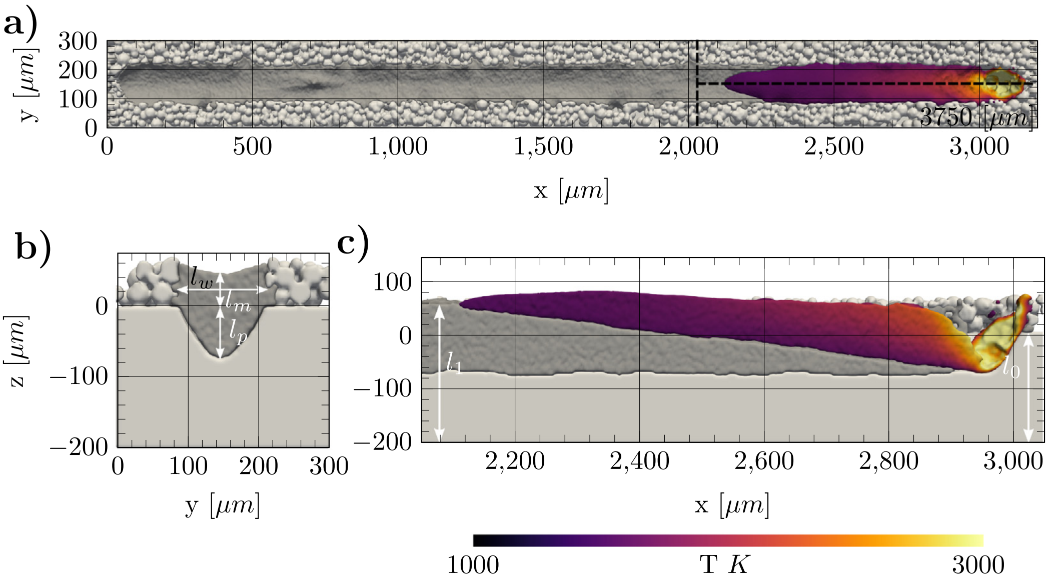

Fig. 2. Single melt track at process conditions #1 (a) in top view, (b) solidified material in transverse cross section view and (c) melt pool in longitudinal cross section view.

3.1. Validation of melt-track dimensions

In order to validate the numerical model, we first compare the accuracy of the simulated single melt tracks to experimental data. The process map from Scime and Beuth [38] suggests a smooth melt pool without balling at the process conditions for cases #1, #2, #4, #5 and #7 in Table 1. Top view, solidified track cross section, and longitudinal melt-pool profile of case #1 are shown as example of a stable single melt track in Fig. 2. At these process conditions a continuous melt pool without significant variance in width develops and is maintained along the scan path. The color coded temperature field, Fig. 2, indicates high temperature within the radiation zone followed by a rapid cooling towards the trailing region of the melt-pool. The longitudinal cross-section view reveals a vapor cavity at the laser irradiation zone followed by a smooth melt-pool topology. The powder layer is fully melted and a sufficient penetration depth into the substrate ensures fusion between the consecutive layers. In the vertical cross-section view the maximum track width l_w, penetration depth into the substrate l_p and consolidated material layer build-up l_m are sketched. The respective total track height follows from the sum of build-up and penetration depth as $l_h = l_p + l_m$. Layer build-up is achieved as the new substrate height l_1 exceeds the initial substrate height l_0, as shown in Fig. 2 (c).

In Table 2, single-melt-track width and depth results are summarized. For cases #1, #2, #4, #5 and #7 the total track height is stated while for the balling cases #3 and #6 the penetration depth is given. We compare the results with lines of constant melt pool geometry from Scime and Beuth [38]. With a melt track width of 148 μm for case #4, 155 μm for case #7, and track depths of 115 μm and 115 μm for cases #1 and #2, the experimental data are met within an relative deviation of 15 %. Single-track widths and depths of all simulations reside between their corresponding lines of constant melt pool dimension, see Fig. 5 in [38]. Hence, the results indicate the ability of the numerical model to accurately predict the single melt track proportions.

3.2. Balling validation

Next, the occurrence of balling at different process parameter settings is compared with experimental data. In [38], the probabilities of balling at various points in the power-scan-speed map are presented. They are identified from the number of examined cross-sections that exhibit a balling morphology at the specific process parameters. Based on these findings, no balling is expected for cases #2 and #5, while balling is likely to occur in cases #3 and #6. Hence, we choose these four parameter sets to assess the numerical prediction of melt pool breakup and balling. Fig. 3 presents the simulation results in the longitudinal cut through the domain center. Case #3 is shown at the time step where the laser is turned off while cases #2, #5 and #6 are shown at the last time steps before the melt pool separation. In all four cases we find melt aggregation and a disturbed track topology in the region of initial melt pool development. At the onset of a single melt track the pool is more likely to accumulate, as shown in [1,25], even when there is no powder bed present [36]. We believe this enhanced accumulation facilitates balling. Therefore, we disregard initial humps and focus the validation on the subsequent melt track. The topologies of cases #2 and #5 remain homogeneous for the most part and only a marginal amount of melt separates in case #2, see Fig. 3 (a) and (b). In contrast, large melt agglomerates separate from the main pool in cases #3 and #6, see Fig. 3 (c) and (d). The developing balls extend over the powder layer height. Thus, the increased likelihood of balling for cases #3 and #6 as found in the experiments is confirmed by the simulations. Besides the indication of balling and non-balling conditions, the results reveal an increased tendency of melt separation, inhomogeneous track topology and disturbed melt pool at higher laser scan speeds and a lower laser power.

Table 2
Single melt track dimensions.

Serial number	Width l_w [μm]	Depth [μm]	Width [μm] [38]	Depth [μm] [38]
1	129	115		100 ± 7
2	119	115		100 ± 9
3	114	52		
4	148	154	150 ± 7.5	
5	136	145		
6	129	74		
7	155	167	150 ± 7.5	

3.3. Balling mechanism

The simulations allow for a precise determination of melt pool ratios and to quantify forces relevant for the cause and development of balling. In Fig. 4 and Fig. 5 the melt pool evolution for cases #3 and #6 are shown in top view and as centered cut section, respectively. We distinguish four regions of the melt pool: (I) depression,

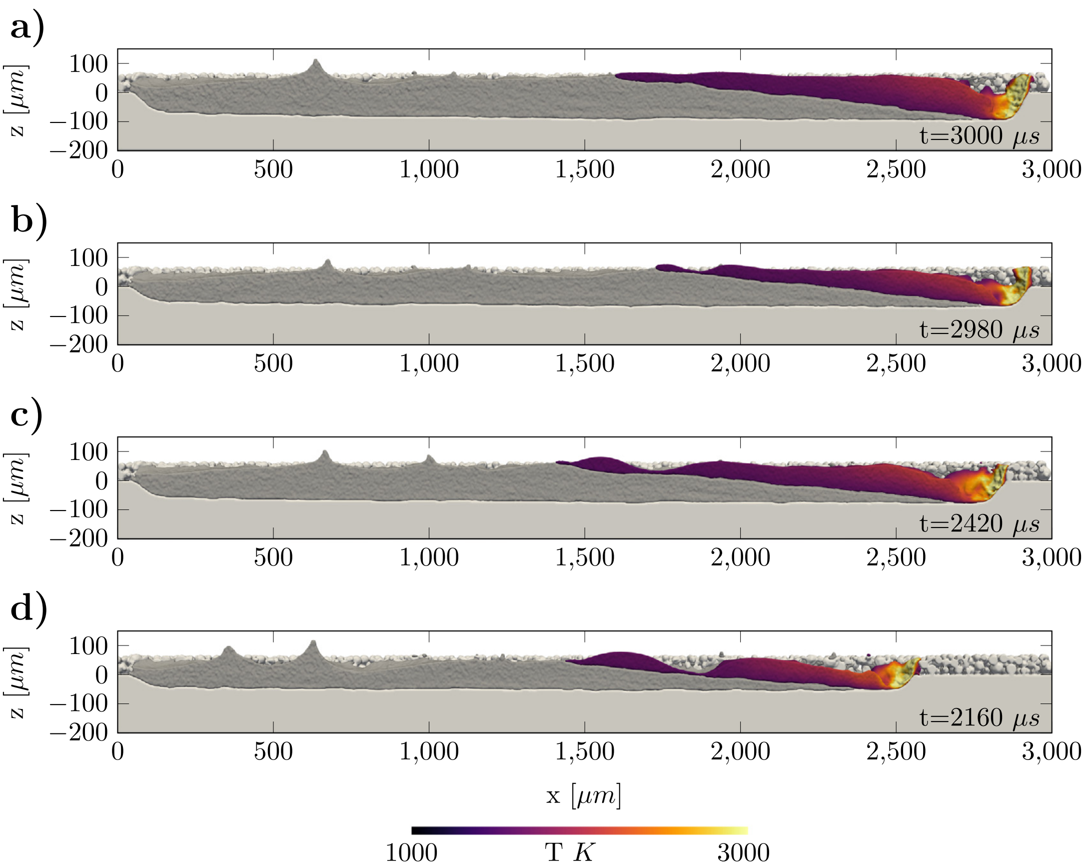

Fig. 3. Longitudinal cross section view of single melt tracks at the last time step before pinch-off for process parameter set (a) #3, (b) #2, (c) #5 and (d) #6.

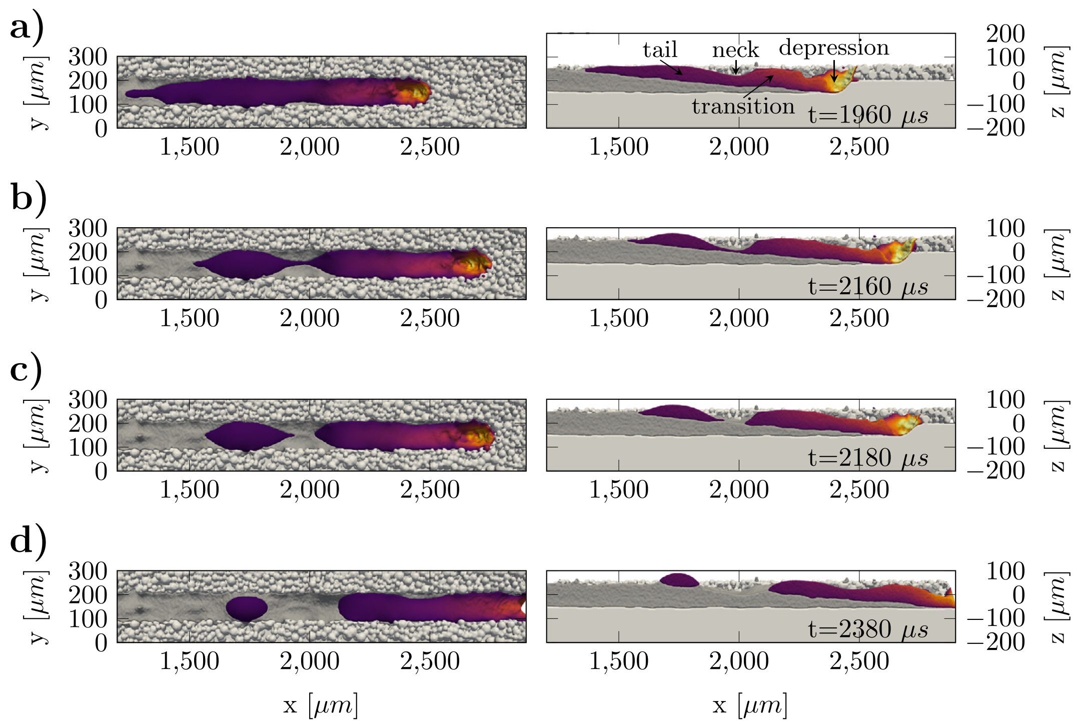

Fig. 4. Top view and longitudinal cross section view of balling process for simulation case #3 at (a) $t = 1960$ μs, (b) $t = 2160$ μs, (c) $t = 2180$ μs and (d) $t = 2380$ μs.

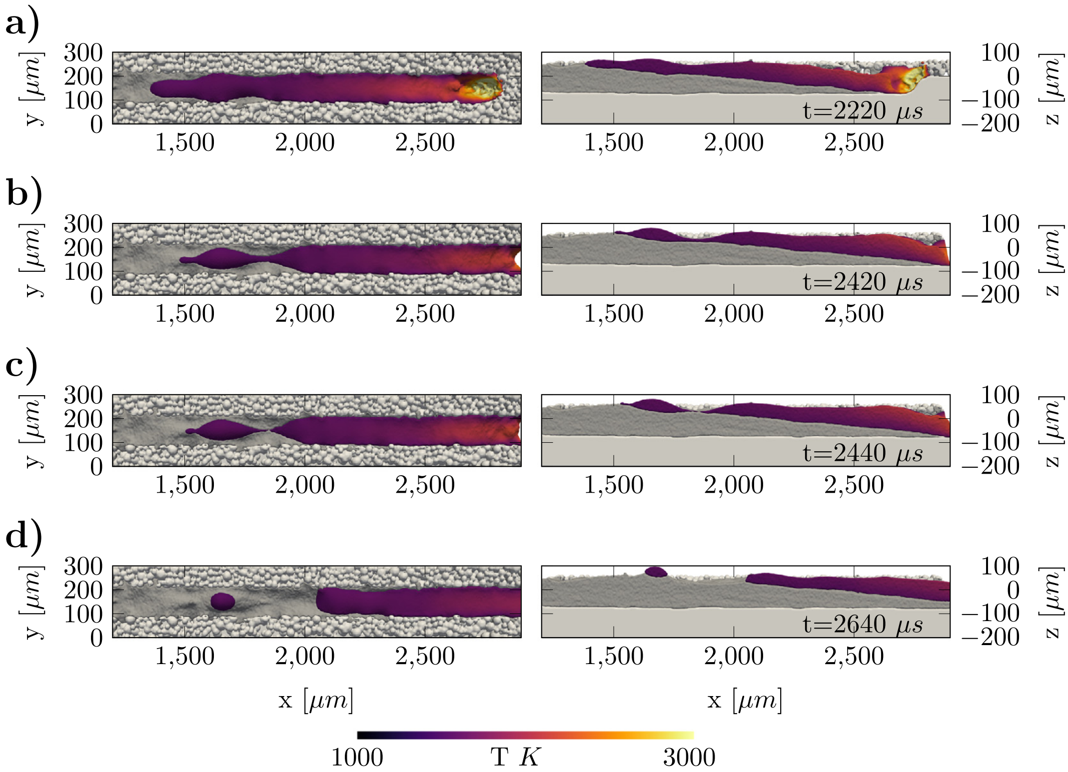

Fig. 5. Top view and longitudinal cross section view of balling process for simulation case #6 at (a) $t = 2220$ μs, (b) $t = 2420$ μs, (c) $t = 2440$ μs and (d) $t = 2640$ μs.

(II) transition, (III) neck, and (IV) tail end. In direct proximity of the laser beam strong recoil pressure and Marangoni forces induce a depression of the melt pool. Further downstream the transition region follows, characterized by decay of the high temperature gradients, the absence of prominent melt extrusion and a constant melt pool width. The section with contracting melt pool post laser-exposure is called the neck-region. The following tail end region eventually forms the isolated ball. Both the depression and transition region appear quasi-steady while the neck and tail region vary periodically to form the emerging balls. The depression constitutes the deepest penetration into the substrate. It is followed by a gradual decrease of melt pool depth in the transition region. The contraction of melt at the tail end leads to a hemispherical shape which exceeds the powder layer height. In contrast, layer build-up in the neck region is marginal. As a result, the solidified track topology consists of a ball followed by a cavity. Note, while the melt pool size of case #6 exceeds the one of case #3 the ball size is smaller in case #6. The ball size depends on the onset of necking. In case #3 necking starts further upstream, leading to a larger tail region and eventually a larger ball. Consequently, the cavity following the ball is more pronounced in case #3 as well.

Melt pool breakup shown in Fig. 4 and Fig. 5 exhibits characteristics of Plateau–Rayleigh instability. A common parameter to evaluate this instability in melt pools is the length to width ratio [7,21]. The length to width threshold ratios found in literature range between 2 and π [13]. A clear indication as to which analytical model is most precise still is missing and their overall applicability is questioned [31]. On the one hand, for process conditions of low melt penetration numerical studies from literature show melt breakup prior to the predicted ratios [10]. On the other hand, the stabilizing effect of melt penetration into the substrate is discarded completely in the analytical models suggesting an underestimation of the breakup ratios [7]. The resulting length to width ratios for cases #3 and #6 are 11.3 and 11.4, respectively. While these ratios agree with the available models they cannot confirm their accuracy as they are well beyond the model thresholds. Large length to width ratios for cases #2 and #5 indicate stable melt tracks beyond the analytical model predictions. This discrepancy most likely originates from the stabilization due to a considerate melt penetration which is discarded in the analytical models. Nonetheless, the present simulation results confirm the trend of long, shallow and narrow melt pools to be less stable.

Now, we take a closer look at the influence of Marangoni and capillary forces on the necking and breakup behavior. In this work, a linear surface-tension dependence on temperature is incorporated, see σ in A.3. Its impact on the melt pool is twofold. First, the capillary forces normal to the interfaces reduce with temperature. And more importantly, tangential Marangoni forces occur as a result of non-zero surface tension gradients along the interface. In Fig. 6 (b) and (c), case #3 is shown shortly after the onset of necking at time 1960 μs, as well as shortly before the pinch-off at time 2160 μs. The melt pool is color coded with the temperature. The lines 1 - 4 and 1' - 4' correspond to the transverse surface tension plots in Fig. 6 (a). In Fig. 6 (d) the surface tension along lines A and B is shown. The highest heat content and surface-tension gradients are found in the depression region. Downstream, high temperatures at the melt pool center lead to a low surface-tension that rapidly increases towards the cooler melt pool edges. In the transition region the surface tension at the melt pool sides remains constant while it increases along the center. As the Marangoni force results from the surface-tension gradient, their intensity can be estimated from the slope of the surface tension plots. It is concluded that a strong Marangoni force only is present in the depression region and quickly decreases in the transition region. Since surface-tension gradients decay over time, the Marangoni force attenuates as well. Shortly before ball pinch-off, only a weak Marangoni force acts in the neck region. Consequently, the Marangoni force, which promotes melt spreading, decays as necking progresses.

To investigate the impact of capillary forces, we study the evolution of pressure in the neck region over time. Fig. 7 (a) shows the pressure contour of case #3 at times 1960, 2080 and 2140 μs in a cut through the melt pool center. Color coding corresponds to the normalized pressure field. The white x-marked line through the neck region indicates the

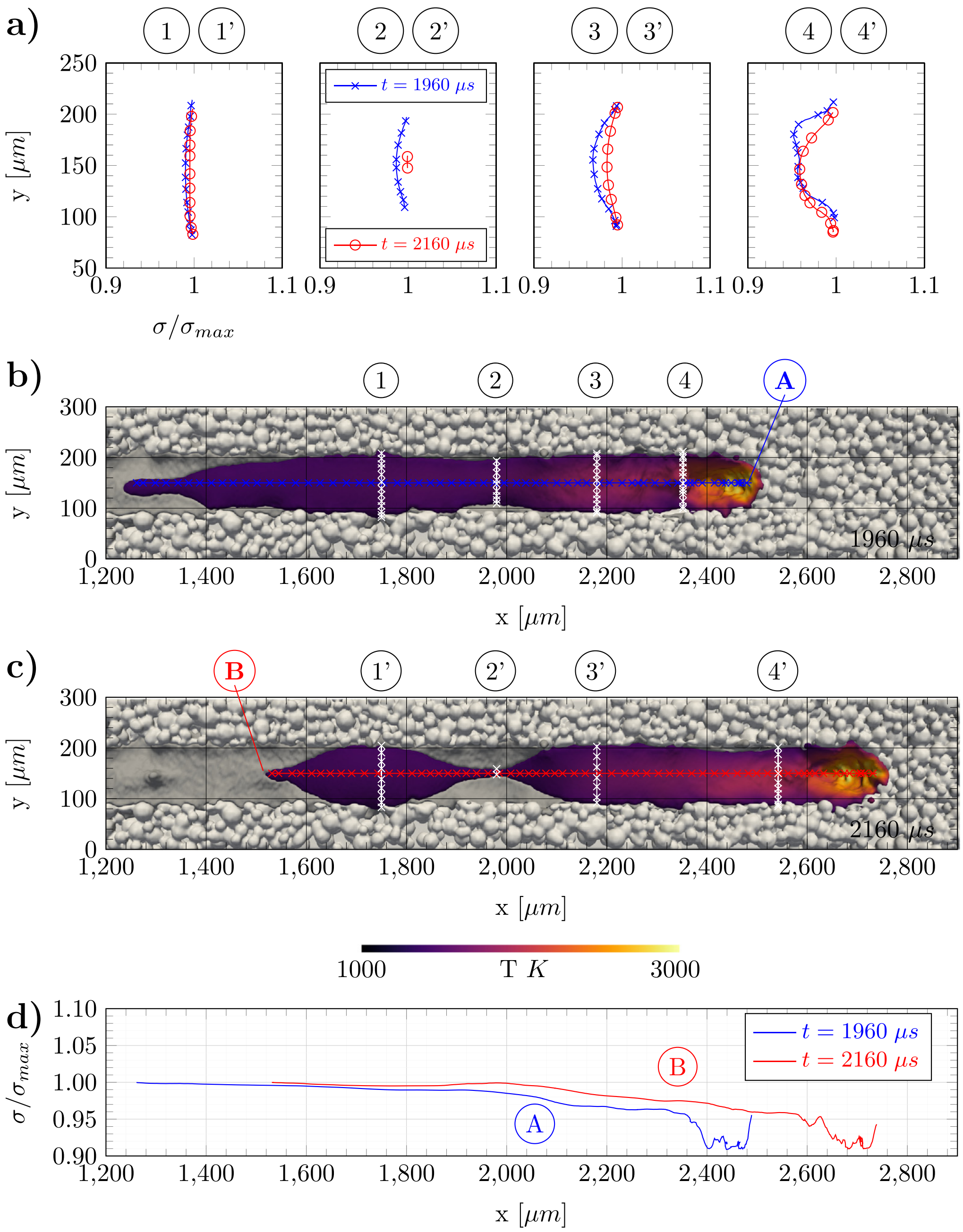

Fig. 6. Surface tension distribution for simulation #3 at time 1960 μs and 2160 μs (a) transverse at locations x = 1750 μm, x = 1980 μm, x = 2180 μm and x = 2352 μm, (b) temperature contour plot shortly after necking onset, (c) temperature contour plot shortly before pinch-off and (d) longitudinal along the melt pool surface.

path of the pressure plot in Fig. 7 (b). As the neck contracts, pressure increases. This is a direct response to a stronger capillary force. As a result, strong pressure gradients arise towards the transition and tail end region. These pressure gradients in turn induce a convective flux outward of the neck region. To quantify the impact of melt convection on the neck contraction and balling, the average specific momentum $I_{sp} = \sum(m_i v_i)/\sum(m_i)$ is plotted over time in Fig. 7 (c), with particle mass m_i and particle velocity v_i. I_{sp} is evaluated in the downstream and upstream neck regions $x = 1750 - 1980$ μm and $x = 1980 - 2180$ μm, respectively. Shortly before breakup, melt convects towards the neck region. Then, as the pressure in the neck rises, momentum changes direction, and following breakup melt convects outwards from the neck region. Capillary force leads to a pressure increase in the neck that induces melt convection, which induces further necking and ultimately to melt pool breakup.

The melt pool breakup is followed by a melt contraction towards a ball. One common explanation of the balling process is the competing mechanisms of solidification and spreading [8,33,34]. From the assumption of no impact speed of the melted material it is concluded that melt flow is mainly driven by capillary forces and inertia. A comparison of the time scale of super-heat removal to the spreading time is then used to predict the presence or absence of balling. Faster solidification than spreading timescales are claimed to lead to a premature stop of spreading and thus induce balling. In accordance to [33], the solidification time in the present study is approximated by $\tau^{sol} = 2\left(w^2/3\alpha\right)\ln\left(T_0 - T_\infty\right)/\left(T_s - T_\infty\right)$. For cases #3 and #6 follow solidification times of 51 μs and 42 μs. Here, melt track widths of w = 110 μm and w = 127 μm, thermal diffusivities of $\alpha = 6.78e^{-6}$ m^2/s and $\alpha = 7.43e^{-6}$ m^2/s, super heat temperatures T_0 = 1579 K and T_0 = 1563 K, an ambient temperature of T_∞ = 353 K and solidus temperature of

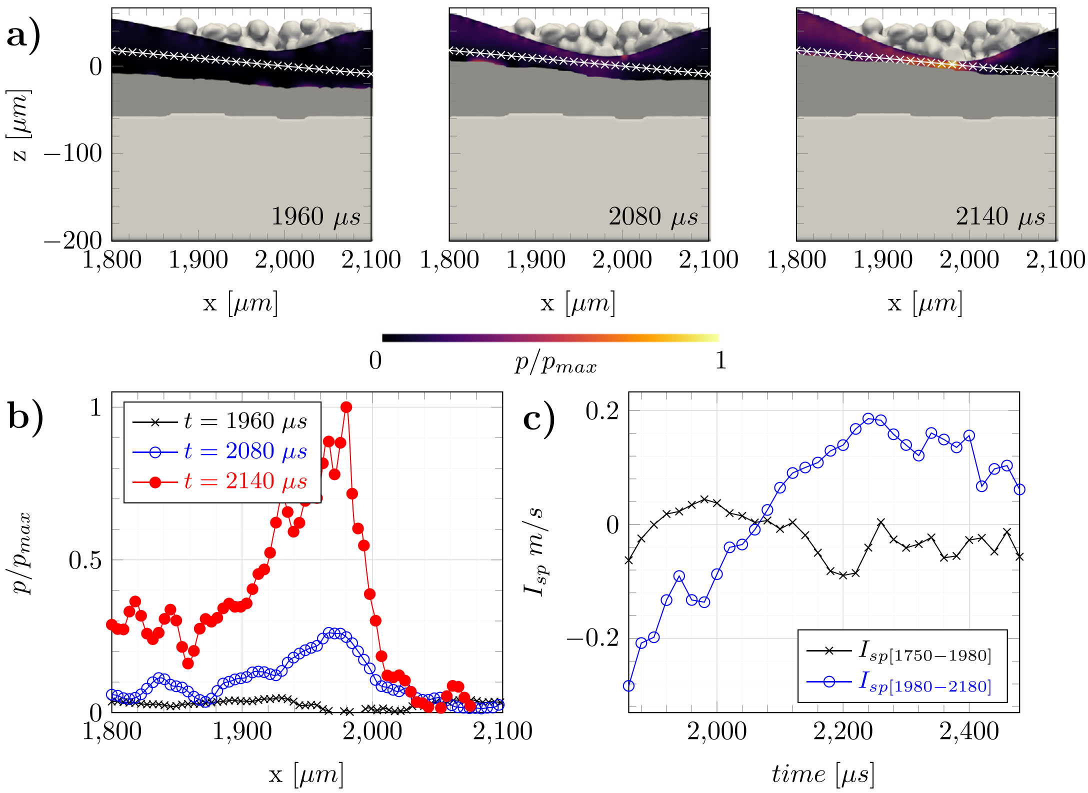

Fig. 7. Longitudinal center cross section in neck region between x = 1800 μm and x = 2100 μm (a) pressure contour plot at time t = 1960 μs, t = 2080 μs and t = 2140 μs, (b) normalized pressure distribution through neck and (c) specific momentum in upstream and downstream neck region over time.

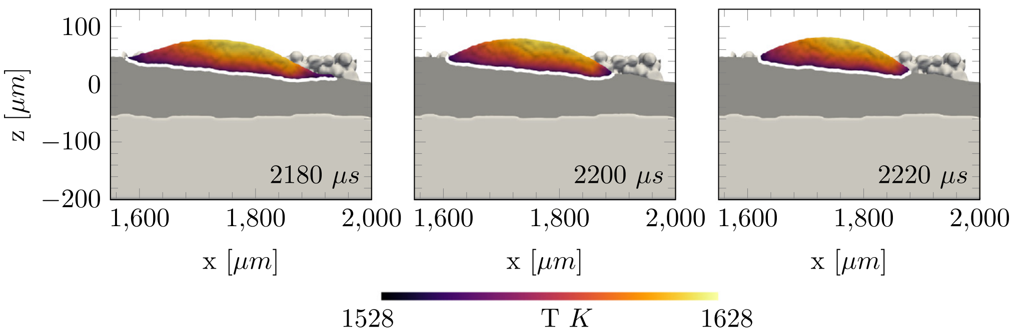

Fig. 8. Balling process of case #3 at time t = 2180 μs, t = 2200 μs and t = 2220 μs. Solidification front in white, solidified material in dark gray, substrate in light gray, and melt pool temperature color coded. (For interpretation of the references to color in this figure legend, the reader is referred to the web version of this article.)

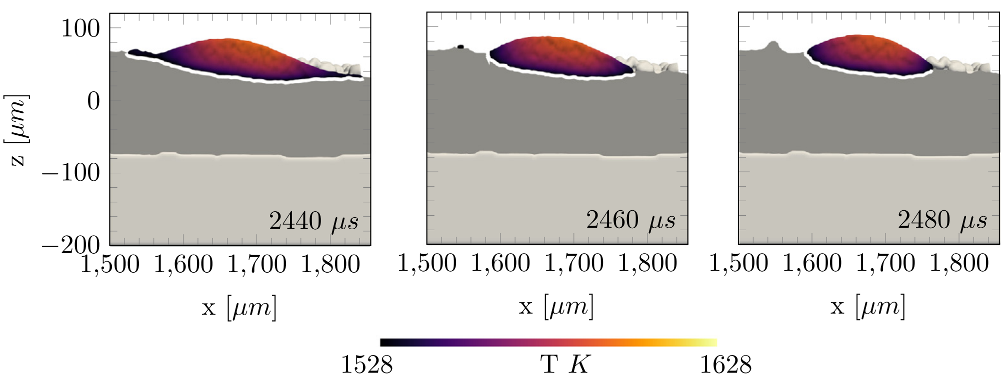

Fig. 9. Balling process of case #6 at time t = 2440 μs, t = 2460 μs and t = 2480 μs. Solidification front in white, solidified material in dark gray, substrate in light gray, and melt pool temperature color coded. (For interpretation of the references to color in this figure legend, the reader is referred to the web version of this article.)

Table A.3
Material properties Inconel 718 [43].

Notation	Property		Value	Units
T_s	Solidus temperature	–	1528	K
T_l	Liquidus temperature	–	1610	K
T_{ev}	Boiling temperature	–	3104	K
ρ_0	Density	–	7733	kg/m^3
ν	Dynamic viscosity	$T_s \leq T$	$0.179\ e^{-2}\exp(50.2/(R\ T))$	Pa s
σ	Surface tension coefficient	$T_s \leq T$	$2.1049\ e^{-3}$–$0.11e^{-3}\ K^{-1}$T	N/m
λ	Thermal conductivity	$T \leq T_s$ $T_s \leq T \leq T_l$ $T_l \leq T$	5.884 + 0.01654 K^{-1}T 111.454–0.05255 K^{-1}T 4.952 + 0.01360 K^{-1} T	W/mK
c_p	Specific heat capacity	0 ≤ h < 36367.7 36367.7 ≤ h < 332707.7 332707.7 ≤ h < 676972 676972 ≤ h < 968765 968765 ≤ h < 2131058	334.4 h /(h+97351.8) 493.9 h /(h+161192.3) 652 h /(h+319284) 3558 h /(h+4759615) 778 h /(h+283854)	J/kg K
ρ_{el}	Electrical resistivity	T ≤ 1123 K 1123 K < T ≤ T_s T_s < T ≤ T_l T_l < T	$1.105e^{-6}+2.617e^{-10}\ K^{-1}$ T $1.341e^{-6}+5.182e^{-11}\ K^{-1}$ T $4.511e^{-6}+6.341e^{-10}\ K^{-1}$ T $1.260e^{-6}+1.317e^{-10}\ K^{-1}$ T	Ω m
α	Absorptivity	T	$0.365\ \sqrt{\rho_{el}/\lambda}$ - $0.0667\ \rho_{el}/\lambda + 0.006\ \sqrt{(\rho_{el}/\lambda)^3}$	–
$h_{ev,n}$	Latent heat of evaporation	–	$6.583e^6$	J/kg
h_{ev}	Molar heat of evaporation	–	$382e^3$	J/mol
M	Molar mass	–	$57.96e^{-3}$	kg/mol

T_s = 1528 K are applied, respectively. From $\tau^{spread} = (\rho w^3/\sigma)^{0.5}$, the spreading timescales 74 µs and 92 µs follow for cases #3 and #6. Here, density ρ = 7733 kg/m^3 and surface tension coefficients σ = 1.89 N/m are used in both cases. The applied material variables are the average values determined in the ball at pinch-off. At that time, most of the melt super-heat is already removed and the tail end spreading is already stopped. As the evaluated spreading time exceeds the solidification time, no melt spreading is expected in both cases.

Overall, the simulation results support the theoretical model. It is interesting to note, that in contrast to the model assumption of zero impact speed, the melt has considerable non-zero momentum after pinch-off, see Fig. 7 (c). In Figs. 8 and 9 the tail end region of cases #3 and #6 and their respective solidification fronts are shown shortly after the melt pool breakup. The melt pool is color coded by temperature. In both cases we find a contracting melt pool rather than a flow dominated by spreading forces. In case #3 the melt contracts from time t = 2180 µs to time t = 2200 µs at which point the solidification front is caught up. The same behavior is found in case #6 where melt contraction and solidification define the balling process. We conclude that, when balling occurs following a necking process, the assumption of zero impact speed of the model by [33] no longer is valid. Instead, the balling process is best characterized by an advancing solidification front at the rear of the tail region and melt contraction followed by an advancing solidification at the front of the tail region.

4. Conclusions

Single melt track simulations are conducted at seven scan-speed-laser-power settings to investigate balling behavior of Inconel 718 material. The present smoothed particle hydrodynamics model accurately predicts multi-phase dynamics including strong interface deformations. The numerical model considers all relevant thermal- and fluid-mechanics effects, including evaporation-induced recoil pressure and cooling as well as capillary, Marangoni and wetting interface forces.

The validity of the model to investigate the balling phenomenon is established by comparison with experimental data. As the breakup is very sensitive to the apparent melt pool dimensions, we compare width and depth with [38] and find good agreement. In addition, the model capability to predict parameter sets for balling and non-balling melt tracks is validated for two power settings. We identify clearly absence and presence of balls as well as rough and smooth melt pool topologies at the respective conditions.

An investigation of the surface-tension distribution in transversal and longitudinal scan direction reveals the connection of Marangoni forces to the melt pool dynamics. Particular important to the balling process is the decay of surface tension gradients in the necking region during the melt contraction. It indicates a related decay of stabilizing melt flow towards the pool edges.

In contrast, capillary forces within the neck increase as necking progresses both due to an increase of curvature and a reduction in temperature. A resulting high capillary pressure induces a convective melt flux away from the neck region, ultimately leading to the pinch-off of the tail region. As a result, material build-up within the neck area is marginal. Analytical estimates for breakup conditions cannot be confirmed by the numerical results as the melt pool shows to be stable well beyond the model thresholds. This deviation can be explained by stabilizing melt pool penetration into the substrate, which is disregarded by the analytical estimates. We find a comparable breakup behavior for both investigated power settings. The ball size shows to depend more on the necking onset rather than the size of the melt pool itself.

The balling process is best characterized by an advancing solidification front at the rear, and an initial melt contraction at the front that is followed by an advancing melt front at a later stage. Thus, from the simulations the common explanation of the competing mechanisms of spreading and solidification cannot be confirmed. Instead, we find that capillary forces in the neck region induce a melt contraction which is stronger than melt spreading.

CRediT authorship contribution statement

C. Zöller: Conceptualization, Data curation, Formal analysis, Investigation, Methodology, Software, Validation, Visualization, Writing – original draft, Writing – review & editing. **N.A. Adams:** Funding acquisition, Project administration, Resources, Writing – review & editing. **S. Adami:** Conceptualization, Formal analysis, Investigation, Methodology, Software, Supervision, Writing – review & editing.

Declaration of competing interest

The authors declare that they have no known competing financial interests or personal relationships that could have appeared to influence the work reported in this paper.

Data availability

Data will be made available on request.

Acknowledgments

Nikolaus Adams and Stefan Adami gratefully acknowledge funding through the TUM-Oerlikon Advanced Manufacturing Institute, Germany. In addition, computing time was provided by the Gauss Centre for Supercomputing e.V. (www.gauss-centre.eu) at the Leibniz Supercomputing Centre (www.lrz.de), which is greatly appreciated.

Appendix

See Table A.3.

References

[1] W. Ge, S. Han, Y. Fang, J. Cheon, S.J. Na, Mechanism of surface morphology in electron beam melting of Ti6Al4V based on computational flow patterns, Appl. Surf. Sci. 419 (2017) 150–158.
[2] R.P. Parida, V. Senthilkumar, Experimental studies of defect generation in selective laser melted Inconel 718 alloy, Proc. - Mater. Today 39 (2021) 1372–1377.
[3] L. Moniz, Q. Chen, G. Guillemot, M. Bellet, C.-A. Gandin, C. Colin, J.-D. Bartout, M.-H. Berger, Additive manufacturing of an oxide ceramic by laser beam melting—Comparison between finite element simulation and experimental results, J. Mater Process. Technol. 270 (2019) 106–117.
[4] S. Yuan, F. Shen, C.K. Chua, K. Zhou, Polymeric composites for powder-based additive manufacturing: Materials and applications, Prog. Polym. Sci. 91 (2019) 141–168.
[5] P. Yuan, D. Gu, Molten pool behaviour and its physical mechanism during selective laser melting of TiC/AlSi10Mg nanocomposites: Simulation and experiments, J. Phys. D: Appl. Phys. 48 (3) (2015) 035303–035319.
[6] D. Dai, D. Gu, Influence of thermodynamics within molten pool on migration and distribution state of reinforcement during selective laser melting of AlN/AlSi10Mg composites, Int. J. Mach. Tools Manuf. 100 (2016) 14–24.
[7] I. Yadroitsev, A. Gusarov, I. Yadroitsava, I. Smurov, Single track formation in selective laser melting of metal powders, J. Mater Process. Technol. 210 (12) (2010) 1624–1631.
[8] C. Guo, Z. Xu, Y. Zhou, S. Shi, G. Li, H. Lu, Q. Zhu, R.M. Ward, Single-track investigation of IN738LC superalloy fabricated by laser powder bed fusion: Track morphology, bead characteristics and part quality, J. Mater Process. Technol. 290 (2021) 117000–117015.
[9] W. Yan, W. Ge, Y. Qian, S. Lin, B. Zhou, W.K. Liu, F. Lin, G.J. Wagner, Multi-physics modeling of single/multiple-track defect mechanisms in electron beam selective melting, Acta Mater. 134 (2017) 324–333.
[10] Y. Lee, W. Zhang, Mesoscopic simulation of heat transfer and fluid flow in laser powder bed additive manufacturing, in: Proceedings - 26th Annual International Solid Freeform Fabrication Symposium - An Additive Manufacturing Conference, SFF 2015, 2020, pp. 1154–1165.
[11] U. Gratzke, P. Kapadia, J. Dowden, J. Kroos, G. Simon, Theoretical approach to the humping phenomenon in welding processes, J. Phys. D: Appl. Phys. 25 (11) (1992) 1640–1647.
[12] J. Liu, D.-d. Gu, H.-y. Chen, D.-h. Dai, H. Zhang, Influence of substrate surface morphology on wetting behavior of tracks during selective laser melting of aluminum-based alloys, J. Zhejiang Univ.-Sci. A 19 (2) (2018) 111–121.
[13] L. Johnson, M. Mahmoudi, B. Zhang, R. Seede, X. Huang, J.T. Maier, H.J. Maier, I. Karaman, A. Elwany, R. Arróyave, Assessing printability maps in additive manufacturing of metal alloys, Acta Mater. 176 (2019) 199–210.
[14] R. Li, J. Liu, Y. Shi, L. Wang, W. Jiang, Balling behavior of stainless steel and nickel powder during selective laser melting process, Int. J. Adv. Manuf. Technol. 59 (9) (2012) 1025–1035.
[15] H. Niu, I. Chang, Instability of scan tracks of selective laser sintering of high speed steel powder, Scr. Mater. 41 (11) (1999) 1229–1234.
[16] G. Yu, D. Gu, D. Dai, M. Xia, C. Ma, Q. Shi, On the role of processing parameters in thermal behavior, surface morphology and accuracy during laser 3D printing of aluminum alloy, J. Phys. D: Appl. Phys. 49 (13) (2016) 135501–135516.
[17] L. Li, J.-Q. Li, T.-H. Fan, Phase-field modeling of wetting and balling dynamics in powder bed fusion process, Phys. Fluids 33 (4) (2021) 042116–042126.
[18] D. Gu, P. Yuan, Thermal evolution behavior and fluid dynamics during laser additive manufacturing of Al-based nanocomposites: Underlying role of reinforcement weight fraction, J. Appl. Phys. 118 (23) (2015) 233109–233119.
[19] C. Körner, E. Attar, P. Heinl, Mesoscopic simulation of selective beam melting processes, J. Mater Process. Technol. 211 (6) (2011) 978–987.
[20] D. Gu, Y. Shen, Balling phenomena in direct laser sintering of stainless steel powder: Metallurgical mechanisms and control methods, Mater. Des. 30 (8) (2009) 2903–2910.
[21] J.-P. Kruth, L. Froyen, J. Van Vaerenbergh, P. Mercelis, M. Rombouts, B. Lauwers, Selective laser melting of iron-based powder, J. Mater Process. Technol. 149 (1–3) (2004) 616–622.
[22] Z. Ren, D.Z. Zhang, G. Fu, J. Jiang, M. Zhao, High-fidelity modelling of selective laser melting copper alloy: Laser reflection behavior and thermal-fluid dynamics, Mater. Des. 207 (2021) 109857–109872.
[23] D. Gu, M. Xia, D. Dai, On the role of powder flow behavior in fluid thermodynamics and laser processability of Ni-based composites by selective laser melting, Int. J. Mach. Tools Manuf. 137 (2019) 67–78.
[24] A. Gusarov, I. Yadroitsev, P. Bertrand, I. Smurov, Heat transfer modelling and stability analysis of selective laser melting, Appl. Surf. Sci. 254 (4) (2007) 975–979.
[25] E. Papazoglou, N. Karkalos, A. Markopoulos, A comprehensive study on thermal modeling of SLM process under conduction mode using FEM, Int. J. Adv. Manuf. Technol. 111 (9) (2020) 2939–2955.
[26] S.A. Khairallah, A.T. Anderson, A. Rubenchik, W.E. King, Laser powder-bed fusion additive manufacturing: Physics of complex melt flow and formation mechanisms of pores, spatter, and denudation zones, Acta Mater. 108 (2016) 36–45.
[27] B. Bradstreet, Effect of surface tension and metal flow on weld bead formation, Weld. J. 47 (7) (1968) 314–322.
[28] H. Yang, Z. Li, S. Wang, The analytical prediction of thermal distribution and defect generation of Inconel 718 by selective laser melting, Appl. Sci. 10 (20) (2020) 7300–7319.
[29] S.A. Khairallah, A. Anderson, Mesoscopic simulation model of selective laser melting of stainless steel powder, J. Mater Process. Technol. 214 (11) (2014) 2627–2636.
[30] M. Khan, P. Dickens, Selective laser melting (SLM) of pure gold, Gold Bull. 43 (2) (2010) 114–121.
[31] A. Mostafaei, C. Zhao, Y. He, S. Reza Ghiaasiaan, B. Shi, S. Shao, N. Shamsaei, Z. Wu, N. Kouraytem, T. Sun, J. Pauza, J.V. Gordon, B. Webler, N.D. Parab, M. Asherloo, Q. Guo, L. Chen, A.D. Rollett, Defects and anomalies in powder bed fusion metal additive manufacturing, Curr. Opin. Solid State Mater. Sci. 26 (2) (2022) 100974–101098.
[32] Z. Li, B.-Q. Li, P. Bai, B. Liu, Y. Wang, Research on the thermal behaviour of a selectively laser melted aluminium alloy: Simulation and experiment, Materials 11 (7) (2018) 1172–1186.
[33] X. Zhou, X. Liu, D. Zhang, Z. Shen, W. Liu, Balling phenomena in selective laser melted tungsten, J. Mater Process. Technol. 222 (2015) 33–42.
[34] S. Liu, H. Guo, Balling behavior of selective laser melting SLM magnesium alloy, Materials 13 (16) (2020) 3632–3653.
[35] M. Boutaous, X. Liu, D.A. Siginer, S. Xin, Balling phenomenon in metallic laser based 3D printing process, Int. J. Therm. Sci. 167 (2021) 107011–107021.
[36] W. Ge, S. Han, S.J. Na, J.Y.H. Fuh, Numerical modelling of surface morphology in selective laser melting, Comput. Mater. Sci. 186 (2021) 110062–110070.
[37] H. Gu, C. Wei, L. Li, Q. Han, R. Setchi, M. Ryan, Q. Li, Multi-physics modelling of molten pool development and track formation in multi-track, multi-layer and multi-material selective laser melting, Int. J. Heat Mass Transfer 151 (2020) 119458–119474.
[38] L. Scime, J. Beuth, Melt pool geometry and morphology variability for the Inconel 718 alloy in a laser powder bed fusion additive manufacturing process, Addit. Manuf. 29 (2019) 100830–100839.
[39] M. Liu, G. Liu, Smoothed Particle Hydrodynamics (SPH): An overview and recent developments, Arch. Comput. Methods Eng. 17 (1) (2010) 25–76.
[40] X. Hu, N. Adams, A multi-phase SPH method for macroscopic and mesoscopic flows, J. Comput. Phys. 213 (2) (2006) 844–861.
[41] S. Adami, X. Hu, N.A. Adams, A transport-velocity formulation for smoothed particle hydrodynamics, J. Comput. Phys. 241 (2013) 292–307.
[42] S. Adami, X.Y. Hu, N.A. Adams, A generalized wall boundary condition for smoothed particle hydrodynamics, J. Comput. Phys. 231 (21) (2012) 7057–7075.
[43] J. Weirather, V. Rozov, M. Wille, P. Schuler, C. Seidel, N.A. Adams, M.F. Zaeh, A smoothed particle hydrodynamics model for laser beam melting of Ni-based alloy 718, Comput. Math. Appl. 78 (7) (2019) 2377–2394.
[44] C. Zöller, N. Adams, S. Adami, A partitioned continuous surface stress model for multiphase smoothed particle hydrodynamics, J. Comput. Phys. 472 (2023) 111716.
[45] C. Li, Y. Guo, J. Zhao, Interfacial phenomena and characteristics between the deposited material and substrate in selective laser melting Inconel 625, J. Mater Process. Technol. 243 (2017) 269–281.
[46] P.W. Cleary, J.J. Monaghan, Conduction modelling using smoothed particle hydrodynamics, J. Comput. Phys. 148 (1) (1999) 227–264.

[47] X. He, P. Fuerschbach, T. DebRoy, Heat transfer and fluid flow during laser spot welding of 304 stainless steel, J. Phys. D: Appl. Phys. 36 (12) (2003) 1388–1398.
[48] J.-P. Fürstenau, H. Wessels, C. Weißenfels, P. Wriggers, Generating virtual process maps of SLM using powder-scale SPH simulations, Comput. Part. Mech. 7 (4) (2020) 655–677.
[49] S.I. Anisimov, V.A. Khokhlov, Instabilities in Laser-Matter Interaction, CRC Press, 1995.
[50] C. Schlick, An inexpensive BRDF model for physically-based rendering, Comput. Graph. Forum 13 (1994) 233–246.
[51] R.H. Cole, R. Weller, Underwater explosions, Phys. Today 1 (6) (1948) 35.
[52] W.C. Swope, H.C. Andersen, P.H. Berens, K.R. Wilson, A computer simulation method for the calculation of equilibrium constants for the formation of physical clusters of molecules: Application to small water clusters, J. Chem. Phys. 76 (1) (1982) 637–649.
[53] J.J. Monaghan, Smoothed particle hydrodynamics, Annu. Rev. Astron. Astrophys. 30 (1) (1992) 543–574.
[54] J.P. Morris, A study of the stability properties of smooth particle hydrodynamics, Publ. Astron. Soc. Aust. 13 (1996) 97–102.
[55] J. Zhou, Y. Zhang, J. Chen, Numerical simulation of random packing of spherical particles for powder-based additive manufacturing, J. Manuf. Sci. Eng. 131 (3) (2009) 031004–031012.
[56] P. Incardona, A. Leo, Y. Zaluzhnyi, R. Ramaswamy, I.F. Sbalzarini, OpenFPM: A scalable open framework for particle and particle-mesh codes on parallel computers, Comput. Phys. Comm. 241 (2019) 155–177.

Appendix C

Beam-shaping in laser-based powder bed fusion of metals: A computational analysis of point-ring intensity profiles

Additive Manufacturing 93 (2024) 104402

Contents lists available at ScienceDirect

Additive Manufacturing

journal homepage: www.elsevier.com/locate/addma

Research paper

Beam-shaping in laser-based powder bed fusion of metals: A computational analysis of point-ring intensity profiles

C. Zöller [a,*], N.A. Adams [a,b], S. Adami [b]

[a] Technical University of Munich, TUM School of Engineering and Design, Chair of Aerodynamics and Fluid Mechanics, Boltzmannstraße 15, 85748 Garching, Germany

[b] Technical University of Munich, Munich Institute of Integrated Materials, Energy and Process Engineering, Lichtenbergstraße 4a, 85748 Garching, Germany

ARTICLE INFO

Keywords:
Smoothed Particle Hydrodynamics
SPH
Laser shape
Laser profile
Beam shape
Beam profile
Intensity distribution
Intensity profile
Power distribution
Energy distribution

ABSTRACT

Laser-based powder bed fusion has the potential to enable manufacturing of local material properties and locally varying alloys. One promising approach under research is shaping of the applied laser beam. The current commercial standard using a Gaussian laser beam profile is associated with a high energy intensity peak and strong gradients. A potential alternative beam shape is the point-ring profile where laser energy is distributed between a central spot and an outer ring. We conduct a numerical study of beam shape impact on melt-pool shapes, surface temperatures, evaporation and flow dynamics of single-melt-tracks. To that end, we apply a Weakly Compressible Smoothed Particle Hydrodynamics solver coupled with a ray-tracing laser scheme. A point-ring profile is compared to a standard Gaussian profile. The profiles are studied at two different beam sizes to find the influence of beam size on the shape effect. We find good agreement between numerical results and experimental data for both narrow and deep, as well as wide and shallow melt-tracks. The simulation results show that beam size and thus energy density influence the effect beam-shaping has on the melt-pool dynamics. Both the distribution of evaporation and surface tension forces over the melt-pool surface are found to depend on the used beam shape. The study highlights the importance of distinguishing between size and shape effects when investigating laser beam shapes. Both energy density and its distribution need to be tuned for the desired melt-pool behavior.

1. Introduction

While laser-based powder bed fusion is becoming an increasingly competitive manufacturing technique, it is still limited by process stability and efficiency. Typically, process windows of stable production are restricted in terms of scan speed and laser power due to fabrication defects such as porosity, rough surface finish, and micro cracks. Many defects are influenced by or even originate from the melt pool. One important parameter to control the melt-pool behavior is the laser energy input. The current industrial standard are Gaussian laser beams [1,2], exemplary shown in Fig. 1(a). Their beam shape is characterized by a high central intensity peak and a steep radial gradient. This intensity distribution can translate to overheating and high temperature gradients within the melt pool. The resulting evaporation and Marangoni flow lead to a highly dynamic melt pool [3]. Thus, the standard Gaussian beam profile contributes to melt-pool fluctuations, spatter, balling, and powder denudation [3]. As the Gaussian beam profile is found to attribute to a limited process window, alternative beam shapes are subject of current research [2]. In beam-shaping the beam profiles are adjusted to achieve melt-pool temperature distributions with favorable melt-pool dynamics [4] and solidification rates [5]. Common alternative laser beam shapes under investigation are the elliptical Gaussian profile [4–8], top-hat (flat-top) profile [9–11], doughnut profile (inverse Gaussian) [12,13], Bessel profile [14] and point-ring profile [3,15,16]. Their respective intensity distributions are schematically depicted in Fig. 1(b) to (f).

Abadi et al. [4] study the effect of longitudinal and transverse elliptical Gaussian beams on conduction mode welds. To that end, the reference Gaussian beam is increased in either the longitudinal or transverse direction, effectively reducing the applied power density. The numerical investigation shows reduced temperature gradients for the deformed beam shapes. A study of melt-pool flow dynamics reveals vertices at the front of the melt pool that attribute to material preheating in case of a longitudinal elliptical beam shape. In another investigation, the major and minor axis of the elliptical beams are chosen to deliver equivalent peak irradiances [6]. The results show an improvement of temperature gradients, maximum flow velocities and

* Corresponding author.
E-mail addresses: christopher.zoeller@tum.de (C. Zöller), nikolaus.adams@tum.de (N.A. Adams), stefan.adami@tum.de (S. Adami).

https://doi.org/10.1016/j.addma.2024.104402
Received 5 April 2024; Received in revised form 23 July 2024; Accepted 30 August 2024
Available online 2 September 2024

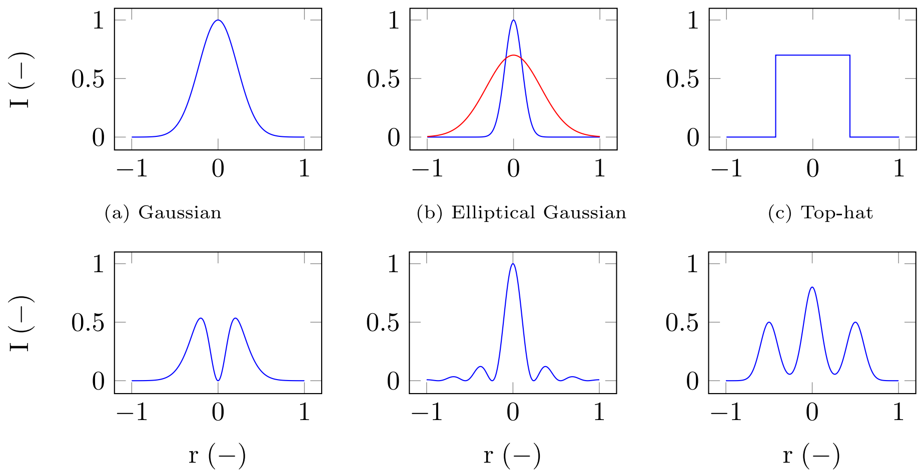

(a) Gaussian (b) Elliptical Gaussian (c) Top-hat

(d) Doughnut (e) Bessel (f) Point-Ring

Fig. 1. Schematic illustration of intensity distribution I over the radial distance r from the beam center for common beam profiles.

the key-hole free parameter space when elliptical shapes are applied. A comparison of single-melt-tracks shows, at approximately equivalent beam area, that elliptical shapes require higher energy densities to avoid lack of fusion [7]. In general, transverse elliptical beams result in shallow, short, and wide melt pools with a larger supercooled region [5]. Mi et al. [8] find, that the effect of elliptical beam shapes on melt-track dimensions depends on the scan speed, where differences in melt pool free surface contours are more pronounced at high scan speeds. As dimension and energy content can be adjusted by the use of elliptical beam shapes, they have the potential for tailored microstructure and thus part property generation. Roehling et al. [6] find, that elliptical beam shapes lead to the generation of equiaxed and mixed equiaxed-columnar microstructures over a wider range of process parameters than the Gaussian beam. This is also confirmed in a later study [7], where the volume fraction of equiaxed grains is increased by use of an elliptical beam shape. The specific development of the microstructure is further studied in a numerical investigation where an Arbitrarian Lagrangian Euler Method is coupled with the Cellular Automata method [5]. Microstructure development is shown to depend on melt-pool size and melt-pool curvature at the liquid solid interface. The resulting melt pool of single track scans with transverse elliptical Gaussian beams are found to be favorable for grain nucleation and equiaxed grain development.

In [9] Sow et al. compare a small Gaussian beam to a large top-hat beam. They show lower evaporation and suppression of spatter for the top-hat profile which is attributed to lower volumetric energy densities. The use of top-hat beam profiles also demonstrates to reduce the powder denudation zone and facilitate a more homogeneous bonding between the melt-pool tracks and the substrate [11]. An investigation of large top-hat laser beams finds larger width-to-depth ratios in the melt-pool compared to single track energy deposition by a small Gaussian beam. The induced melt pool is shown to be advantageous for epitaxial growth of columnar grains [10].

Wischeropp et al. [12] compare single-melt-track and density cube experiments conducted with a doughnut-shaped and a Gaussian laser beam of same spot diameter. The peak intensity of the doughnut beam shape is 42% below the Gaussian maximum. They show the doughnut beam shape produces wider and shallower melt-tracks. The differences are more pronounced at lower scan speeds. Even at high laser energies and high scan speeds, no key-holing and balling are observed for the doughnut shape leading to a significant increase of the process window. Two-dimensional numerical simulations with doughnut beam shapes show a more uniform intensity distribution in the melt and less evaporation losses compared to a Gaussian profile [17]. Simulation results by Grigoriev et al. [13] confirm less pronounced evaporation and the corresponding thermal losses when a doughnut profile with reduced peak intensity is applied.

With Bessel beams, narrower and deeper melt pools are achieved while temperature gradients are smaller compared to the Gaussian beam [18]. Final tracks show less defects and a reduced surface roughness. Tumkur et al. [14] apply the profile to single tracks of stainless steel 316 and find reduced thermal gradients, reduced spatter and an extended process window.

Between a Gaussian beam and a doughnut beam there exists a smooth transition of partial central spot and partial outer ring intensity distributions. Modern laser beam systems such as the AFX-1000 laser from nLight enable several modes of such intensity distribution spectra. It is important to note, that without further optical elements, a pure Gaussian-spot beam has a significantly smaller beam area and thus, at the same beam power, a much higher peak intensity compared to combined Gaussian and ring-shaped beams. The effect of three of those intensity distribution modes on high-strength aluminum alloys is investigated by Nahr et al. [3]. An increased processing window with greater processing speeds and laser powers compared to a Gaussian beam profile is found. The studied melt-tracks show less humping and surface roughness as well as reduced hot cracking with the alternative beam shapes. A study where the point-ring profiles are applied to powder bed fusion of 316L steel finds no key-holing and balling at significantly higher beam powers and scan speeds compared to Gaussian profiles allowing for faster build rates [15]. In [1], point-ring and Gaussian profiles of comparable and different sizes are used to study the beam shape influence on spatter behavior. Less spatter is recorded compared to a Gaussian beam when the adjusted profile is applied. Additionally, they find that peak intensity correlates with spatter size. A profile with an intensity distribution between point and ring of 1/4 is used to study the potential of beam-shaping for in-situ alloying [16]. The shaped profile proves capable to improve feed stock contamination as the amount of spatter can be reduced by almost 75%.

With the advancement of beam-shaping techniques even optimized shapes for target temperature distributions are possible [19]. Shapes also are no longer static but can be dynamically changed during the build process [20].

With improved melt-pool stability, an increased process window, less spatter, and variable micro structures, the investigations into shaped laser beams have revealed its potential for more stable, efficient and tailored powder-bed-fusion processes. Current research shows the importance of distinguishing between laser beam size and laser beam shape as both can have a significant effect on the process evolution. Yet, to the best of our knowledge, how beam size impacts the effects of beam shapes on melt-pool behavior has not been systematically investigated for point-ring profiles. In addition, no numerical studies are found which quantify influence factors and reveal the local flow field characteristics of melt pools forming under point-ring-shaped laser beam irradiation.

The aim of the present study is an in-depth investigation of laser beam shape effects on single-melt-tracks using point-ring shaped laser profiles. We apply a high-fidelity numerical scheme for single-melt-track simulations at the micro-scale. The isolated beam shape influence is studied by comparison of Gaussian and point-ring-shaped laser beam profiles at two different beam sizes. The simulation results are compared with regard to melt-track shape, temperature distribution on the melt-pool surface, material evaporation and flow field dynamics. Conclusions are drawn about the respective contributions of shape effects at different beam sizes. The manuscript is structured as follows. First, we briefly recap the applied simulation method highlighting the main physical and numerical modeling approaches. The methodology is validated by comparison with experimental data. Second, simulation results at fixed position and single-melt-tracks with different laser irradiation are presented and analyzed. Finally, we draw conclusions about beam shape effects on the melt-pool evolution.

2. Materials and methods

To study the influence of different beam shapes on the melt pool, we conduct transient, three-dimensional single melt-track simulations at the micro-scale. We apply a high-fidelity Weakly Compressible Smoothed Particle Hydrodynamics (WCSPH) model [21]. The Lagrangian particle method allows for a more natural treatment of the complex multi-phase problem compared to the commonly applied Eulerian grid-based approaches [22–24]. In Smoothed Particle Hydrodynamics, Lagrangian discretization elements are assigned to a certain phase. Neither their position in space nor their neighbor relations are fixed throughout the simulation. Instead, the particles can be understood as fluid elements that follow Newtons' laws of motion and carry mass, momentum and energy with them. Thus, the capturing and the tracking of phase interfaces is handled naturally. The method is therefore particularly suited for the intense melt-pool-interface dynamics during powder bed fusion. For a more detailed description of the SPH model the reader is referred to [21,25–29].

The validation data used in this study shows vastly different single-melt-track widths and depths in the parameter space under investigation. The experimental results suggest strong variations in evaporation and melt-pool dynamics depending on the applied beam shape [15]. To capture this versatile melt-pool behavior the three conservation laws of mass, momentum and energy are solved together with models for evaporation and surface tension effects. The set of equations is closed by Cole's weakly compressible equation of state [30]. The present model accounts for evaporation-induced melt convection through a recoil pressure force

$$\mathbf{F}^{ev} = \frac{1}{\rho} A\, c_1\, p_\infty \exp\left(\frac{\Delta H_{mol}}{R}\left(\frac{1}{T} - \frac{1}{T_{ev}}\right)\right), \tag{1}$$

derived from the Clausius–Clapeyron equation for ideal gases assuming a constant latent heat of phase change [31]. Here, the variables correspond to the evaporating surface area A, the coefficient $c_1 = 0.54$, the ambient pressure p_∞, the molar latent heat of evaporation ΔH_{mol}, the universal gas constant R, the temperature T and the boiling temperature T_{ev}, respectively.

Evaporative cooling follows

$$Q^{ev} = -A\ \left(h + h_{ev}\right) J_{ev}, \tag{2}$$

considering both the enthalpy h and the specific heat of evaporation h_{ev}. This heat sink acts at the interface between melt and ambient gas. The mass flux, J_{ev}, is approximated by

$$J_{ev} = c_2\, c_3\, p_r \sqrt{\frac{M}{2\pi R\, T}}, \tag{3}$$

where the coefficient $c_2 = 0.82$ and the sticking coefficient $c_3 = 1$ are chosen according to [31]. Here, p_r is the recoil pressure and M the atomic mass of the evaporating (melt-) material.

The influence of surface tension is considered threefold. At a curved melt-gas interface, the capillary force

$$\mathbf{F}^{\kappa} = \frac{1}{\rho}\sigma\kappa\mathbf{n}, \tag{4}$$

acts towards a minimization of surface free energy. The capillary force component is directed inwards, opposite to the interface normal direction $\mathbf{n}$, and its magnitude depends on the local curvature κ and the surface tension coefficient σ. Temperature gradients at the melt-pool surface induce a Marangoni force

$$\mathbf{F}^{\sigma} = \frac{1}{\rho}\nabla_s\sigma, \tag{5}$$

acting towards the cooler regions. Here, ∇_s is the surface-gradient operator. Finally, wetting forces at the melt-gas-substrate triple line conclude the description of surface tension effects on melt dynamics. Wetting is considered by solving Young's equation

$$\mathbf{F}^{\theta} = \frac{1}{\rho}\sigma\left(cos\left(\theta_{eq}\right) - cos\left(\theta\right)\right), \tag{6}$$

through a simple stress boundary condition [29]. This static wetting model introduces a force acting towards an equilibrium wetting angle θ_{eq}. Within the SPH framework, surface tension can be incorporated as volumetric interface force following Brackbill et al. [32].

Instead of determining the contributions of capillary, Marangoni and wetting forces separately, a total stress is formulated Π at the interface that naturally contains all effects. The surface tension contributions Eqs. (4)–(6) then follow from the divergence of the stress tensor

$$\nabla\cdot\Pi = \nabla\cdot\left(\sigma\left(I - \mathbf{n}\otimes\mathbf{n}\right)\right), \tag{7}$$

with the identity matrix I [32,33]. Note, wetting is incorporated into the tensor through prescribed normal vectors towards the equilibrium interface normal direction [29]. The time step and stability are enhanced by considering a density weighted approach, where interface forces are applied proportional to the respective interface phase densities [26].

Within the material, energy dissipation is modeled by Fourier's law. Phase change is considered by a non-isothermal melting and solidification approach incorporating latent heat. The considered substrate material is stainless steel 316. For an accurate representation the temperature-dependent material properties as listed in Appendix A are included in the numerical model. The reader is referred to [21] for more details about the numerical model.

Powder is discarded in this study as the randomness of powder introduces another source of uncertainty. Instead, focusing on bare plate experiments allows to directly connect melt pool behavior to the laser profile. The applied recoil pressure evaporation model considers a constant latent heat of phase change and discards particle collision effects in the derivation of the condensation flux [34] as well as preferential element evaporation of multi-component alloys [35]. The escaping vapor phase and its impact on the ambient flow field is not considered. The surface tension of the liquid melt is directly proportional to the local temperature following the material model as stated in Appendix A. The build chamber in the experiments used for validation is flooded with Argon gas leaving a residual oxygen content of 0.2% [15]. This condition is considered in the simulations by using argon as shielding gas. However, the numerical model does not incorporate the impact of surface-active agents such as sulfur and oxygen possibly present at the material surface.

As the present study focuses on the impact of laser beam shapes, particular care is taken of accurate laser beam modeling. To predict the energy deposition accurately, a precise beam shape representation and multi-reflection model are considered using a ray tracing scheme following [36]. Therefore, a laser beam is represented by a defined

Table 1
Simulation domains.

Domain	Substrate	Gas
# 1	Ø400 × 200 μm³	Ø400 × 40 μm³
# 2	2300 × 400 × 100 μm³	2300 × 400 × 40 μm³
# 3	2300 × 300 × 150 μm³	2300 × 300 × 60 μm³

number of discrete rays that carry a portion of its energy. Different beam shapes are modeled by distributing the respective intensity profile in accordance to the position of a ray within the beam profile. Multi-reflections are considered by advancing the rays according to geometrical optics. With each laser-matter interaction, energy is transferred to the material and the ray energy is attenuated. Ray paths continue to be traced until their energy falls to below 1% of the initial value. Note, that explicit interface reconstruction of the discretized phases is not necessary with the employed SPH method. Rather, ray reflections are determined from the nearest interface particle approximation using their local normal vectors. The material specific normal absorbance governs the actual energy deposition, see Appendix A. The stainless steel 316 base plate used in the experimental validation data is sandblasted. The impact of the rough surface is incorporated into the numerical model by an increased radiative normal absorptance. The substrate normal absorptance is chosen as $\alpha_n = 0.62$. It follows from a linear extrapolation based on absorption measurements of rough metal surfaces [37] and the stated surface roughness in the experimental validation data [15]. The liquid absorption is chosen as $\alpha_n = 0.35$, which is well among typical values found in literature [38–42]. The normal absorptivity is corrected for the incident angle between laser ray and local surface normal, θ_a, according to Schlicks approximation $\alpha = \alpha_n \left(1 - (1 - \cos(\theta_a))^5\right)$ [43]. Finally, to avoid artifacts by local peaks, the deposited energy is smoothed between neighboring interface particles. Rays are propagated in pseudo-time between two SPH time steps. Shield gas is considered as an inert medium with respect to the laser, and the entire laser energy is deposited into the solid and the liquid phase.

The general multi-phase WCSPH method is based on the work of Hu and Adams [25], enhanced by the transport velocity scheme of Adami et al. [28] to suppress tensile instabilities. Time integration is done by the velocity-verlet scheme [44]. The minimal time step is determined from the minimum of convective, viscous, surface-tension, recoil-pressure and conduction conditions [29,45–47], and for all simulations results in 8.3 ns. The numerical sound speed of the weakly compressible approach is 70.3 m/s. As kernel function we use the Quintic Spline with a smoothing length equal to the particle spacing and a cut-off radius of three times the particle spacing. The algorithm utilizes the scalable OpenFPM framework by applying the provided domain decomposition, data structures, cell lists, communication and memory management [48]. The compute times of the single track simulation on an A100 GPU amounts to 87 to 195 GPU hours depending on the setup.

In the present study we focus on two beam shapes, namely a Gaussian profile and a point-ring profile. The latter is characterized by an intensity distribution of 40% in the point and 60% in the ring, labeled as variable beam parameter product 4 (VBPP4). According to the experimental data, we utilize spot diameters of 107 μm (Gaussian) and 253 μm (VBPP4), respectively [15]. Note, that different than the experiments we analyze both beam sizes for each of the profiles. The respective intensity distributions are shown in Fig. 2. To provide a clear indication of spatial locations, the labels C, R and R' are introduced, corresponding to the positions of the central peak intensity, ring intensity peak, and ring intensity valley, respectively. In case of laser movement, the peak and valley intensities are further differentiated by labels U and D denoting upstream and downstream positions relative to the laser motion.

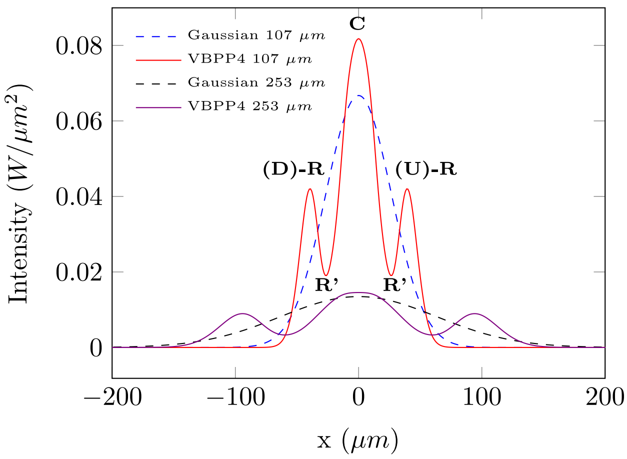

Fig. 2. Laser intensity distribution of Gaussian and VBPP4 profile with both 107 μm and 253 μm spot diameters.

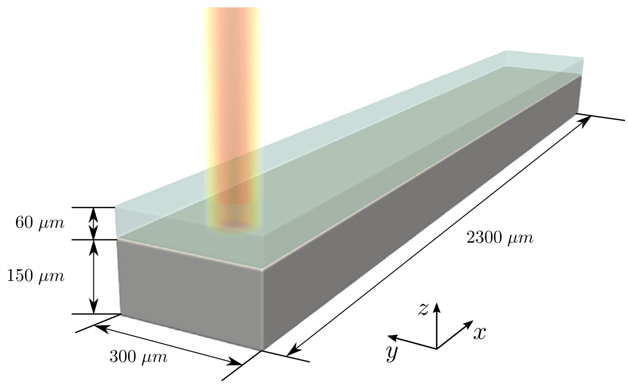

Fig. 3. Simulation domain for single melt track study consisting of 2300 × 300 × 150 μm substrate plate covered by a 60 μm gas layer. At initialization the laser beam is located at position (150, 0, 0).

Furthermore, we investigate the melt-pool dynamics during fixed laser beam irradiation and the single-melt-tracks. Following domain size studies the domains are set as listed in Table 1. At these domain sizes no influence of the boundary conditions on the melt pool dimensions and temperature distribution were found. For fixed laser beam simulations the cylindrical domain # 1 is utilized. For the single track simulations with 253 μm and 107 μm spot diameter laser beams domains # 2 and # 3 are chosen, respectively. Here, the increased domain width or depth ensure no boundary effects for wider or deeper melt pools. In Fig. 3 the domain for single track simulations with lasers of spot diameter 107 μm is shown exemplary. The respective domains are enclosed by three boundary-particle layers. At the domain boundaries a Dirichlet condition enforces a far field temperature of 300 K. Between solid and fluid phases a no slip boundary condition is applied. Following a resolution study on melt pool dimensions the initial particle spacing is set to 2.5 μm. This resolution is applied in all presented studies. Thus, the small and large beams used in the study are resolved by 21 and 50 SPH particles across their spot radius r_s, respectively. The laser is positioned at coordinates (150 0 0) and traverses at scan speed u to location (2150 0 0). The investigated process parameter sets are listed in Table 2 together with a volumetric energy density defined as VED = P / (u r_s^2). Laser power is kept at a constant 300 W in all studies.

Table 2
Single-melt-track simulation parameters.

Beam shape unit	Spot diameter (μm)	Power (W)	Scan speed (mm/s)	VED = P/(u r_s^2) (J/mm^3)
Gaussian	107	300	800	131.0
Gaussian	107	300	1100	95.3
Gaussian	107	300	1400	74.9
Gaussian	107	300	1700	61.7
Gaussian	253	300	1100	16.9
VBPP4	107	300	1100	95.3
VBPP4	253	300	800	23.3
VBPP4	253	300	1100	16.9
VBPP4	253	300	1400	13.3
VBPP4	253	300	1700	10.9

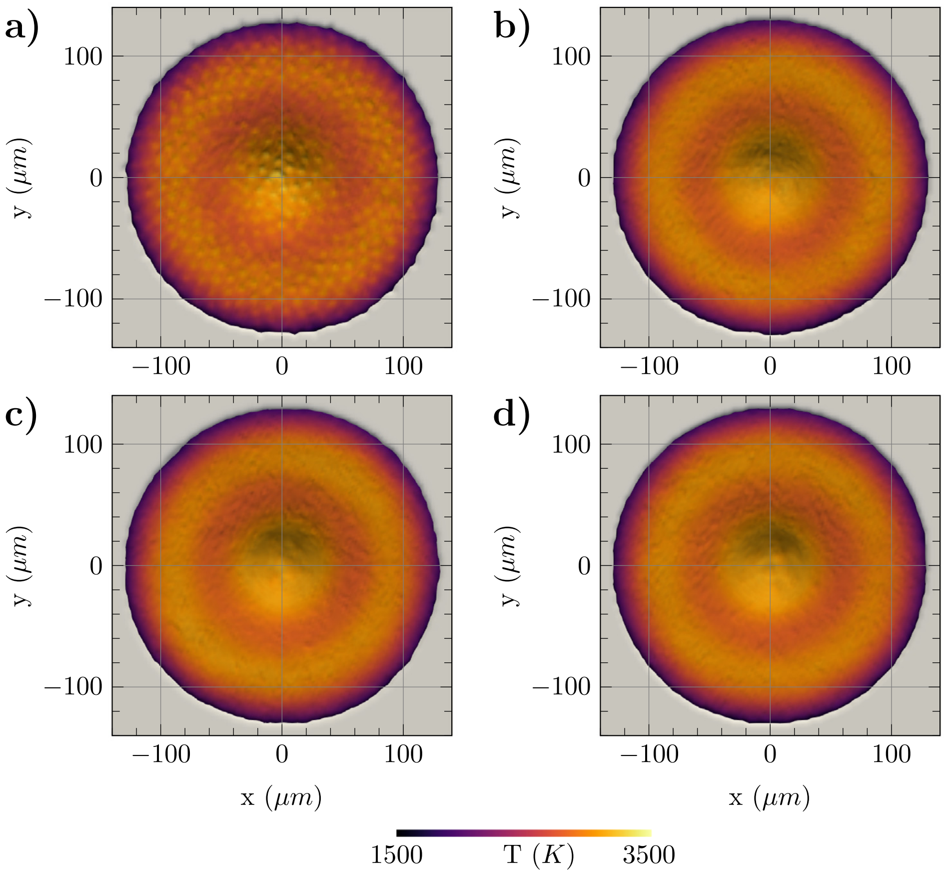

Fig. 4. Top view after $t = 250$ μs laser irradiation with VBPP4 profile at fixed laser position where the laser beam is discretized by (a) 500, (b) 2000, (c) 4000 and (d) 8000 rays.

3. Results

3.1. Validation

The simulation model is validated by comparison to the experimental data by Grunewald et al. [15], where the influence of Gaussian and point-ring laser profiles on single-melt-tracks with an AFX-1000 (nlight Inc) printer has been investigated. In total 120 different parameter sets of scan speed, laser power and beam shape are considered in [15]. The width, depth and cross sectional area of the melt pool are extracted from two cross section micro-graphs per single track. The tracks are melted on a bare AISI 316L plate.

To ensure an accurate laser representation we perform a ray resolution study. The cylindrical domain is chosen for a fixed VBPP4 laser beam of 253 μm spot diameter. This profile has a large beam area and pronounced intensity variations within small spatial dimensions that are to be resolved. Hence, it requires more laser rays than a small Gaussian profile. Fig. 4 shows the top view of the base plate after 250 μs of laser irradiation with a fixed laser beam at 300 W laser power. The substrate is displayed in gray, while the melt is color-coded with temperature. The ray resolution is varied between 500, 2000, 4000 and 8000 rays over the cut-off area. At 500 rays the laser ray discretization shows a visible sunflower pattern clearly indicating insufficient resolution, see Fig. 4(a). The expected low temperature ring below the laser intensity valley at location R’ is more diffuse than in the other cases. Starting from 2000 rays, shown in Fig. 4(b), the temperature hot-spots disappear and the low temperature ring is clearly visible. Higher ray resolutions show only marginal effects on melt-pool shape, mainly within the central cavity, see Fig. 4(c) and (d). The melt-pool width is not sensitive to the number of rays and also the melt-pool depth only increases by 2.5 μm for ray resolutions of 4000 and 8000 rays (not shown here).

The surface temperature distribution along the x-coordinate at $y = 0.0$ is displayed in Fig. 5 after 220, 250 and 280 μs of laser irradiation, respectively. The temperature distribution closely follows the intensity distribution of the laser beam. From Fig. 5 we identified 4000 to be the minimum required number of rays to capture the temperature plateau in the core region and the temperature peaks from the ring-profile.

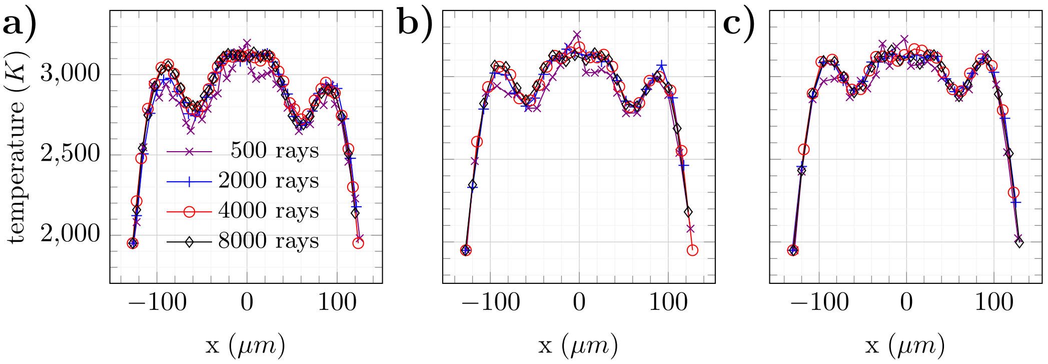

Fig. 5. Temperature distribution along x-axis at $y = 0$ after (a) 220 μs, (b) 250 μs, and (c) 280 μs of laser irradiation with laser profile VBPP4.

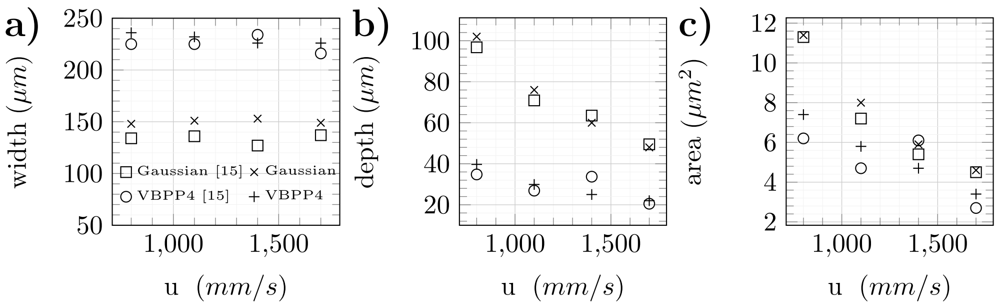

Fig. 6. Comparison of single melt-track dimensions from our simulations and experimental data from [15]: (a) width, (b) depth, and (c) cross sectional area for different laser scan speeds and laser profiles.

To validate the full numerical model we compare the dimension of single-melt-track simulations at different process parameters and different beam shapes with experimental data. The setup follows the experimental study by Grunewald et al. [15]. The laser power is kept at constant 300 W while the scan speed is changed in steps of 300 mm/s from 800 mm/s to 1700 mm/s. Fig. 6 shows the comparison between experimental and simulation data for melt-pool (a) width, (b) depth, and (c) cross sectional area, respectively. The predicted dimensions agree well with the experimental data. Remaining deviations between experiment and simulation might be ascribed to the simplifications of the applied evaporation model, the simplified incident angle relation of the laser, discarded surfactants like oxygen or sulfur present on the substrate or the comparison to averaged experimental measurements discarding data variance.

Now, we investigate the effect of the beam shape on the melt-pool evolution at different beam sizes for the Gaussian and the VBPP4 profile. Note, here we match the beam sizes to compare similar heating in the irradiated zones, see Fig. 2.

3.2. Fixed laser

The examination of fixed-laser energy deposition allows for a detailed analysis of the induced melt-pool dynamics by the beam shape without the influence of the laser scan speed. We use simulation domain # 1, as stated before and irradiate the base plate surface with the respective intensity distributions.

The substrate is heated up and, eventually, forms the melt pool. In Fig. 7, a central cut through substrate and melt pool are shown for irradiation by different beam shapes. The melt pool is color-coded by temperature. A black line represents the liquid–solid and liquid-gas interface. Stream lines indicate the local flow velocity field within the melt pool. They are color coded by the velocity magnitude where white indicates low and dark blue high velocities. Small black arrows denote the flow direction. Above the melt pool the laser beam shapes are outlined.

In Fig. 7(a), the melt pool is shown at t = 42.5 μs with a Gaussian laser beam of spot diameter d = 107 μm. A narrow melt pool with deep cavity has formed, where the melt in the center reaches the boiling temperature. The flow field is characterized by a downward motion due to the evaporation-induced recoil pressure effect. Outside the center, the melt is advected radially outwards forming a toroidal lip above the substrate.

In Fig. 7(b) the corresponding melt pool at t = 42.5 μs with a VBPP4 profile of the same spot diameter of d = 107 μm is shown. Clearly, the respective laser beam shape reflects in shape and temperature of the generated melt pool. Together, point and ring intensity distributes cause a melt-pool depression forming an undulatory cavity. Overall, the pool dimensions and velocity magnitudes are of comparable size.

Fig. 7(c) shows the melt pool generated at t = 250 μs by a Gaussian laser with an increased spot diameter of d = 253 μm at identical power. The melt pool is now shallow and wide. Still a cavity occurs in the very core region yet at a reduced level of overheating.

The melt pool induced by the VBPP4 profile at same beam size is shown in Fig. 7(d). The disc-like melt-pool is now depressed by a small central cavity only. Boiling temperature is only reached in proximity to the laser-spot center. In region of the intensity valley, R’, the melt temperature is decreased. From the high temperature region below the peak ring irradiation, R, melt flow is directed both inwards and outwards towards the respective cooler areas. In the cooler region, R’, two melt streams meet, slow down and change direction. At the melt-pool edge, where temperature gradients are large, increasing velocities at the surface and a re-circulation region are found. Also, at low power densities the beam shape affects the melt-pool evolution, as the flow velocity is changed by the irradiation profile. The melt cavity induced by the point-ring profile is smaller while the pool width is slightly increased.

Vapor cavity evolution under Gaussian and VBPP4 laser beam shape irradiation is shown in Fig. 8(a) and (b), respectively. Initially the beam shape translates to a distinct melt pool shape, yet as the vapor cavity advances into the material the differences become less pronounced. Specifically, the undulatory shape due to the VBPP4 beam irradiation is no longer clearly evident after 75 μs.

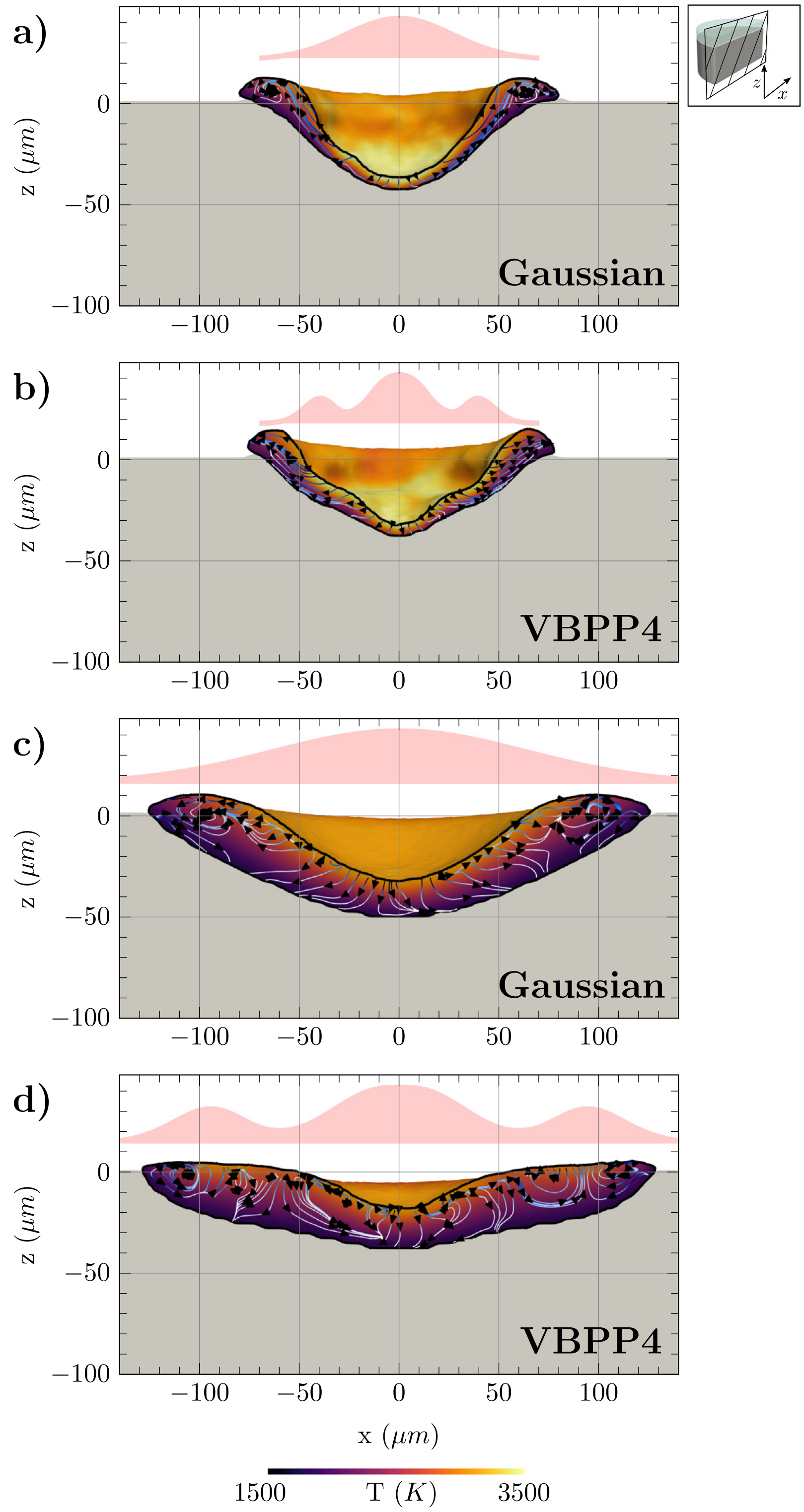

Fig. 7. Cross section view of melt pool after $t = 42.5$ μs irradiation with (a) Gaussian profile with 107 μm spot diameter, (b) VBPP4 profile with 107 μm spot diameter, and after $t = 250$ μs irradiation with (c) Gaussian profile with 253 μm spot diameter, and (d) VBPP4 profile with 253 μm spot diameter.

3.3. Single-melt-tracks

In the following section we study the influence of the beam shape at two different power densities on single tracks using the Gaussian and the VBPP4 profile. We limit the investigation to a single scan speed of 1100 mm/s. With this scan speed the studied VED= $P/(ur_s^2)$ are VED= 95.3 J/mm^3 and VED= 16.9 J/mm^3 for spot diameters 107 μm and 253 μm respectively. All other settings are taken from the previous section.

At first, pool shape and surface temperature distribution are compared. In the lower half of Fig. 9(a) the melt-pool contour at the central x-z-plane is depicted for the Gaussian and VBPP4 profiles with

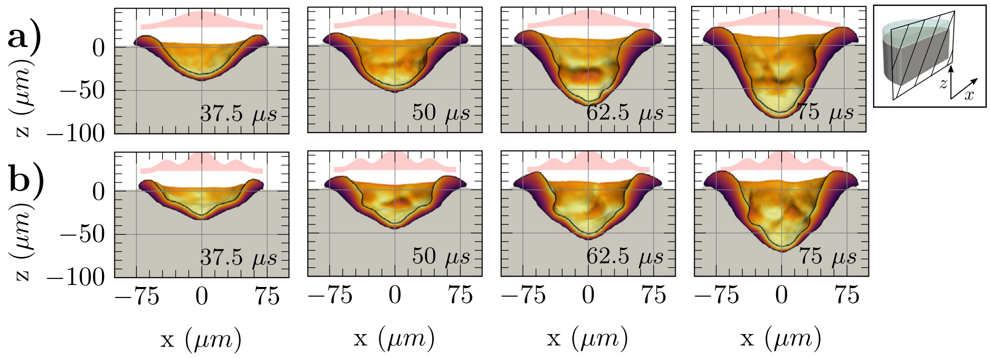

Fig. 8. Development of melt pool cross section after t = 37.5 μs, t = 50.0 μs, t = 62.5 μs, and t = 75.0 μs of irradiation with (a) Gaussian profile of 107 μm spot diameter and (b) VBPP4 profile of 107 μm spot diameter.

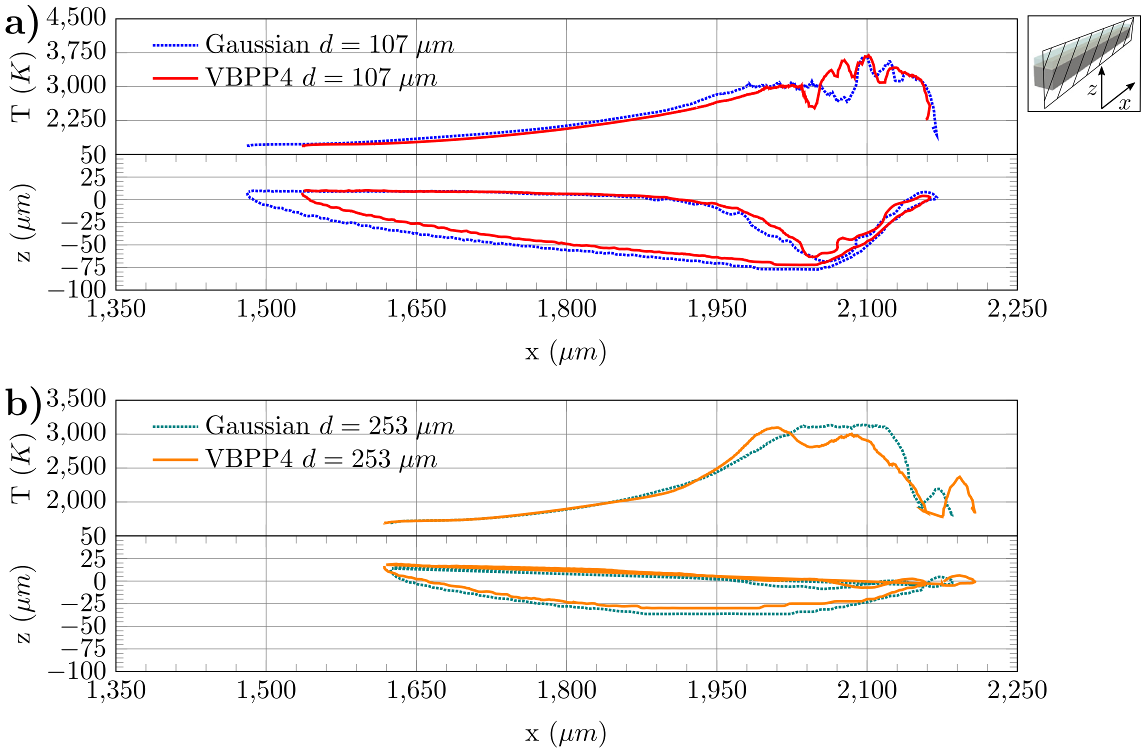

Fig. 9. Melt pool contour and surface temperature distribution after t = 1780 μs of laser irradiation with Gaussian and VBPP4 profile with spot diameters of (a) 107 μm and (b) 253 μm.

spot diameter of 107 μm. In the upper half the corresponding surface temperatures are plotted. Energy deposition with the Gaussian profile leads to a slightly deeper and longer melt pool. Within the vapor cavity, the melt-pool morphology is characterized by small-scale disturbances. Their amplitudes are larger on the laser irradiated upstream side. The temperature distribution on the melt surface is similar for both irradiation profiles, and no distinct impact of the beam shape is revealed. In both cases there are intense fluctuations in the overheated cavity and a monotonic decay towards the trailing edge.

The corresponding shape and temperature distribution after energy deposition with the large Gaussian and VBPP4 laser profiles are shown in Fig. 9(b). The melt pools are of comparable length, yet the Gaussian irradiation induces a slightly deeper pool with a single vapor cavity below the laser spot. In the laser irradiated zone the temperature is constant at the boiling point. The melt pool formed by VBPP4 intensity distribution shows two smaller cavities in the zone of the spot, C, and at the downstream side of the ring intensity peaks, DR. The temperature decay in between corresponds to the intensity valley DR'. Both the Gaussian and VBPP4 temperature profiles show similar decay towards the trailing edge of the melt pool.

A closeup of the laser irradiated zone of single track simulations with laser scan velocity of 1100 mm/s are shown in Fig. 10. Depicted are central x-z cuts through both substrate and melt pool. The melt cross section contour is highlighted by a black line. The melt pool is color coded by temperature. Velocity stream lines with arrows describe the instantaneous local flow field. The respective laser irradiation zones are indicated by laser profiles above the melt pool.

The melt pool forming due to laser irradiation with a Gaussian profile of spot diameter 107 μm is shown in Fig. 10(a). Local differences in evaporation and thus recoil pressure acceleration lead to a wavy surface morphology. The results show marginal velocities within the melt-pool bulk suggesting melt flow to be present mainly at the surface.

The melt-pool cross section forming due to energy deposition with the VBPP4 profile is shown in Fig. 10(b). There are no distinct differences in flow dynamics and surface morphology compared to the case of Gaussian laser irradiation.

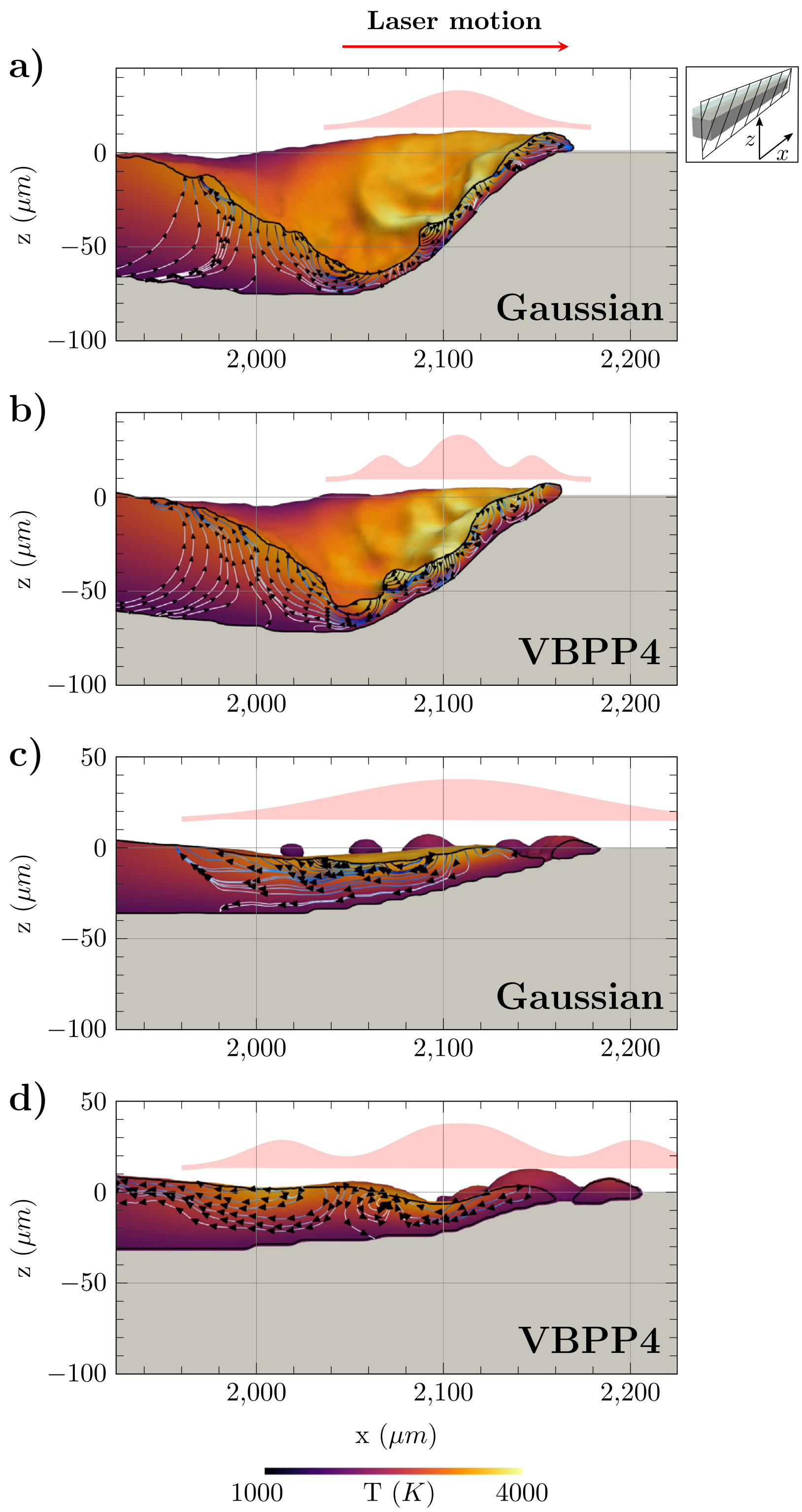

Fig. 10. Cross section view of single melt track with laser irradiation of (a) Gaussian profile with 107 μm spot diameter, (b) VBPP4 profile with 107 μm spot diameter, (c) Gaussian profile with 253 μm spot diameter, and (d) VBPP4 profile with 253 μm spot diameter. Laser scan speed of 1100 mm/s.

In Fig. 10(c) the melt pool forming under a Gaussian laser beam with spot diameter of 253 μm is illustrated. A single shallow cavity is formed with smooth surface topology. Flow velocity is directed downstream within most of the cavity. Only at the far upstream side, where temperature gradients are high, the velocity field shows upstream motion.

Finally, the melt-pool cross section resulting from irradiation with a VBPP4 profile with spot diameter 253 μm is shown in Fig. 10(d). Instead of a single cavity, there are two smaller cavities close to the positions C and DR of central spot and downstream ring intensity peaks. From the two cavities there is a surface flow towards the cooler region DR' between them. Due to this local flow behavior, velocity magnitudes are decreased compared to the scenario with Gaussian irradiation.

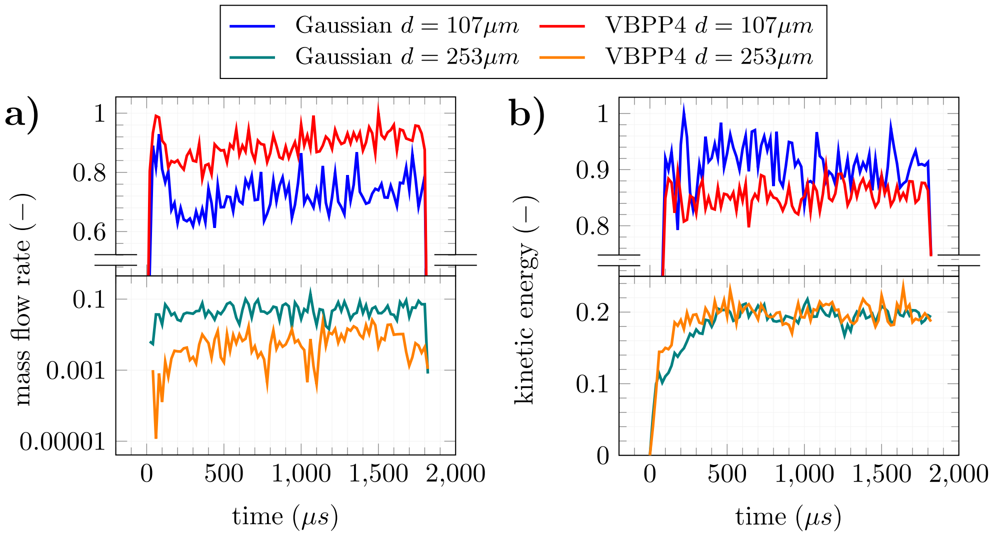

Fig. 11. Development of (a) evaporation mass flow rate and (b) kinetic energy in single track melt pools irradiated by Gaussian and VBPP4 beam profiles.

Melt-pool evaporation is known to affect the powder layer in laser-based powder bed fusion of metal [49] and can lead to powder denudation and spatter. Thus, its control is important for multi-material manufacturing [1]. In addition, it is one of the main drivers of melt-pool dynamics and thus a key phenomenon to control. To quantify the effect of beam-shaping on evaporation we track the evaporation mass-flow rate, calculated from Eq. (3). In Fig. 11 we compare this mass-flow rate together with the kinetic energy of the melted fluid phase for both beam shapes at the two power densities. The switch in beam shape from Gaussian to VBPP4 increases the evaporation mass-flow rate by an average of 24.5% at high power density. In contrast, at low power density the mass-flow rate is 82% lower when the VBPP4 profile is applied, and evaporation is almost fully avoided. Interestingly, fluctuations in the mass-flow rate are reduced with the VBBP4 profile both at high and low power densities. At high power densities the evaporation mass flow rate quickly increases followed by a drop after about 100 μs. The results show a larger surface area with temperatures above the boiling point during the initial stage of melt pool development. One contributing factor could be the smaller surface area of the vapor cavity onto which the laser energy is deposited via multi-reflections.

To find the impact of the beam shape on the global flow dynamics the kinetic energy is tracked over time and plotted in Fig. 11(b). At high power densities the Gaussian laser induces higher kinetic energy in the melt pool than irradiation with the VBPP4 beam shape. Note, that the increased evaporation under VBPP4 laser radiation does not lead to an increased total kinetic energy. At low power densities the beam shape does not impact the total melt-pool kinetic energy.

4. Discussion

By first studying fixed-laser beam irradiation on bare plates with different laser profiles, the impact of laser motion is discarded and the problem is reduced to the influence of beam shape at different beam sizes. The beam size controls the energy density and thus the impact of evaporation on pool shape, size and dynamics. At small beam sizes, we find a larger region of boiling and superheated temperature, leading to increased evaporation rates and flow speeds. Below the boiling point, intense temperature gradients are mainly found at the melt-pool fringes. Thus the cause for melt dynamics within the melt cavity is attributed to evaporation rather then Marangoni effects. The beam shape changes the distribution of energy and thus the regions of superheated temperature and evaporation. As a result, the melt-pool shape and dynamics within the vapor cavity are adjusted by the beam shape. At large beam sizes, the contribution by evaporation is reduced. As a result, smaller cavities form and the flow velocity is reduced. Temperature gradients within the laser irradiated zone result in an increase of Marangoni convection. This is particularly evident for the melt pool forming with the VBPP4 profile. Here, the cavity remains smaller due to an inward motion of melt from region R to R'. Hence, beam shape leads to a variation of surface tension gradients and the resulting local melt dynamics. Comparison of the melt cavity development under high VED Gaussian and VBPP4 beam irradiation shows less pronounced shape differences at later times. In the deep vapor cavities instabilities and a high degree of multi-reflections weaken the clear translation of the beam shape to the melt pool shape.

Finally, simulation results of single-melt-tracks using both Gaussian and VBPP4 profiles are analyzed. Both the high VED Gaussian and low VED VBPP4 melt pool dimensions are in good agreement with the experimental results by Grunewald et al. [15] suggesting comparable global melt pool behavior. At high energy densities melt-pool contours suggest a minor impact of the specific beam shape on the melt-pool depth, length and topology. An explanation for similar melt-pool shapes is the increase in multi-reflections that diminish effective differences between beam shapes. The temperature distribution on the melt surface is comparable as well. An overall temperature level above the boiling point suggests a minor significance of Marangoni convection within the vapor cavity. The investigation of the local flow field suggests high evaporation-induced flow velocities in the vapor cavity that show no clear dependence on the specific beam shape. A distinct cavity shape developing under irradiation with the VBPP4 profile for a fixed laser no longer is observed. In contrast, at low power densities, the beam shape shows a stronger influence on the resulting melt pool. A decreased surface temperature at the location DR' has a clear impact on the local flow field. The melt flow changes direction between two cavities forming at locations C and DR. At location DR' melt accumulates forming a small peak. This can be explained by Marangoni convection towards this region. Hence, the results suggest in scenarios where energy absorption is mainly determined by the beam shape rather than multi-reflections its effects on the melt pool are more pronounced.

At low energy densities, beam-shaping has the potential to fully suppress the evaporation mass-flow. In contrast, when power densities are high the opposite trend is found. Fluctuations in the mass-flow rate are significantly reduced by the VBPP4 profile emphasizing its potential to achieve a more stable vapor cavity. From kinetic energy measurements we find that higher evaporation with the VBPP4 profile does not lead to overall increased kinetic energy of the melt pool. While at low power densities the observed melt-pool cross sections suggest a significant influence of the laser beam shape on the local melt-pool flow field, their impact on the kinetic energy within the melt pool remains small. Overall, kinetic energies are comparable for both investigated beam shapes. The evaluation of mass-flow rate and kinetic energy highlight the significance of the laser beam size rather than the beam shape on the evaporation and melt-pool kinetic energy.

5. Conclusions

To study the influence of laser beam shapes on the melt-pool formation a simulation campaign for single-melt-tracks on a base plate has been conducted for Gaussian and point-ring laser intensity distributions. The investigation is conducted with two different beam sizes to draw conclusions about how the beam size influences the beam shape effect. The simulation model considers all relevant interface dynamics including evaporation effects and surface tension forces. Resulting melt pool dimensions including penetration depths and thermal gradients are accurately predicted allowing for a quantitative comparison of the beam shape effect.

To ensure a precise energy deposition into the material, the applied ray tracing scheme is verified by a resolution study for fixed-laser irradiation on a substrate plate. The model is capable to resolve both the prescribed intensity distribution and multi-reflections within the forming melt cavity. Simulation model validity is further established by comparison of single-melt-track simulations with experimental data. Melt-track width, depth, and cross section area are in good agreement, both, for a low energy-density point-ring beam and a high energy-density Gaussian beam irradiation.

The study of melt-pool evolution for laser irradiation by fixed laser beams demonstrates the dependence of the beam-shaping effect on beam size. The Gaussian and point-ring beam profiles are studied at 107 μm and 253 μm beam diameters. Beam size controls the energy density and thus the melt pool surface temperature and evaporation intensity. At high energy density a change in beam shape results in a change in the distribution of evaporation forces. In turn, the local flow field and vapor cavity shape are changed. However, with increased irradiation time the shape differences of the vapor cavities are less pronounced. At low energy density, the flow field is governed by Marangoni convection induced by the local surface temperature gradients. The beam shape adjusts these temperature gradients which in the case of the point-ring profile leads to a reduction of a central vapor-cavity.

Single-melt-tracks simulation results suggest a minor impact of the beam profile on melt-pool depth, length and topology at high energy densities. No clear influence on the local flow field, temperature distribution and cavity shape can be observed. In contrast, at low energy density both the flow field and the melt pool topology are influenced by the beam shape.

Beam-shaping shows opposite trends on the evaporation mass flow rate for small and large beam sizes. Hence, it is important to consider overall process parameters when selecting a beam shape. Both evaporation mass flow rate and total melt-pool kinetic energy depend more on the beam size rather than shape for the considered process parameters.

While no powder is considered in the present study the result suggest to be transferable to scenarios including powder. The melt-pool shape, dynamics and evaporation effects show a strong dependence on the irradiation of the melt pool rather than the substrate. It is the distribution of surface tension and evaporation forces that drive the flow. We expect the same to be true in scenarios with powder. However, power density showed relevant for the beam shape influence and we also expect the powder layer height to influence the required power density. Before transferring the results to scenario with powder, the applied beam power should be adjusted to ensure a comparable melt pool development within the laser irradiated zone.

The present study shows significantly different melt-pool behavior at the two considered power densities. It is important to choose comparable laser beam sizes and power densities in order to isolate the effect of laser beam shape. While beam shape effects are evident at low power densities and during the initial development of vapor cavities, they became less pronounced in the deep vapor cavities of fixed irradiation and single melt tracks at high power densities. Building on this, we propose future studies to investigate the impact of power density, vapor cavity instability, and multi-reflections on the beam shape effect. We suggest to include powder and its layer height as parameter in these studies to account for its impact on power density requirements. Also, comparing different point-ring power distributions is of interest.

CRediT authorship contribution statement

C. Zöller: Writing – review & editing, Writing – original draft, Visualization, Validation, Software, Methodology, Investigation, Formal analysis, Data curation, Conceptualization. **N.A. Adams:** Writing – review & editing, Resources, Project administration, Funding acquisition. **S. Adami:** Writing – review & editing, Supervision, Software, Methodology, Investigation, Formal analysis, Conceptualization.

Declaration of competing interest

The authors declare that they have no known competing financial interests or personal relationships that could have appeared to influence the work reported in this paper.

Table A.3
Stainless Steel 316 material properties

Notation	Property		Value	Units	Source
T_s	solidus temperature	–	1673	K	[50]
T_l	liquidus temperature	–	1727	K	[50]
T_{ev}	boiling temperature	–	3090	K	[40]
ρ_0	density	–	7200	kg/m^3	[51]
ν	dynamic viscosity	$T_s \leq T$	$0.2536e^{-3}\exp(5492.2/T)$	Pas	[52]
σ	surface tension coefficient	$T_s \leq T$	$1.6 - 0.4e^{-3}$ T	N/m	[38,42]
λ	thermal conductivity	$T \leq T_l$	11.44 + 0.0136 T	W/mK	[50]
		$T_l < T$	6.4881 + 0.0129 T		[50]
c_p	specific heat capacity	$T \leq T_l$	462.656 + 0.1338 T	J/kgK	[52]
		$T_l < T$	775	J/kgK	[40]
α_s	solid absorptivity	–	0.62	–	[37]
α_l	liquid absorptivity	–	0.35	–	[38–42]
$h_{ev,n}$	latent heat of evaporation	–	7.45e6	J/kg	[40,41]
h_{ev}	molar heat of evaporation	–	416 753	J/mol	
M	molar mass	–	55.94e−3	kg/mol	[52]

Data availability

Data will be made available on request.

Acknowledgments

The authors gratefully acknowledge funding through the TUM-Oerlikon Advanced Manufacturing Institute project GasAlloy-Y at the Munich Institute of Integrated Materials, Energy and Process Engineering. Computing time was provided by the Gauss Centre for Supercomputing e.V. (www.gauss-centre.eu) at the Leibniz Supercomputing Centre (www.lrz.de).

Appendix A. Material properties SS316

See Table A.3.

References

[1] J. Grünewald, J. Reimann, K. Wudy, Influence of ring-shaped beam profiles on spatter characteristics in laser-based powder bed fusion of metals, J. Laser Appl. 35 (4) (2023).

[2] J. Bi, L. Wu, S. Li, Z. Yang, X. Jia, M.D. Starostenkov, G. Dong, Beam shaping technology and its application in metal laser additive manufacturing: A review, J. Mater. Res. Technol. (2023).

[3] F. Nahr, D. Bartels, R. Rothfelder, M. Schmidt, Influence of novel beam shapes on laser-based processing of high-strength aluminium alloys on the basis of EN AW-5083 single weld tracks, J. Manuf. Mater. Process. 7 (3) (2023) 93.

[4] S.N.R. Abadi, Y. Mi, F. Sikström, A. Ancona, I. Choquet, Effect of shaped laser beam profiles on melt flow dynamics in conduction mode welding, Int. J. Therm. Sci. 166 (2021) 106957.

[5] R. Shi, S.A. Khairallah, T.T. Roehling, T.W. Heo, J.T. McKeown, M.J. Matthews, Microstructural control in metal laser powder bed fusion additive manufacturing using laser beam shaping strategy, Acta Mater. 184 (2020) 284–305.

[6] T.T. Roehling, S.S. Wu, S.A. Khairallah, J.D. Roehling, S.S. Soezeri, M.F. Crumb, M.J. Matthews, Modulating laser intensity profile ellipticity for microstructural control during metal additive manufacturing, Acta Mater. 128 (2017) 197–206.

[7] T.T. Roehling, R. Shi, S.A. Khairallah, J.D. Roehling, G.M. Guss, J.T. McKeown, M.J. Matthews, Controlling grain nucleation and morphology by laser beam shaping in metal additive manufacturing, Mater. Des. 195 (2020) 109071.

[8] Y. Mi, S. Mahade, F. Sikström, I. Choquet, S. Joshi, A. Ancona, Conduction mode laser welding with beam shaping using a deformable mirror, Opt. Laser Technol. 148 (2022) 107718.

[9] M. Sow, T. De Terris, O. Castelnau, Z. Hamouche, F. Coste, R. Fabbro, P. Peyre, Influence of beam diameter on laser powder bed fusion (L-PBF) process, Addit. Manuf. 36 (2020) 101532.

[10] W. Yuan, H. Chen, S. Li, Y. Heng, S. Yin, Q. Wei, Understanding of adopting flat-top laser in laser powder bed fusion processed Inconel 718 alloy: Simulation of single-track scanning and experiment, J. Mater. Res. Technol. 16 (2022) 1388–1401.

[11] A. Okunkova, M. Volosova, P. Peretyagin, Y. Vladimirov, I. Zhirnov, A. Gusarov, Experimental approbation of selective laser melting of powders by the use of non-Gaussian power density distributions, Physics Procedia 56 (2014) 48–57.

[12] T.M. Wischeropp, H. Tarhini, C. Emmelmann, Influence of laser beam profile on the selective laser melting process of AlSi10Mg, J. Laser Appl. 32 (2) (2020).

[13] S.N. Grigoriev, A.V. Gusarov, A.S. Metel, T.V. Tarasova, M.A. Volosova, A.A. Okunkova, A.S. Gusev, Beam shaping in laser powder bed fusion: Péclet number and dynamic simulation, Metals 12 (5) (2022) 722.

[14] T.U. Tumkur, G. Guss, J.D. Roehling, S.A. Khairallah, M.J. Matthews, Metal additive manufacturing using complex beam shaping, Procedia CIRP 111 (2022) 71–74.

[15] J. Grünewald, F. Gehringer, M. Schmöller, K. Wudy, Influence of ring-shaped beam profiles on process stability and productivity in laser-based powder bed fusion of AISI 316L, Metals 11 (12) (2021) 1989.

[16] R. Rothfelder, F. Huber, M. Schmidt, Influence of beam shape on spatter formation during PBF-LB/M of Ti6Al4V and tungsten powder, Procedia CIRP 111 (2022) 14–17, http://dx.doi.org/10.1016/j.procir.2022.08.105, 12th CIRP Conference on Photonic Technologies [LANE 2022].

[17] T.M. Wischeropp, R. Salazar, D. Herzog, C. Emmelmann, Simulation of the effect of different laser beam intensity profiles on heat distribution in selective laser melting, in: Lasers in Manufacturing Conference, June 22–25, WLT Munich, Germany, 2015.

[18] T.U. Tumkur, T. Voisin, R. Shi, P.J. Depond, T.T. Roehling, S. Wu, M.F. Crumb, J.D. Roehling, G. Guss, S.A. Khairallah, et al., Nondiffractive beam shaping for enhanced optothermal control in metal additive manufacturing, Sci. Adv. 7 (38) (2021) eabg9358.

[19] V. Holla, P. Kopp, J. Grünewald, K. Wudy, S. Kollmannsberger, Laser beam shape optimization in powder bed fusion of metals, Addit. Manuf. 72 (2023) 103609.

[20] J. Grünewald, V. Blickle, M. Allenberg-Rabe, P. Wagenblast, K. Wudy, Flexible and highly dynamic beam shaping for laser-based powder bed fusion of metals, Procedia CIRP 111 (2022) 65–70.

[21] C. Zöller, N. Adams, S. Adami, Numerical investigation of balling defects in laser-based powder bed fusion of metals with Inconel 718, Addit. Manuf. (2023) 103658.

[22] M. Russell, A. Souto-Iglesias, T. Zohdi, Numerical simulation of laser fusion additive manufacturing processes using the SPH method, Comput. Methods Appl. Mech. Engrg. 341 (2018) 163–187.

[23] J. Weirather, V. Rozov, M. Wille, P. Schuler, C. Seidel, N.A. Adams, M.F. Zaeh, A smoothed particle hydrodynamics model for laser beam melting of Ni-based alloy 718, Comput. Math. Appl. 78 (7) (2019) 2377–2394.

[24] J.-P. Fürstenau, H. Wessels, C. Weißenfels, P. Wriggers, Generating virtual process maps of SLM using powder-scale SPH simulations, Comput. Part. Mech. 7 (4) (2020) 655–677.

[25] X. Hu, N. Adams, A multi-phase SPH method for macroscopic and mesoscopic flows, J. Comput. Phys. 213 (2) (2006) 844–861, http://dx.doi.org/10.1016/j.jcp.2005.09.001.

[26] S. Adami, X. Hu, N.A. Adams, A new surface-tension formulation for multi-phase SPH using a reproducing divergence approximation, J. Comput. Phys. 229 (13) (2010) 5011–5021.

[27] S. Adami, X.Y. Hu, N.A. Adams, A generalized wall boundary condition for smoothed particle hydrodynamics, J. Comput. Phys. 231 (21) (2012) 7057–7075.

[28] S. Adami, X. Hu, N.A. Adams, A transport-velocity formulation for smoothed particle hydrodynamics, J. Comput. Phys. 241 (2013) 292–307.

[29] C. Zöller, N. Adams, S. Adami, A partitioned continuous surface stress model for multiphase smoothed particle hydrodynamics, J. Comput. Phys. 472 (2023) 111716.

[30] R.H. Cole, R. Weller, Underwater explosions, Phys. Today 1 (6) (1948) 35.

[31] S.I. Anisimov, V.A. Khokhlov, Instabilities in Laser-Matter Interaction, CRC Press, 1995.

[32] J.U. Brackbill, D.B. Kothe, C. Zemach, A continuum method for modeling surface tension, J. Comput. Phys. 100 (2) (1992) 335–354.

[33] A. Krimi, M. Rezoug, S. Khelladi, X. Nogueira, M. Deligant, L. Ramírez, Smoothed particle hydrodynamics: A consistent model for interfacial multiphase fluid flow simulations, J. Comput. Phys. 358 (January) (2018) 53–87, http://dx.doi.org/10.1016/j.jcp.2017.12.006.

[34] A. Klassen, T. Scharowsky, C. Körner, Evaporation model for beam based additive manufacturing using free surface lattice Boltzmann methods, J. Phys. D: Appl. Phys. 47 (27) (2014) 275303.

[35] T.F. Flint, L. Scotti, H.C. Basoalto, M.C. Smith, A thermal fluid dynamics framework applied to multi-component substrates experiencing fusion and vaporisation state transitions, Commun. Phys. 3 (1) (2020) 196.

[36] H. Wessels, T. Bode, C. Weißenfels, P. Wriggers, T. Zohdi, Investigation of heat source modeling for selective laser melting, Comput. Mech. 63 (2019) 949–970.

[37] D. Bergström, The Absorption of Laser Light by Rough Metal Surfaces (Ph.D. thesis), Luleå tekniska universitet, 2008.

[38] T. Mukherjee, H. Wei, A. De, T. DebRoy, Heat and fluid flow in additive manufacturing–Part II: Powder bed fusion of stainless steel, and titanium, nickel and aluminum base alloys, Comput. Mater. Sci. 150 (2018) 369–380.

[39] L. Liu, M. Huang, Y. Ma, M. Qin, T. Liu, Simulation of powder packing and thermo-fluid dynamic of 316L stainless steel by selective laser melting, J. Mater. Eng. Perform. 29 (2020) 7369–7381.

[40] L. Cao, Mesoscopic-scale numerical simulation including the influence of process parameters on SLM single-layer multi-pass formation, Metall. Mater. Trans. A 51 (2020) 4130–4145.

[41] X. Chen, W. Mu, X. Xu, W. Liu, L. Huang, H. Li, Numerical analysis of double track formation for selective laser melting of 316L stainless steel, Appl. Phys. A 127 (2021) 1–13.

[42] P. Ansari, A.U. Rehman, F. Pitir, S. Veziroglu, Y.K. Mishra, O.C. Aktas, M.U. Salamci, Selective laser melting of 316L austenitic stainless steel: Detailed process understanding using multiphysics simulation and experimentation, Metals 11 (7) (2021) 1076.

[43] C. Schlick, An inexpensive BRDF model for physically-based rendering, in: Computer Graphics Forum, vol. 13, Wiley Online Library, 1994, pp. 233–246.

[44] W.C. Swope, H.C. Andersen, P.H. Berens, K.R. Wilson, A computer simulation method for the calculation of equilibrium constants for the formation of physical clusters of molecules: Application to small water clusters, J. Chem. Phys. 76 (1) (1982) 637–649.

[45] P.W. Cleary, J.J. Monaghan, Conduction modelling using smoothed particle hydrodynamics, J. Comput. Phys. 148 (1) (1999) 227–264.

[46] J.J. Monaghan, Smoothed particle hydrodynamics, Annu. Rev. Astron. Astrophys. 30 (1) (1992) 543–574.

[47] J.P. Morris, A study of the stability properties of smooth particle hydrodynamics, Publ. Astron. Soc. Aust. 13 (1996) 97–102.

[48] P. Incardona, A. Leo, Y. Zaluzhnyi, R. Ramaswamy, I.F. Sbalzarini, OpenFPM: A scalable open framework for particle and particle-mesh codes on parallel computers, Comput. Phys. Comm. 241 (2019) 155–177.

[49] S.A. Khairallah, A.T. Anderson, A. Rubenchik, W.E. King, Laser powder-bed fusion additive manufacturing: Physics of complex melt flow and formation mechanisms of pores, spatter, and denudation zones, Acta Mater. 108 (2016) 36–45.
[50] J.C. Haley, J.M. Schoenung, E.J. Lavernia, Modelling particle impact on the melt pool and wettability effects in laser directed energy deposition additive manufacturing, Mater. Sci. Eng. A 761 (2019) 138052.
[51] K.C. Mills, Recommended Values of Thermophysical Properties for Selected Commercial Alloys, Woodhead Publishing, 2002.
[52] T. Chawla, D. Graff, R. Borg, G. Bordner, D. Weber, D. Miller, Thermophysical properties of mixed oxide fuel and stainless steel type 316 for use in transition phase analysis, Nucl. Eng. Des. 67 (1) (1981) 57–74.

Bibliography

[1] Abadi, S. N. R., Mi, Y., Sikström, F., Ancona, A., and Choquet, I. "Effect of shaped laser beam profiles on melt flow dynamics in conduction mode welding". In: *International Journal of Thermal Sciences* 166 (2021), p. 106957.

[2] Adami, S., Hu, X. Y., and Adams, N. A. "A generalized wall boundary condition for smoothed particle hydrodynamics". In: *Journal of Computational Physics* 231.21 (2012), pp. 7057–7075.

[3] Adami, S., Hu, X., and Adams, N. A. "A new surface-tension formulation for multi-phase SPH using a reproducing divergence approximation". In: *Journal of Computational Physics* 229.13 (2010), pp. 5011–5021.

[4] Afrasiabi, M., Keller, D., Lüthi, C., Bambach, M., and Wegener, K. "Effect of process parameters on melt pool geometry in laser powder bed fusion of metals: a numerical investigation". In: *Procedia CIRP* 113 (2022), pp. 378–384.

[5] Afrasiabi, M., Lüthi, C., Bambach, M., and Wegener, K. "Smoothed particle hydrodynamics modeling of the multi-layer laser powder bed fusion process". In: *Procedia CIRP* 107 (2022), pp. 276–282.

[6] Afrasiabi, M., Lüthi, C., Bambach, M., and Wegener, K. "Multi-resolution SPH simulation of a laser powder bed fusion additive manufacturing process". In: *Applied Sciences* 11.7 (2021), p. 2962.

[7] Alkahari, M. R., Furumoto, T., Ueda, T., Hosokawa, A., Tanaka, R., and Abdul Aziz, M. S. "Thermal conductivity of metal powder and consolidated material fabricated via selective laser melting". In: *Key Engineering Materials* 523 (2012), pp. 244–249.

[8] Anisimov, S. I. and Khokhlov, V. A. *Instabilities in laser-matter interaction*. CRC press, 1995.

[9] Bayat, M., Thanki, A., Mohanty, S., Witvrouw, A., Yang, S., Thorborg, J., Tiedje, N. S., and Hattel, J. H. "Keyhole-induced porosities in Laser-based Powder Bed Fusion (L-PBF) of Ti6Al4V: High-fidelity modelling and experimental validation". In: *Additive Manufacturing* 30 (2019), p. 100835.

[10] Bi, J., Wu, L., Li, S., Yang, Z., Jia, X., Starostenkov, M. D., and Dong, G. "Beam shaping technology and its application in metal laser additive manufacturing: A review". In: *Journal of Materials Research and Technology* (2023).

[11] Bierwisch, C. "DEM powder spreadingand SPH powder melting models for additive manufacturing processsimulations". In: (2019).

[12] Bierwisch, C. "Consistent thermo-capillarity and thermal boundary conditions for single-phase smoothed particle hydrodynamics". In: *Materials* 14.16 (2021), p. 4530.

[13] Bierwisch, C., Butz, A., Dietemann, B., Wessel, A., Najuch, T., and Mohseni-Mofidi, S. "PBF-LB/M multiphysics process simulation from powder to mechanical properties". In: *Procedia CIRP* 111 (2022), pp. 37–40.

[14] Boutaous, M., Liu, X., Siginer, D. A., and Xin, S. "Balling phenomenon in metallic laser based 3D printing process". In: *International Journal of Thermal Sciences* 167 (2021), pp. 107011–107021.

[15] Brackbill, J. U., Kothe, D. B., and Zemach, C. "A continuum method for modeling surface tension". In: *Journal of computational physics* 100.2 (1992), pp. 335–354.

[16] Bradstreet, B. “Effect of surface tension and metal flow on weld bead formation”. In: *Welding journal* 47.7 (1968), pp. 314–322.

[17] Breinlinger, T., Polfer, P., Hashibon, A., and Kraft, T. “Surface tension and wetting effects with smoothed particle hydrodynamics”. In: *Journal of Computational Physics* 243 (2013), pp. 14–27.

[18] Cleary, P. W. “Modelling confined multi-material heat and mass flows using SPH”. In: *Applied Mathematical Modelling* 22.12 (1998), pp. 981–993.

[19] Cleary, P. W. and Monaghan, J. J. “Conduction modelling using smoothed particle hydrodynamics”. In: *Journal of Computational Physics* 148.1 (1999), pp. 227–264.

[20] Colagrossi, A. and Landrini, M. “Numerical simulation of interfacial flows by smoothed particle hydrodynamics”. In: *Journal of computational physics* 191.2 (2003), pp. 448–475.

[21] Cole, R. H. and Weller, R. “Underwater explosions”. In: *Physics Today* 1.6 (1948), p. 35.

[22] Cummins, S., Cleary, P. W., Delaney, G., Phua, A., Sinnott, M., Gunasegaram, D., and Davies, C. “A coupled DEM/SPH computational model to simulate microstructure evolution in Ti-6Al-4V laser powder bed fusion processes”. In: *Metals* 11.6 (2021), p. 858.

[23] Cummins, S. J. and Rudman, M. “An SPH projection method”. In: *Journal of computational physics* 152.2 (1999), pp. 584–607.

[24] Dai, D. and Gu, D. “Influence of thermodynamics within molten pool on migration and distribution state of reinforcement during selective laser melting of AlN/AlSi10Mg composites”. In: *International Journal of Machine Tools and Manufacture* 100 (2016), pp. 14–24.

[25] Dao, M. H. and Lou, J. “Simulations of laser assisted additive manufacturing by smoothed particle hydrodynamics”. In: *Computer Methods in Applied Mechanics and Engineering* 373 (2021), p. 113491.

[26] Dong, X., Li, Z., and Zhang, X. “Contact-angle implementation in multiphase smoothed particle hydrodynamics simulations”. In: *Journal of Adhesion Science and Technology* 32.19 (2018), pp. 2128–2149.

[27] Farrokhpanah, A., Bussmann, M., and Mostaghimi, J. “New smoothed particle hydrodynamics (SPH) formulation for modeling heat conduction with solidification and melting”. In: *Numerical Heat Transfer, Part B: Fundamentals* 71.4 (2017), pp. 299–312.

[28] Farrokhpanah, A., Samareh, B., and Mostaghimi, J. “Applying contact angle to a two-dimensional multiphase smoothed particle hydrodynamics model”. In: *Journal of Fluids Engineering* 137.4 (2015), p. 041303.

[29] Fürstenau, J.-P., Wessels, H., Weißenfels, C., and Wriggers, P. “Generating virtual process maps of SLM using powder-scale SPH simulations”. In: *Computational Particle Mechanics* 7.4 (2020), pp. 655–677.

[30] Gao, F. and Sonin, A. A. “Precise deposition of molten microdrops: the physics of digital microfabrication”. In: *Proceedings of the Royal Society of London. Series A: Mathematical and Physical Sciences* 444.1922 (1994), pp. 533–554.

[31] Ge, W., Han, S., Fang, Y., Cheon, J., and Na, S. J. “Mechanism of surface morphology in electron beam melting of Ti6Al4V based on computational flow patterns”. In: *Applied Surface Science* 419 (2017), pp. 150–158.

[32] Ge, W., Han, S., Na, S. J., and Fuh, J. Y. H. “Numerical modelling of surface morphology in selective laser melting”. In: *Computational Materials Science* 186 (2021), pp. 110062–110070.

[33] Gingold, R. and Monaghan, J. “Kernel estimates as a basis for general particle methods in hydrodynamics”. In: *Journal of Computational Physics* 46.3 (1982), pp. 429–453.

[34] Gingold, R. A. and Monaghan, J. J. “Smoothed particle hydrodynamics: theory and application to non-spherical stars”. In: *Monthly notices of the royal astronomical society* 181.3 (1977), pp. 375–389.

[35] Gratzke, U, Kapadia, P., Dowden, J, Kroos, J, and Simon, G. “Theoretical approach to the humping phenomenon in welding processes”. In: *Journal of Physics D: Applied Physics* 25.11 (1992), p. 1640.

[36] Grenier, N., Antuono, M., Colagrossi, A., Le Touzé, D., and Alessandrini, B. “An Hamiltonian interface SPH formulation for multi-fluid and free surface flows”. In: *Journal of Computational Physics* 228.22 (2009), pp. 8380–8393.

[37] Grigoriev, S. N., Gusarov, A. V., Metel, A. S., Tarasova, T. V., Volosova, M. A., Okunkova, A. A., and Gusev, A. S. “Beam shaping in laser powder bed fusion: Péclet number and dynamic simulation”. In: *Metals* 12.5 (2022), p. 722.

[38] Grünewald, J., Blickle, V., Allenberg-Rabe, M., Wagenblast, P., and Wudy, K. “Flexible and highly dynamic beam shaping for Laser-Based Powder Bed Fusion of metals”. In: *Procedia CIRP* 111 (2022), pp. 65–70.

[39] Grünewald, J., Gehringer, F., Schmöller, M., and Wudy, K. “Influence of ring-shaped beam profiles on process stability and productivity in laser-based powder bed fusion of AISI 316L”. In: *Metals* 11.12 (2021), p. 1989.

[40] Grünewald, J., Reimann, J., and Wudy, K. “Influence of ring-shaped beam profiles on spatter characteristics in laser-based powder bed fusion of metals”. In: *Journal of Laser Applications* 35.4 (2023).

[41] Gu, D. and Shen, Y. “Balling phenomena in direct laser sintering of stainless steel powder: Metallurgical mechanisms and control methods”. In: *Materials & Design* 30.8 (2009), pp. 2903–2910.

[42] Gu, D., Xia, M., and Dai, D. “On the role of powder flow behavior in fluid thermodynamics and laser processability of Ni-based composites by selective laser melting”. In: *International Journal of Machine Tools and Manufacture* 137 (2019), pp. 67–78.

[43] Gu, D. and Yuan, P. “Thermal evolution behavior and fluid dynamics during laser additive manufacturing of Al-based nanocomposites: Underlying role of reinforcement weight fraction”. In: *Journal of Applied Physics* 118.23 (2015), pp. 233109–233119.

[44] Gu, H., Wei, C., Li, L., Han, Q., Setchi, R., Ryan, M., and Li, Q. “Multi-physics modelling of molten pool development and track formation in multi-track, multi-layer and multi-material selective laser melting”. In: *International Journal of Heat and Mass Transfer* 151 (2020), pp. 119458–119474.

[45] Guo, C., Xu, Z., Zhou, Y., Shi, S., Li, G., Lu, H., Zhu, Q., and Ward, R. M. “Single-track investigation of IN738LC superalloy fabricated by laser powder bed fusion: Track morphology, bead characteristics and part quality”. In: *Journal of Materials Processing Technology* 290 (2021), p. 117000.

[46] Gusarov, A. and Kruth, J.-P. “Modelling of radiation transfer in metallic powders at laser treatment”. In: *International journal of heat and mass transfer* 48.16 (2005), pp. 3423–3434.

[47] Gusarov, A., Yadroitsev, I, Bertrand, P., and Smurov, I. “Heat transfer modelling and stability analysis of selective laser melting”. In: *Applied Surface Science* 254.4 (2007), pp. 975–979.

[48] Gusarov, x. V. and Smurov, I. “Modeling the interaction of laser radiation with powder bed at selective laser melting”. In: *Physics Procedia* 5 (2010), pp. 381–394.

[49] Hu, H. and Eberhard, P. “Thermomechanically coupled conduction mode laser welding simulations using smoothed particle hydrodynamics”. In: *Computational Particle Mechanics* 4 (2017), pp. 473–486.

[50] Hu, H., Fetzer, F., Berger, P., and Eberhard, P. "Simulation of laser welding using advanced particle methods". In: *GAMM-Mitteilungen* 39.2 (2016), pp. 149–169.

[51] Hu, X. Y. and Adams, N. A. "A multi-phase SPH method for macroscopic and mesoscopic flows". In: *Journal of Computational Physics* 213.2 (2006), pp. 844–861.

[52] Hu, X. and Adams, N. "Angular-momentum conservative smoothed particle dynamics for incompressible viscous flows". In: *Physics of Fluids* 18.10 (2006).

[53] Hu, X. and Adams, N. A. "An incompressible multi-phase SPH method". In: *Journal of computational physics* 227.1 (2007), pp. 264–278.

[54] Huber, M., Keller, F., Säckel, W., Hirschler, M., Kunz, P., Hassanizadeh, S. M., and Nieken, U. "On the physically based modeling of surface tension and moving contact lines with dynamic contact angles on the continuum scale". In: *Journal of Computational Physics* 310 (2016), pp. 459–477.

[55] Johnson, L., Mahmoudi, M., Zhang, B., Seede, R., Huang, X., Maier, J. T., Maier, H. J., Karaman, I., Elwany, A., and Arróyave, R. "Assessing printability maps in additive manufacturing of metal alloys". In: *Acta Materialia* 176 (2019), pp. 199–210.

[56] Khairallah, S. A., Anderson, A. T., Rubenchik, A., and King, W. E. "Laser powder-bed fusion additive manufacturing: Physics of complex melt flow and formation mechanisms of pores, spatter, and denudation zones". In: *Acta Materialia* 108 (2016), pp. 36–45.

[57] Khairallah, S. A. and Anderson, A. "Mesoscopic simulation model of selective laser melting of stainless steel powder". In: *Journal of Materials Processing Technology* 214.11 (2014), pp. 2627–2636.

[58] Khairallah, S. A., Martin, A. A., Lee, J. R., Guss, G., Calta, N. P., Hammons, J. A., Nielsen, M. H., Chaput, K., Schwalbach, E., Shah, M. N., et al. "Controlling interdependent meso-nanosecond dynamics and defect generation in metal 3D printing". In: *Science* 368.6491 (2020), pp. 660–665.

[59] Khan, M. and Dickens, P. "Selective Laser Melting (SLM) of pure gold". In: *Gold bulletin* 43.2 (2010), pp. 114–121.

[60] Khorasani, A., Gibson, I., Veetil, J. K., and Ghasemi, A. H. "A review of technological improvements in laser-based powder bed fusion of metal printers". In: *The International Journal of Advanced Manufacturing Technology* 108 (2020), pp. 191–209.

[61] Körner, C., Attar, E., and Heinl, P. "Mesoscopic simulation of selective beam melting processes". In: *Journal of Materials Processing Technology* 211.6 (2011), pp. 978–987.

[62] Krimi, A., Rezoug, M., Khelladi, S., Nogueira, X., Deligant, M., and Ramírez, L. "Smoothed particle hydrodynamics: a consistent model for interfacial multiphase fluid flow simulations". In: *Journal of Computational Physics* 358 (2018), pp. 53–87.

[63] Kruth, J.-P., Froyen, L., Van Vaerenbergh, J., Mercelis, P., Rombouts, M., and Lauwers, B. "Selective laser melting of iron-based powder". In: *Journal of materials processing technology* 149.1-3 (2004), pp. 616–622.

[64] Lafaurie, B., Nardone, C., Scardovelli, R., Zaleski, S., and Zanetti, G. "Modelling merging and fragmentation in multiphase flows with SURFER". In: *Journal of Computational Physics* 113.1 (1994), pp. 134–147.

[65] Lee, Y. and Zhang, W. "Mesoscopic simulation of heat transfer and fluid flow in laser powder bed additive manufacturing". In: (2015).

[66] Lee, Y. and Zhang, W. "Modeling of heat transfer, fluid flow and solidification microstructure of nickel-base superalloy fabricated by laser powder bed fusion". In: *Additive Manufacturing* 12 (2016), pp. 178–188.

[67] Li, L., Li, J.-Q., and Fan, T.-H. "Phase-field modeling of wetting and balling dynamics in powder bed fusion process". In: *Physics of Fluids* 33.4 (2021), pp. 042116–042126.

[68] Li, R., Liu, J., Shi, Y., Wang, L., and Jiang, W. "Balling behavior of stainless steel and nickel powder during selective laser melting process". In: *The International Journal of Advanced Manufacturing Technology* 59.9 (2012), pp. 1025–1035.

[69] Li, W., Meng, L., Zhang, Q., Liu, Y., Wang, S., Ma, J., Zhou, Y., Zhou, D., Wang, H., Cheng, W., et al. "Melt pool evolution and microstructure simulation of SLM 316L based on SPH-PFM coupling model". In: *Journal of Materials Research and Technology* 28 (2024), pp. 3037–3051.

[70] Li, W., Shen, M., Meng, L., Luo, P., Liu, Y., Ma, J., Niu, X., Wang, H., Cheng, W., and Wei, T. "Establishment of a three-dimensional mathematical model of SLM process based on SPH method". In: *Computational Particle Mechanics* (2023), pp. 1–17.

[71] Li, Y. and Gu, D. "Parametric analysis of thermal behavior during selective laser melting additive manufacturing of aluminum alloy powder". In: *Materials & design* 63 (2014), pp. 856–867.

[72] Li, Z., Li, B.-Q., Bai, P., Liu, B., and Wang, Y. "Research on the thermal behaviour of a selectively laser melted aluminium alloy: simulation and experiment". In: *Materials* 11.7 (2018), pp. 1172–1186.

[73] Lin, Y., Lüthi, C., Afrasiabi, M., and Bambach, M. "Enhanced heat source modeling in particle-based laser manufacturing simulations with ray tracing". In: *International Journal of Heat and Mass Transfer* 214 (2023), p. 124378.

[74] Liu, J., Gu, D.-d., Chen, H.-y., Dai, D.-h., and Zhang, H. "Influence of substrate surface morphology on wetting behavior of tracks during selective laser melting of aluminum-based alloys". In: *Journal of Zhejiang University-SCIENCE A* 19.2 (2018), pp. 111–121.

[75] Liu, M. and Liu, G. "Smoothed particle hydrodynamics (SPH): an overview and recent developments". In: *Archives of computational methods in engineering* 17 (2010), pp. 25–76.

[76] Liu, S., Liu, J., Chen, J., and Liu, X. "Influence of surface tension on the molten pool morphology in laser melting". In: *International Journal of Thermal Sciences* 146 (2019), p. 106075.

[77] Liu, S. and Guo, H. "Balling behavior of selective laser melting SLM magnesium alloy". In: *Materials* 13.16 (2020), pp. 3632–3653.

[78] Long, T. and Huang, H. "An improved high order smoothed particle hydrodynamics method for numerical simulations of selective laser melting process". In: *Engineering Analysis with Boundary Elements* 147 (2023), pp. 320–335.

[79] Lucy, L. B. "A numerical approach to the testing of the fission hypothesis". In: *Astronomical Journal, vol. 82, Dec. 1977, p. 1013-1024.* 82 (1977), pp. 1013–1024.

[80] Lüthi, C., Afrasiabi, M., and Bambach, M. "An adaptive smoothed particle hydrodynamics (SPH) scheme for efficient melt pool simulations in additive manufacturing". In: *Computers & Mathematics with Applications* 139 (2023), pp. 7–27.

[81] Ma, J., Niu, X., Zhou, Y., Li, W., Liu, Y., Shen, M., Wang, H., Cheng, W., and You, Z. "Simulation of solidification microstructure evolution of 316L stainless steel fabricated by selective laser melting using a coupled model of smooth particle hydrodynamics and cellular automata". In: *Journal of Materials Research and Technology* 27 (2023), pp. 600–616.

[82] Martin, A. A., Calta, N. P., Khairallah, S. A., Wang, J., Depond, P. J., Fong, A. Y., Thampy, V., Guss, G. M., Kiss, A. M., Stone, K. H., et al. "Dynamics of pore formation during laser powder bed fusion additive manufacturing". In: *Nature communications* 10.1 (2019), p. 1987.

[83] Matthews, M. J., Guss, G., Khairallah, S. A., Rubenchik, A. M., Depond, P. J., and King, W. E. "Denudation of metal powder layers in laser powder-bed fusion processes". In: *Additive manufacturing handbook*. CRC Press, 2017, pp. 677–692.

[84] Matthews, M., Roehling, T., Khairallah, S., Tumkur, T., Guss, G, Shi, R, Roehling, J., Smith, W., Vrancken, B., Ganeriwala, R., et al. “Controlling melt pool shape, microstructure and residual stress in additively manufactured metals using modified laser beam profiles”. In: *Procedia Cirp* 94 (2020), pp. 200–204.

[85] Meier, C., Fuchs, S. L., Hart, A. J., and Wall, W. A. “A novel smoothed particle hydrodynamics formulation for thermo-capillary phase change problems with focus on metal additive manufacturing melt pool modeling”. In: *Computer Methods in Applied Mechanics and Engineering* 381 (2021), p. 113812.

[86] Meier, C., Weissbach, R., Weinberg, J., Wall, W. A., and Hart, A. J. “Critical influences of particle size and adhesion on the powder layer uniformity in metal additive manufacturing”. In: *Journal of Materials Processing Technology* 266 (2019), pp. 484–501.

[87] Mi, Y., Mahade, S., Sikström, F., Choquet, I., Joshi, S., and Ancona, A. “Conduction mode laser welding with beam shaping using a deformable mirror”. In: *Optics & Laser Technology* 148 (2022), p. 107718.

[88] Monaghan, J. J. “Smoothed particle hydrodynamics”. In: *Annual review of astronomy and astrophysics* 30.1 (1992), pp. 543–574.

[89] Monaghan, J. J. “Smoothed particle hydrodynamics”. In: *Reports on progress in physics* 68.8 (2005), p. 1703.

[90] Monaghan, J. J. “SPH compressible turbulence”. In: *Monthly Notices of the Royal Astronomical Society* 335.3 (2002), pp. 843–852.

[91] Monaghan, J. J. and Rafiee, A. “A simple SPH algorithm for multi-fluid flow with high density ratios”. In: *International Journal for Numerical Methods in Fluids* 71.5 (2013), pp. 537–561.

[92] Moniz, L., Chen, Q., Guillemot, G., Bellet, M., Gandin, C.-A., Colin, C., Bartout, J.-D., and Berger, M.-H. “Additive manufacturing of an oxide ceramic by laser beam melting—Comparison between finite element simulation and experimental results”. In: *Journal of Materials Processing Technology* 270 (2019), pp. 106–117.

[93] Morris, J. P. “Simulating surface tension with smoothed particle hydrodynamics”. In: *International journal for numerical methods in fluids* 33.3 (2000), pp. 333–353.

[94] Morris, J. P., Fox, P. J., and Zhu, Y. “Modeling low Reynolds number incompressible flows using SPH”. In: *Journal of computational physics* 136.1 (1997), pp. 214–226.

[95] Morris, J. P. “A study of the stability properties of smooth particle hydrodynamics”. In: *Publications of the Astronomical Society of Australia* 13.1 (1996), pp. 97–102.

[96] Mostafaei, A., Zhao, C., He, Y., Ghiaasiaan, S. R., Shi, B., Shao, S., Shamsaei, N., Wu, Z., Kouraytem, N., Sun, T., et al. “Defects and anomalies in powder bed fusion metal additive manufacturing”. In: *Current Opinion in Solid State and Materials Science* 26.2 (2022), pp. 100974–101098.

[97] Mukherjee, T, Wei, H., De, A, and DebRoy, T. “Heat and fluid flow in additive manufacturing–Part II: Powder bed fusion of stainless steel, and titanium, nickel and aluminum base alloys”. In: *Computational Materials Science* 150 (2018), pp. 369–380.

[98] Nahr, F., Bartels, D., Rothfelder, R., and Schmidt, M. “Influence of Novel Beam Shapes on Laser-Based Processing of High-Strength Aluminium Alloys on the Basis of EN AW-5083 Single Weld Tracks”. In: *Journal of Manufacturing and Materials Processing* 7.3 (2023), p. 93.

[99] Niu, H. and Chang, I. “Instability of scan tracks of selective laser sintering of high speed steel powder”. In: *Scripta materialia* 41.11 (1999), pp. 1229–1234.

[100] Nugent, S and Posch, H. “Liquid drops and surface tension with smoothed particle applied mechanics”. In: *Physical Review E* 62.4 (2000), p. 4968.

[101] Okunkova, A., Volosova, M., Peretyagin, P., Vladimirov, Y., Zhirnov, I., and Gusarov, A. "Experimental approbation of selective laser melting of powders by the use of non-Gaussian power density distributions". In: *Physics Procedia* 56 (2014), pp. 48–57.

[102] Olejnik, M. and Pozorski, J. "A robust method for wetting phenomena within smoothed particle hydrodynamics". In: *Flow, Turbulence and Combustion* 104 (2020), pp. 115–137.

[103] Papazoglou, E., Karkalos, N., and Markopoulos, A. "A comprehensive study on thermal modeling of SLM process under conduction mode using FEM". In: *The International Journal of Advanced Manufacturing Technology* 111.9 (2020), pp. 2939–2955.

[104] Parida, R. P. and Senthilkumar, V. "Experimental studies of defect generation in selective laser melted Inconel 718 alloy". In: *Proceedings - Materials Today*. Vol. 39. Elsevier, 2021, pp. 1372–1377.

[105] Plateau, J. A. F. *Statique expérimentale et théorique des liquides soumis aux seules forces moléculaires*. Vol. 2. Gauthier-Villars, 1873.

[106] Price, D. J. "Smoothed particle hydrodynamics and magnetohydrodynamics". In: *Journal of Computational Physics* 231.3 (2012), pp. 759–794.

[107] Rayleigh, L. "On the instability of jets". In: *Proceedings of the London mathematical society*. Vol. 1. 1. Wiley Online Library, 1878, pp. 4–13.

[108] Ren, Z., Zhang, D. Z., Fu, G., Jiang, J., and Zhao, M. "High-fidelity modelling of selective laser melting copper alloy: Laser reflection behavior and thermal-fluid dynamics". In: *Materials & Design* 207 (2021), pp. 109857–109872.

[109] Roberts, I. A., Wang, C., Esterlein, R, Stanford, M, and Mynors, D. "A three-dimensional finite element analysis of the temperature field during laser melting of metal powders in additive layer manufacturing". In: *International Journal of Machine Tools and Manufacture* 49.12-13 (2009), pp. 916–923.

[110] Roehling, T. T., Shi, R., Khairallah, S. A., Roehling, J. D., Guss, G. M., McKeown, J. T., and Matthews, M. J. "Controlling grain nucleation and morphology by laser beam shaping in metal additive manufacturing". In: *Materials & Design* 195 (2020), p. 109071.

[111] Roehling, T. T., Wu, S. S., Khairallah, S. A., Roehling, J. D., Soezeri, S. S., Crumb, M. F., and Matthews, M. J. "Modulating laser intensity profile ellipticity for microstructural control during metal additive manufacturing". In: *Acta Materialia* 128 (2017), pp. 197–206.

[112] Rothfelder, R., Huber, F., and Schmidt, M. "Influence of beam shape on spatter formation during PBF-LB/M of Ti6Al4V and tungsten powder". In: *Procedia CIRP* 111 (2022). 12th CIRP Conference on Photonic Technologies [LANE 2022], pp. 14–17. ISSN: 2212-8271. DOI: https://doi.org/10.1016/j.procir.2022.08.105.

[113] Russell, M., Souto-Iglesias, A, and Zohdi, T. "Numerical simulation of Laser Fusion Additive Manufacturing processes using the SPH method". In: *Computer Methods in Applied Mechanics and Engineering* 341 (2018), pp. 163–187.

[114] Schiaffino, S. and Sonin, A. A. "Motion and arrest of a molten contact line on a cold surface: an experimental study". In: *Physics of fluids* 9.8 (1997), pp. 2217–2226.

[115] Schlick, C. "An inexpensive BRDF model for physically-based rendering". In: *Computer graphics forum*. Vol. 13. Wiley Online Library. 1994, pp. 233–246.

[116] Scime, L. and Beuth, J. "Melt pool geometry and morphology variability for the Inconel 718 alloy in a laser powder bed fusion additive manufacturing process". In: *Additive Manufacturing* 29 (2019), p. 100830.

[117] Shah, D. and Volkov, A. N. “Combined smoothed particle hydrodynamics-ray tracing method for simulations of keyhole formation in laser melting of bulk and powder metal targets”. In: *ASME International Mechanical Engineering Congress and Exposition*. Vol. 59377. American Society of Mechanical Engineers. 2019, V02AT02A057.

[118] Shi, R., Khairallah, S. A., Roehling, T. T., Heo, T. W., McKeown, J. T., and Matthews, M. J. “Microstructural control in metal laser powder bed fusion additive manufacturing using laser beam shaping strategy”. In: *Acta Materialia* 184 (2020), pp. 284–305.

[119] Sow, M., De Terris, T., Castelnau, O., Hamouche, Z, Coste, F., Fabbro, R., and Peyre, P. “Influence of beam diameter on Laser Powder Bed Fusion (L-PBF) process”. In: *Additive Manufacturing* 36 (2020), p. 101532.

[120] Stopyra, W., Gruber, K., Smolina, I., Kurzynowski, T., and Kuźnicka, B. “Laser powder bed fusion of AA7075 alloy: Influence of process parameters on porosity and hot cracking”. In: *Additive Manufacturing* 35 (2020), p. 101270.

[121] Swope, W. C., Andersen, H. C., Berens, P. H., and Wilson, K. R. “A computer simulation method for the calculation of equilibrium constants for the formation of physical clusters of molecules: Application to small water clusters”. In: *The Journal of chemical physics* 76.1 (1982), pp. 637–649.

[122] Szewc, K., Pozorski, J., and Taniere, A. “Modeling of natural convection with smoothed particle hydrodynamics: non-Boussinesq formulation”. In: *International Journal of Heat and Mass Transfer* 54.23-24 (2011), pp. 4807–4816.

[123] Tartakovsky, A. and Meakin, P. “Modeling of surface tension and contact angles with smoothed particle hydrodynamics”. In: *Physical Review E—Statistical, Nonlinear, and Soft Matter Physics* 72.2 (2005), p. 026301.

[124] Tumkur, T. U., Guss, G., Roehling, J. D., Khairallah, S. A., and Matthews, M. J. “Metal Additive Manufacturing using complex beam shaping”. In: *Procedia CIRP* 111 (2022), pp. 71–74.

[125] Tumkur, T. U., Voisin, T., Shi, R., Depond, P. J., Roehling, T. T., Wu, S., Crumb, M. F., Roehling, J. D., Guss, G., Khairallah, S. A., et al. “Nondiffractive beam shaping for enhanced optothermal control in metal additive manufacturing”. In: *Science Advances* 7.38 (2021), eabg9358.

[126] Wang, Z.-B., Chen, R., Wang, H., Liao, Q., Zhu, X., and Li, S.-Z. “An overview of smoothed particle hydrodynamics for simulating multiphase flow”. In: *Applied Mathematical Modelling* 40.23-24 (2016), pp. 9625–9655.

[127] Weirather, J., Rozov, V., Wille, M., Schuler, P., Seidel, C., Adams, N. A., and Zaeh, M. F. “A smoothed particle hydrodynamics model for laser beam melting of Ni-based alloy 718”. In: *Computers & Mathematics with Applications* 78.7 (2019), pp. 2377–2394.

[128] Wessels, H, Bode, T, Weißenfels, C., Wriggers, P, and Zohdi, T. “Investigation of heat source modeling for selective laser melting”. In: *Computational Mechanics* 63 (2019), pp. 949–970.

[129] Wimmer, A., Panzer, H., Zoeller, C., Adami, S., Adams, N. A., and Zaeh, M. F. “Experimental and numerical investigations of the hot cracking susceptibility during the powder bed fusion of AA 7075 using a laser beam”. In: *Progress in Additive Manufacturing* (2023), pp. 1–15.

[130] Wimmer, A., Yalvac, B., Zoeller, C., Hofstaetter, F., Adami, S., Adams, N. A., and Zaeh, M. F. “Experimental and numerical investigations of in situ alloying during powder bed fusion of metals using a laser beam”. In: *Metals* 11.11 (2021), p. 1842.

[131] Wischeropp, T. M., Salazar, R., Herzog, D., and Emmelmann, C. “Simulation of the effect of different laser beam intensity profiles on heat distribution in selective laser melting”. In: *Lasers in Manufacturing Conference, June 22–25*. WLT Munich, Germany. 2015.

[132] Wischeropp, T. M., Tarhini, H., and Emmelmann, C. “Influence of laser beam profile on the selective laser melting process of AlSi10Mg”. In: *Journal of Laser Applications* 32.2 (2020).

[133] Wu, J., Ma, J., Niu, X., Shen, M., Wei, T., and Li, W. “Numerical Simulation of Selective Laser Melting of 304 L Stainless Steel”. In: *Metals* 13.7 (2023), p. 1212.

[134] Yadroitsev, I, Gusarov, A, Yadroitsava, I, and Smurov, I. “Single track formation in selective laser melting of metal powders”. In: *Journal of Materials Processing Technology* 210.12 (2010), pp. 1624–1631.

[135] Yadroitsev, I., Krakhmalev, P., Yadroitsava, I., Johansson, S., and Smurov, I. “Energy input effect on morphology and microstructure of selective laser melting single track from metallic powder”. In: *Journal of Materials Processing Technology* 213.4 (2013), pp. 606–613.

[136] Yan, W., Ge, W., Qian, Y., Lin, S., Zhou, B., Liu, W. K., Lin, F., and Wagner, G. J. “Multi-physics modeling of single/multiple-track defect mechanisms in electron beam selective melting”. In: *Acta Materialia* 134 (2017), pp. 324–333.

[137] Yang, H., Li, Z., and Wang, S. “The analytical prediction of thermal distribution and defect generation of Inconel 718 by selective laser melting”. In: *Applied Sciences* 10.20 (2020), pp. 7300–7319.

[138] Yang, L., Rakhsha, M., and Negrut, D. “Comparison of surface tension models in smoothed particles hydrodynamics method”. In: *International Design Engineering Technical Conferences and Computers and Information in Engineering Conference*. Vol. 59261. American Society of Mechanical Engineers. 2019, V006T09A028.

[139] Yang, P., Zhang, F., Huang, C., and Liu, M. “Numerical simulation of selective laser melting based on SPH method”. In: *Scientia Sinica Physica, Mechanica & Astronomica* 52.10 (2022), p. 104706.

[140] Ye, T., Pan, D., Huang, C., and Liu, M. “Smoothed particle hydrodynamics (SPH) for complex fluid flows: Recent developments in methodology and applications”. In: *Physics of Fluids* 31.1 (2019).

[141] Yeganehdoust, F, Yaghoubi, M, Emdad, H, and Ordoubadi, M. “Numerical study of multiphase droplet dynamics and contact angles by smoothed particle hydrodynamics”. In: *Applied Mathematical Modelling* 40.19-20 (2016), pp. 8493–8512.

[142] Yu, G., Gu, D., Dai, D., Xia, M., Ma, C., and Shi, Q. “On the role of processing parameters in thermal behavior, surface morphology and accuracy during laser 3D printing of aluminum alloy”. In: *Journal of Physics D: Applied Physics* 49.13 (2016), pp. 135501–135516.

[143] Yuan, P. and Gu, D. “Molten pool behaviour and its physical mechanism during selective laser melting of TiC/AlSi10Mg nanocomposites: simulation and experiments”. In: *Journal of Physics D: Applied Physics* 48.3 (2015), p. 035303.

[144] Yuan, W., Chen, H., Li, S., Heng, Y., Yin, S., and Wei, Q. “Understanding of adopting flat-top laser in laser powder bed fusion processed Inconel 718 alloy: simulation of single-track scanning and experiment”. In: *Journal of Materials Research and Technology* 16 (2022), pp. 1388–1401.

[145] Zhou, X., Liu, X., Zhang, D., Shen, Z., and Liu, W. “Balling phenomena in selective laser melted tungsten”. In: *Journal of Materials Processing Technology* 222 (2015), pp. 33–42.

[146] Zöller, C, Adams, N., and Adami, S. “Numerical investigation of balling defects in laser-based powder bed fusion of metals with Inconel 718”. In: *Additive Manufacturing* 73 (2023), p. 103658.

[147] Zöller, C, Adams, N., and Adami, S. “Beam-shaping in laser-based powder bed fusion of metals: A computational analysis of point-ring intensity profiles”. In: *Additive Manufacturing* 93 (2024), p. 104402.

[148] Zöller, C., Adams, N. A., and Adami, S. “A partitioned continuous surface stress model for multiphase smoothed particle hydrodynamics”. In: *Journal of Computational Physics* 472 (2023), p. 111716.